Investigating the Root Causes of the Low Electroluminescence Stability of Upright Blue Quantum Dot Light-Emitting Devices

by

Atefeh Ghorbani Koltapeh

A thesis

presented to the University of Waterloo

in fulfillment of the

thesis requirement for the degree of

Doctor of Philosophy

in

Electrical and Computer Engineering (Nanotechnology)

Waterloo, Ontario, Canada, 2024

Examining Committee Membership

The following served on the Examining Committee for this thesis. The decision of the Examining Committee is by majority vote.

External Examiner	Benoit Hugo Lessard Associate Professor, Dept. of Chemical & Biological Engineering, University of Ottawa
Supervisor	Hany Aziz Professor, Dept. of Electrical & Computer Engineering, University of Waterloo
Internal Member	Dayan Ban Professor, Dept. of Electrical & Computer Engineering, University of Waterloo
Internal Member	Mahla Poudineh Assistant Professor, Dept. of Electrical & Computer Engineering, University of Waterloo
Internal-external Member	Yuning Li Professor, Dept. of Chemical Engineering, University of Waterloo

Author's Declaration

I hereby declare that I am the sole author of this thesis. This is a true copy of the thesis, including any required final revisions, as accepted by my examiners.

I understand that my thesis may be made electronically available to the public.

Abstract

Quantum dot light-emitting devices (QLEDs) are promising candidates for use in the next-generation flat panel displays. QLEDs operate based on the electroluminescence (EL) from quantum dots (QDs) as the emissive layer. QLEDs have gained attraction due to the QDs' intriguing properties such as high photoluminescence quantum yield (PLQY) of nearly 100%, narrow emission full-width at half maximum (FWHM < 30 nm) which provides a wide color gamut, the tunability of their peak luminescence wavelengths across the entire visible spectrum, and their solution-processability which makes them compatible to low-cost and flexible fabrication techniques. These features make QLEDs superior to their currently commercialized organic light-emitting devices (OLEDs) rivals, as they provide more natural images. However, QLEDs EL stability for the three red, green, and blue primary colors are not similar. Particularly, blue QLEDs (B-QLEDs) are the least stable which makes it the bottleneck for QLEDs commercialization.

Despite the massive efforts on the QLEDs' development and progress in achieving efficient devices, the B-QLEDs still suffer from poor EL stability. Developing effective strategies to improve the EL stability of B-QLEDs requires that the underlying degradation mechanisms must first be identified. Although high EL stability refers to maintaining the EL level when the device is under electrical bias, i.e. electrical stability, it is imperative that the high EL stability first requires that the materials do not change with time in the absence of bias, i.e. high shelf stability. Unfortunately, there is no clear consensus in the field on the fundamental factors limiting the B-QLEDs EL stability, and the roles of electrical bias versus just the temporal stability of the devices remain entangled.

The main focus of this thesis is to pinpoint the underlying reasons governing the B-QLEDs EL stability and explain the possible mechanisms for the B-QLEDs EL loss. This work utilizes the upright QLED structure, in which the light output is through the anode, which consists of an organic hole transport layer (HTL), CdSe-based QDs, and an inorganic ZnMgO electron transport layer (ETL). The focus of this work is B-QLEDs although red and green QDs are also used as a reference for comparison at some point.

To systematically study the EL stability of B-QLEDs as the objective of this work, the B-QDs PLQY stability is monitored in storage (shelf life) and under electrical stress with different scenarios. Firstly, the PLQY stability of blue QDs (B-QDs) as a thin film is studied over time. The B-QDs are placed in contact with each of the ETL or HTL as in the B-QLEDs structure to determine if interactions between

the different materials in the device stack influence the shelf life of the B-QDs PLQY. It is found that B-QDs PLQY is stable intrinsically or in contact with the HTL. However, the ETL is found to negatively affect the B-QDs PLQY over time, an effect that arises from the diffusion of species from the ETL into the QD layer as well as morphological changes in the ETL that both result in the QDs PLQY drop.

Next, the effect of bias is investigated, first focusing on its effect on the B-QDs PLQY. Single carrier devices are fabricated to be able to exclusively study the potential role of positive (holes) and negative (electrons) carriers upon electrical stress. The results show that HTL undergoes degradation upon hole current flow leading to the B-QDs PLQY decay, whereas the electron current flow has minimal effect on the B-QDs PLQY. The organic HTL is replaced with a more robust thermally crosslinked HTL. Although the new HTL sustained the QDs PLQY, it is not advantageous for improving the B-QLEDs EL stability whereas it can improve the green QLEDs EL stability with the same structure by a factor of two. The results indicate that neither HTL degradation nor B-QDs PLQY drop is the predominant reason for the B-QLEDs' fast EL loss.

The study is further continued by probing the electrical characteristics of the single-carrier devices. The results show that charge injection efficiency in B-QLEDs changes over time due to electrical aging. The results show that the changes worsen the initial charge balance condition during the device operation and thereby a significant EL quenching leads to the EL loss in B-QLEDs. However, the changes are observed to be partially reversible so that driving the B-QLEDs under pulsed current instead of constant current doubles the electrical stability of B-QLEDs.

Ultimately, the investigations continued, and it is found that B-QLEDs suffer from holes leaking into the ZnMgO layer and it causes a significant degradation to the ZnMgO layer. The findings indicate that the damage to ZnMgO layer induced by holes results in more defect density of states in the ETL and worsens the ETL electron injection capacity. This also serves as another contributing factor to the B-QLEDs poor EL stability.

Acknowledgements

This Ph.D. journey, with its numerous ups and downs, has indeed formed me both professionally and personally. A supportive group of people has helped me navigate this challenging journey, and I would like to thank them all.

First, I would like to express deep gratitude to my supervisor, Professor Hany Aziz, for his outstanding support, availability, and most importantly, his constructive and detailed feedback, which has significantly elevated my personal and professional growth. His guidance, compassion, invaluable knowledge, and profound insights have not only inspired me to become a better researcher but also a better individual.

Next, I would like to acknowledge my advisory committee, Professor Dayan Ban, Professor Mahla Poudineh, and Professor Yuning Li. I would also like to thank Professor Benoit Hugo Lessard for accepting the role of my external Ph.D. examiner.

I am sincerely thankful for being in a lab, Giga-to-Nano, with supportive and handy people like Mr. Richard Barber and Mr. Czang-Ho Lee, our lab managers, and my colleagues, past and present.

I cannot begin to express my thanks to my amazing mom and dad, Leili and Kazem, and my lovely siblings, for their unconditional support, kindness, and love. If not for your faith in me, I would not have made it this far. Mom and Dad, your wise and compassionate parenting has had a powerful impact on my life, and you are the inspiration behind my endeavors and successes.

Financial support from the Natural Sciences and Engineering Research Council of Canada (NSERC) and the WIN Nanofellowship is greatly appreciated.

Dedication

I dedicate this thesis to my beloved parents, Leili and Kazem, for their endless support and care.

Table of Contents

List of Figures

List of Tables

Chapter 1
Introduction and Research Objectives

1.1 Motivation

Display technology has become ubiquitous in human daily life, finding widespread applications ranging from smartphones to TVs, virtual reality devices, and beyond. The liquid crystal display (LCD) was invented in the late 1960s[1]. After three decades of dedicated material and device advancement, coupled with substantial investments in fabrication technology, organic light-emitting diode (OLED) displays have experienced exponential growth, emerging as formidable contenders to LCDs in the display market[2-3].

Since the discovery of quantum confinement effects in semiconductors at nanoscale dimensions, quantum dot (QD) materials have gained significant interest due to their wide applications in electronic devices, including lasers, displays, biosensors, and photovoltaics[4]. Colloidal QDs are solution-processed semiconducting nanocrystals that first emerged in the 1980s, comprising semiconductors of groups II-VI, IV-VI, and III-V[5-6]. Quantum dot light-emitting devices (QLEDs) operate based on the electroluminescence (EL) phenomenon where the light is produced by radiative recombination of electron-hole pairs subsequent to being injected into the QDs due to the external bias application. QLEDs have attractive properties that make them suitable for display applications. Some of these advantages are (1) flexible bandgap and emission peak wavelength by tuning the size and composition (2) narrow emission full-width at half-maximum (FWHM<30 nm) and high color purity providing a wide color gamut (3) high photoluminescence (PL) quantum yield (PLQY) approaching 100% (4) cost-effective and scalable solution-process fabrication (5) compatible with flexible substrates[4, 7-9]. Most high-performance QLEDs use CdSe-based II-VI QDs as the emitters due to their direct bandgap (1.73 eV) with the tunability of their peak luminescence wavelength across the entire visible range. Moreover,

they can be processed by solution-coating processes, as they can be dispersed in solvents making colloidal QDs.

In the early stages that QLEDs first emerged in 1994, the CdSe-based QDs emissive layer (EML) was simply sandwiched between two electrodes[10-11]. Thereafter, the device architecture evolved to incorporate elaborate multilayers resembling an optimized OLED structure, thereby enhancing both charge injection and efficiency. Currently, a typical QLED structure includes a QD layer sandwiched between a hole transport layer (HTL) and an electron transport layer (ETL), followed by the necessary charge (hole or electron) injection layers (HIL or EIL), an anode and a cathode, respectively.

Since the birth of QLEDs, Cd-based QLEDs have achieved great progress in efficiency which is encouraging for their commercialization in cost-effective, large-area, and flexible displays. To date, maximum External Quantum Efficiency (EQE) of 30.0%, 28.7%, and 21.9% are achieved for the three primary colors used in displays, red, green, and blue, respectively[12-13]. These record efficiencies pertain to all-solution-processed QLEDs, wherein all layers except for the electrodes are coated using a solution-coating process.

Despite the significant success of improving the QLEDs' efficiency through advancements in both material and device architecture, a notable electroluminescence (EL) stability gap persists, particularly evident in blue QLEDs (B-QLEDs) compared to their red and green counterparts. The EL stability of the QLEDs refers to their ability to maintain their EL efficiency under constant current driving. EL stability depends on both temporal stability and electrical stability. Therefore, one of the requirements for the QLEDs to have high EL stability is to have high temporal stability or equivalently long shelf life. This means QLEDs need to be capable of maintaining their efficiency when kept in storage over time. Also, electrical stability is another important factor affecting EL stability. Electrical stability or operational lifetime refers to the time that it takes for the device to lose its EL intensity to half of its initial value under continuous bias application.

Interactions between materials of the different layers in the device stack or with ambient species can lead to various changes that affect the QLED efficiency over time even without bias limiting their shelf life. Electrical stress can also initiate various degradation processes in QLEDs and ultimately result in device EL loss. Therefore, both long shelf life and high electrical stability are necessary for a QLED to have high EL stability.

Currently, the bottleneck for the commercialization of the QLED technology is the B-QLEDs' low EL stability which needs to be addressed. Moreover, the underlying reasons for the poor EL stability of B-QLEDs and their degradation mechanisms are not well understood. Thus, discovering the EL stability issues of the B-QLEDs, where there is a gap of knowledge, is useful to enhance the devices' EL stability.

1.2 Objectives

The objective of this work is to identify the reasons behind the poor EL stability in CdSe-based B-QLEDs. This requires decoupling the temporal stability effects, i.e. during storage (shelf life) from the bias-induced changes that happen during the device operation which govern the electrical stability. In order for a systematic approach to discover the possible issues, we narrow down the target by taking the following steps:

1. Investigating the temporal stability of the B-QDs' PLQY (without bias). In this work, B-QLEDs with conventional (upright) structures are studied in which the device stack consists of Glass/ITO/HIL/HTL/B-QD/ETL/Al. To start with studying the shelf life of the B-QLEDs, it is critical to verify whether the B-QDs can maintain their PLQY over time in the device stack. Thus, as the first step, the B-QDs PLQY is monitored over time in the following scenarios to understand whether B-QDs PLQY intrinsically is stable or if interactions with the neighboring layers in the stack affect PLQY. In addition, in case of observing any degradation, further investigations are pursued to find the possible mechanisms or explanations for the results. Therefore, the B-QDs PLQY is studied in these scenarios:

    - B-QDs alone, when the B-QDs as a single solid thin film is coated on glass.
    - B-QDs adjacent to the HTL, when the B-QDs are coated on top of the hole supply part of the device (Glass/anode/HIL/HTL/B-QD)
    - B-QDs adjacent to the ETL, when the B-QDs are only subjected to the subsequent layers of ETL/cathode (Glass/B-QDs/ETL/cathode).

2. Exploring the effect of electrical stress on the B-QDs' PLQY as a possible factor behind the poor electrical stability. After investigating the shelf life of the B-QLEDs, the B-QDs PLQY is tested under specific conditions where either electrons or holes are dominant in current flow. Since the device operation involves the injection and transport of both electrons and holes,

single carrier hole-only devices (HODs) and electron-only devices (EODs) are designed and fabricated to exclusively study the potential effect of electrons or holes on B-QDs PLQY. The investigations can further continue to find solutions to address the identified possible issues. Thus, this part mainly encompasses:

- Studying the effect of holes on the B-QDs PLQY in HODs.
- Studying the effect of electrons on the B-QDs PLQY in EODs.

3. Exploring other possible factors that may be contributing to the electrical stability like charge balance, carrier supply efficiency, and carrier-induced degradation on the B-QLEDs' EL stability:

- Studying the electrical characteristics of EODs and HODs under bias to probe the electrons or holes supply individually. In addition to the optical PLQY stability of the B-QDs in single carrier devices, as studied in the previous section, the electrical characteristics of the devices also have to be stable. By studying the electrical properties of the single carrier devices, the charge supply, e.g. carrier injection and transport properties together with the electrical properties of the CTLs are monitored.
- Investigating the charge leakage phenomenon in B-QLEDs and its subsequent effects on the device stability. Achieving high electrical stability necessitates an initially balanced ratio of electron-to-hole injection, which must be sustained throughout the operation. In reality, non-idealities such as unbalanced charge injection may cause excess charges to accumulate within the device or leak to the countercharge transport layer. This can result in EL loss due to degradation in CTLs or the B-QD layer.

1.3 Thesis Organization

The focus of this thesis is to identify degradation mechanisms affecting the B-QLEDs' EL stability. The thesis chapters are organized as follows:

- **Chapter 2**: Providing fundamental knowledge on device physics and operational principles, introducing the parameters, and variables for evaluating the device performance, and a literature review on the QLEDs stability.

- **Chapter 3:** Explaining the experimental methods for device fabrication and introducing the device characterization methods.
- **Chapter 4:** Provides results of studying the shelf life of B-QDs' PLQY, and interactions between the B-QDs and ZnMgO ETL that lead to some PL quenching. Analysis and explanations for the shelf life degradation phenomenon of the B-QDs PLQY are provided.
- **Chater 5:** Presents the results of studying the electrical stability of B-QDs' PLQY under electron or hole current flow in EODs and HODs. Also, it presents findings on replacing the HTL in B-QLEDs to address HOD electrical stability issue. Additionally, it includes results of green QLEDs (G-QLEDs) using the two HTLs.
- **Chapter 6:** Investigating the charge injection changes during the B-QLEDs operation under the bias and its influences on the charge balance and EL stability.
- **Chapter 7:** Highlighting a degradation mechanism occurring in B-QLEDs, originating from the excess holes leaking into the ZnMgO layer.
- **Chapter 8:** Provides an overview of the thesis and summary of the conclusions, plus, the potential research domains and clues for prospective studies.

Chapter 2

Fundamentals of QLEDs and Literature Review on QLEDs Stability Issues with the Proposed Solutions

This chapter briefly introduces QDs structure followed by an explanation of the working principles of QLEDs and their architecture evolution. Later in this chapter, a literature review is presented summarizing the QLEDs' stability issues and the reported solutions for addressing the stability problems.

2.1 Quantum Dots

2.1.1 Quantum Confinement

The appealing optical properties of QDs for luminescence stem from the quantum confinement of electron-hole pairs known as exciton in QDs. Excitons are bound states resulting from Coulombic attraction between an electron and a hole. In bulk materials, the exciton radius can be characterized by using Bohr radius of a hydrogenic atom and is determined by the following equation[14]:

$$a_B = \frac{4\pi\varepsilon_0\varepsilon_r\hbar^2}{m_r^* e^2} = \frac{\varepsilon_r m_e}{m_r^*} \times (0.53\ \text{Å}) \qquad (2.1)$$

Where ε_0 is the vacuum permittivity, ε_r is the permittivity of the medium m_r^* is the reduced effective mass of the electrons and holes, e is the elementary charge, and m_e is the mass of a free electron. When the material dimension reduces below its Bohr radius like in most QDs, the QD quantum confinement effects appear, and the excitons are confined within the QD. In the QDs that have sizes below the Bohr radius, quantum confinement effects lead to a discretized density of states. The quantization of energy states is derived from the Schrödinger equation for a spherical, three-dimensional, infinite quantum

well system. Further details and solutions are available from the referenced sources[15-16]. Therefore, the energy state for the ground state of a spherical quantum dot is described by:

$$E_{n=1} = E_{g,bulk} - \frac{e^2}{2\varepsilon_0 \varepsilon_r . a_B} + \frac{\pi^2 . \hbar^2}{2m_r^* . r^2} \quad (2.2)$$

Where $E_{g,bulk}$ is the bulk material bandgap energy, r is the QD's radius, the second term represents the Coulombic interaction between the confined electron and hole, and the third term represents the confinement energy of the electron and hole. From the equation, one can see the quantum confinement effect ($r < a_B$) leads to a discretized density of states (DoS) in the material. Therefore, the bandgap energy changes as the material's radius changes, and the exciton energy in QD is always greater than that in the bulk material. The exciton energy in QD is referred to as bandgap energy in this work for convenience.

As shown in **Figure 2.1a**, confinement in each direction leads to a delta-function-form for the DoS *vs.* energy in that direction, and ultimately the QD possesses confinement and discretized DoS in all three directions. Consequently, one of the appealing features of QDs, which is size-dependent emission peak, stems from adjusting the QD's bandgap by altering the QD size. As shown in **Figure 2.1b**, the smaller the QD size is, the larger the bandgap would be and, in this way, the QD emission peak can be made to range from visible to infrared. Moreover, the discrete available DoS in QDs contributes to a narrow emission spectrum (FWHM <30 nm), making them superior to organic luminescent materials (FWHM ~ 50 nm), providing the opportunity to obtain saturated colors and maximizing the color space for displays[17].

a)

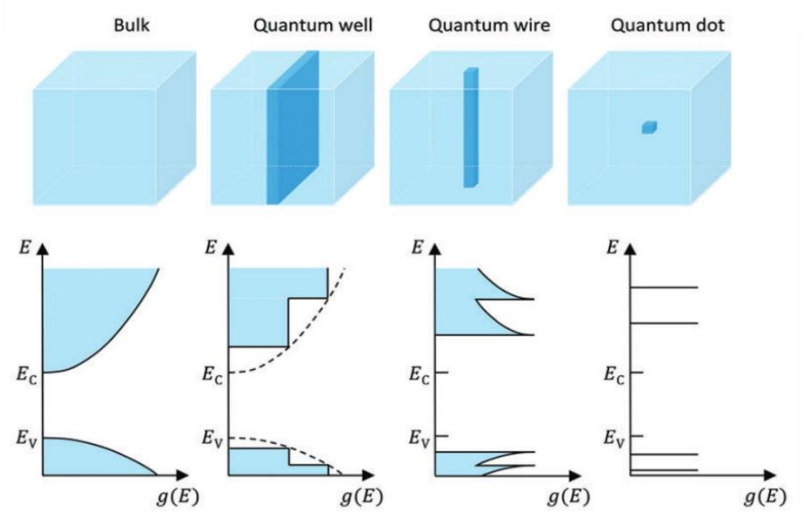

b)

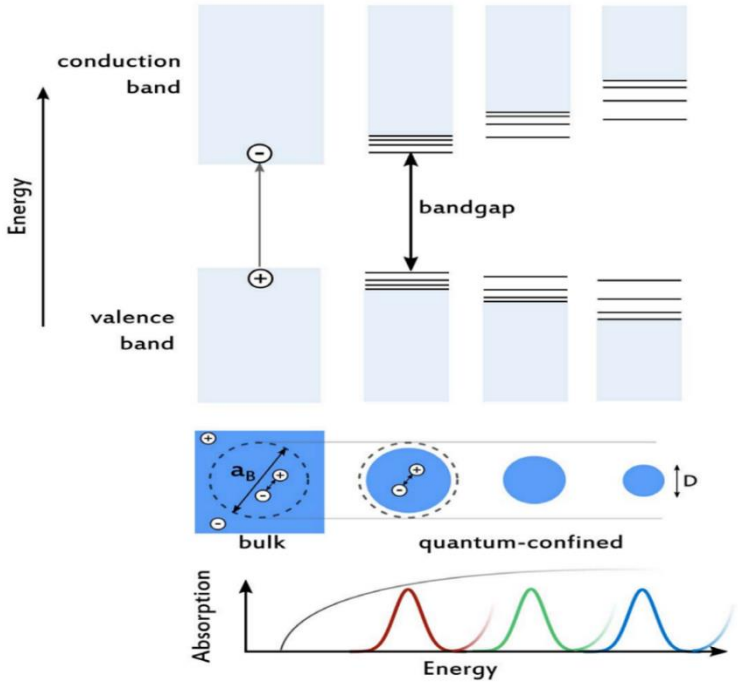

Figure 2.1 a) Changes in the density of states by reducing the material dimension[18]. b) Illustration of quantum confinement effect depending on the dimension[19].

2.1.2 Colloidal Quantum Dots

QDs can be synthesized in the solution phase or solid-state phase. To get the QDs in the solid phase, they can be incorporated into thin films or be embedded within glass substrates using techniques like molecular-beam epitaxy (MBE), metal-organic chemical vapor deposition (MOCVD), and ion beam implantation. However, in the solution phase wet chemical processes are employed to create colloidal QDs. Synthesis methods for QDs can also be categorized as either top-down or bottom-up approaches. Top-down techniques involve reducing the size of bulk materials as seen in MBE, while the bottom-up method involves chemical synthesis processes like MOCVD or wet chemical methods[20]. In this study, all discussed QDs are colloidal suspensions synthesized by wet chemical methods, facilitating their integration into QLED fabrication through cost-effective solution-based processes. During the synthesis, there will be a size distribution for QD particle size that may cause a broadening in the QD optical spectra. Despite that, QDs still own narrow emission spectra with FWHM <30 nm.

2.1.3 Quantum Dots Composition

QDs can be synthesized with a variety of materials. Semiconductors like Si, C, CdTe, and PbS are utilized in various fields such as photovoltaics, sensing, and biological applications. However, CdSe has attracted considerable attention due to its potential for light emission. With a bulk bandgap of 1.74 eV, CdSe offers flexibility in covering the visible spectrum by adjusting the size of QDs[21-24], as shown in **Figure 2.2**. QDs' excellent optical properties depend on factors such as their structure and composition in addition to their size.

Initially, QDs were synthesized in a core-only structure but the photoluminescence quantum yield (PLQY ~ the number of emitted photons relative to the number of absorbed photons) was low. Consequently, QDs have been engineered to adopt a core/shell structure. In this design, a small inorganic semiconductor (core) like CdSe is typically surrounded by a wider-band gap inorganic semiconductor (Shell) such as ZnS, CdS, and ZnSe. The purpose is to passivate the light-emitting core, boosting its ambient stability, reducing defect states, further confining the carriers/excitons on the core, and thereby increasing the emission yield.

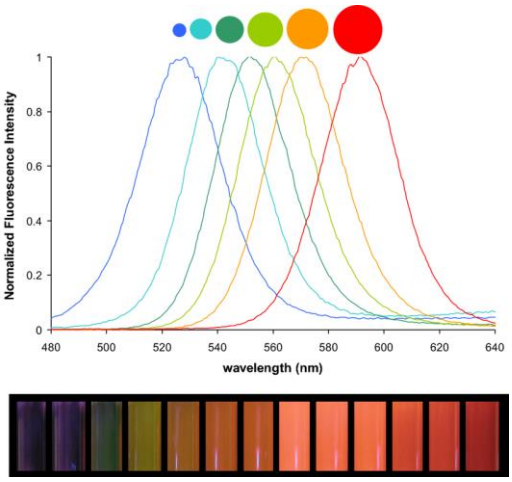

Figure 2.2 Size-tunable fluorescence spectra of CdSe QDs of different sizes. The bottom bar shows the colloidal suspension of the QDs under UV light[25].

The core/shell structure, depicted in **Figure 2.3**, offers various configurations, including abrupt, alloyed, or with intermediate shell [26]. The thickness of the shell is a critical parameter since in the close-packed QD films, the probability of Forster resonance energy transfer (FRET) increases. FRET is a non-radiative transfer of energy from an excited QD to the nearby acceptor QD. This phenomenon leads to a decrease in the PLQY of the QD film. The FRET is strongly influenced by the distance between the adjacent QDs and using thick shells can mitigate FRET, however, excessively thick shells can adversely affect carrier injection efficiency.

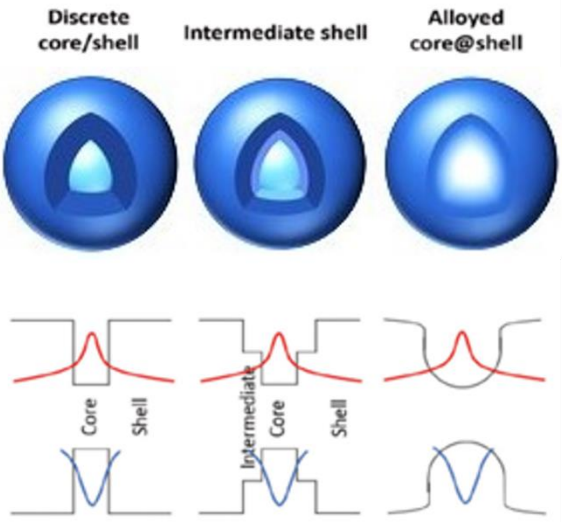

Figure 2.3 Schematic of shape, energy band diagram, and electron-hole wavefunctions in QDs[26].

Core/shell-structured QDs can be categorized as core/multi-shell QDs and alloy-structured QDs. The common feature of both is the use of wide bandgap ZnS as the outermost shell. In the first case, an intermediate semiconductor is used to reduce lattice mismatch and the common structures are (CdSe/CdS/ZnS or CdSe/ZnSe/ZnS). This structure can improve PLQY and the stability of QDs. However, for B-QDs, considering the practical limitations on controlling the synthesis reaction, having the core CdSe with the size of ~ 2nm, the alloyed structure is reported as a better choice. The gradual change in chemical composition results in gradient change in energy bands that facilitates carrier injection and exciton formation. It also alleviates lattice mismatch and greatly improves PLQY by reducing interface defects and non-radiative recombination. The synthesis process is progressed to achieve relatively high PLQY for blue B-QDs using similar Cd-based semiconductors to red/green QDs. However, due to a large surface-to-volume ratio and large exciton energy in B-QDs, achieving efficient carrier injection/confinement is challenging in B-QLEDs' efficiency and stability[27].

In colloidal QDs, the shell surface is covered by organic ligands using a range of chemical groups that anchor to the QD in order to stabilize them in the dispersion in the liquid phase and prevent aggregation. **Figure 2.4** shows a schematic of colloidal QDs with core/multi-shell structure and ligands. With the decrease of QDs size approaching the size of blue emitting QDs, the surface-to-volume ratio increases which results in a large amount of unsaturated dangling bonds and surface defects states. The surface defects states can capture the carriers or excitons and increase the risk of non-radiative recombination and reduce the QDs PLQY. Therefore, ligands can play different roles like stabilizing QDs in the dispersion, passivating surface traps thereby suppressing trap-assisted quenching of the QDs, preventing QDs from water and/or oxygen degrading species, and lastly, ligands can affect the charge transfer properties of the QD films. Therefore, particularly for B-QDs, there is a trade-off in appropriate QDs structural design between the stability and maintaining high PLQY of QDs and at the same time, improving charge injection efficiency into B-QDs. With all the improvements in synthesis methods, the PLQY of B-QDs is practically comparable (still less than) that of red and green QDs unless a very thick shell is used for B-QDs to improve the PLQY, which negatively affects charge injection efficiency[28].

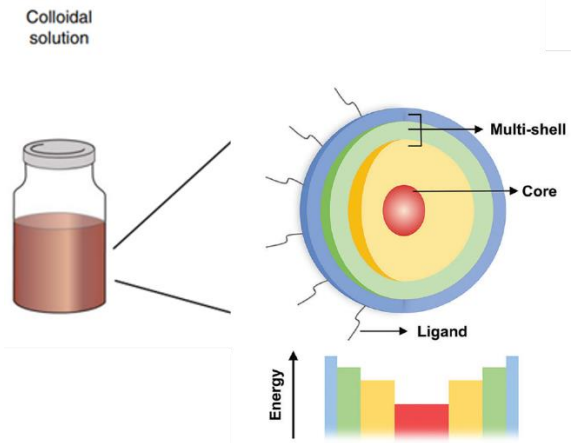

Figure 2.4 A schematic of colloidal QDs with core/multi-shell structure with ligands and energy alignment[28-29]

Typically, colloidally synthesized B-QDs are covered by bulky acids i.e., Oleic Acid (OA) with long carbon chains. Although they are advantageous in terms of strong attachment to QDs during the purification process in the synthesis, better QDs' ambient stability, and increased inter-QD distances leading to high PLQY, they reduce QD conductivity and affect the charge injection/transport within the QD layer. Therefore, ligands not only affect the PLQY of the QDs but also the electroluminescence properties; and the choice of appropriate ligands can improve the QLED performance. Also, the replacement of original ligands with shorter conductive ones is an approach to improve charge balance or balanced electron-to-hole injection ratio in the device[26].

2.2 Auger Recombination

Excitons can relax via either radiative transition or non-radiative transition, also known as exciton quenching, in the former photon is emitted, which is the underlying mechanism in photoluminescence while in the latter no photon is produced. To achieve high efficiencies in QLEDs, it is required to minimize the non-radiative transitions. Auger recombination is one of the most common processes in which exciton quenching occurs. In Auger recombination, the exciton energy is transferred to a third particle such as an electron or hole. Depending on the third particle charge carrier type the recombination pathway could be positive or negative trions. In nanoscale materials opposite to bulk materials, Auger recombination is highly efficient due to the conserved momentum condition. Auger processes are different in direct- and indirect- semiconductors, in direct semiconductors it occurs with only three-particle trions while in indirect semiconductors a photon emission or absorption is needed to satisfy the momentum conservation. Due to the small size and large surface area of QDs, charge

density on QDs can be high under high current density which accelerates the interaction of more than two particles through the Auger process[29-31].

2.3 QLEDs Operating Mechanism and Architecture

2.3.1 QLEDs Operating Mechanism

The structure of QLEDs consists of a stack of materials, each with distinct roles. A typical architecture involves layers arranged as Anode/HTL/QD/ETL/Cathode. In this structure, the anode and cathode are the electrodes for hole and electron injection, respectively. The HTL and ETL are the hole transport layer and electron transport layer, respectively to transfer the carriers to QDs where the light is produced by radiative electron-hole recombination. Sometimes depending on the materials energy levels, a hole injection layer (HIL) between the anode and HTL, or an electron injection layer (EIL) at the ETL/cathode interface is needed to facilitate charge injection from the electrodes. The operating principles of QLEDs have high similarities with OLEDs which involve three steps: (a) charge injection in which electrons and holes are injected from the cathode and anode of the device into charge transport layers (CTLs). (b) charge transport in that the injected carriers travel through the CTLs and enter the emission layer (EML) due to the applied electric field. (c) exciton formation and radiative recombination referring to electron-hole pairs formed by Coulombic interaction between electrons and holes. Eventually, the generated photon escapes from the planar structure contributing to light emission. The operating principles are shown in **Figure 2.5**.

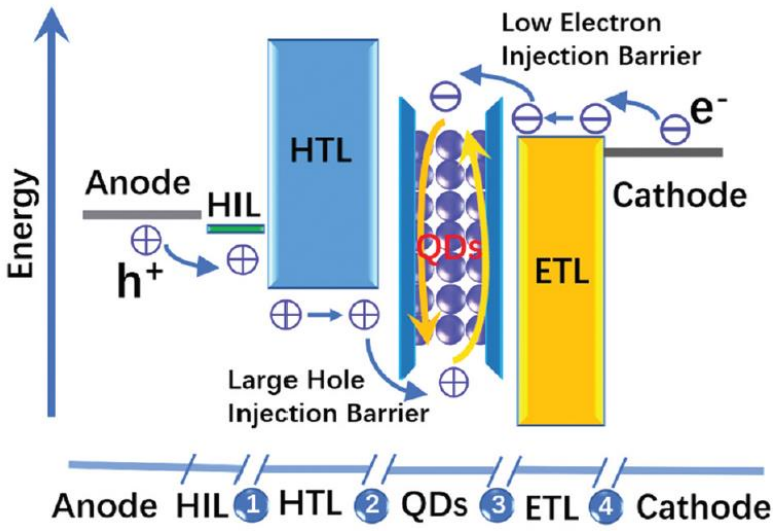

Figure 2.5 A schematic diagram of a QLED operating mechanism[27]

Excitons are generally unstable and relax to the ground state either by radiative recombination where the exciton energy is released by photon or non-radiative recombination releasing the energy in the form of heat. The efficacy of these processes can be significantly impacted by the optoelectronic characteristics of the CTLs, including their band structure, work function, conductivity, intragap states, and optical properties. For instance, the conductivity of CTLs and the energy-level alignment at the interfaces of electrodes/CTLs and QD/CTLs play a crucial role in governing charge injection efficiencies.

The efficiency of carrier injection is highly dependent on the magnitude of the injection barrier (i.e., the energy difference between the highest occupied molecular orbital (HOMO) of the HTL and the valence band maximum (VBM) of the QDs for hole injection and the energy barrier between the conduction band minimum (CBM) of inorganic ETL and that of the QDs for electron injection). Therefore, the choice of appropriate CTLs is important in QLEDs performance to ideally satisfy the minimum energy barrier for electrons/holes accordingly and supply enough charges so that the electron/hole injection into QD is balanced[28].

Furthermore, it is essential to carefully choose CTLs to ensure effective charge confinement within the QD layer. The selection of CTLs should prioritize their ability to block countercharge carriers

effectively. In addition, the suitability of CTLs is determined by considering the material's solution-processability for all-solution-processed QLEDs. In this regard, it is crucial to ascertain that the solution-coated CTL films exhibit stability, continuity, and absence of pinholes while allowing for their thickness control. This consideration extends beyond solvent orthogonality to encompass the formation of reliable, uniform, and controllable films[32].

2.3.2 QLEDs Architecture Evolution

The QLEDs device structure has gradually matured and is in part inspired by OLEDs. The QLEDs device structure evolution is shown in **Figure 2.6**. In their first emergence in 1994[10], QDs mixture with an organic hole transport polymer was sandwiched between the electrodes leaving the QDs as both an EML and ETL which is a type I structure. Although this device realized the electroluminescence from QDs, the organic polymer was not sufficiently blocking the electrons and the main recombination zone was in the organic polymer. In 2002[33], Loudon et al. introduced Alq_3 as ETL in QLEDs. They used a single QD layer sandwiched between two organic CTLs and electrodes as in a type II structure that improved the efficiency of the device. In 2008[34], Bulovic et al. incorporated inorganic CTLs for QLEDs and could obtain an EQE of 0.5% which is called a type III device structure. Later in 2011[35], Qian et al. used ZnO nanoparticles (NPs) as ETL, keeping the organic HTL, making a hybrid organic-inorganic device, i.e. type IV, which led to a great increase in current density[8]. Both type II and type III structures have their own advantages and disadvantages that type IV structure benefits from the advantages of both as a compromise leading to the best QLEDs efficiency and brightness to date[28].

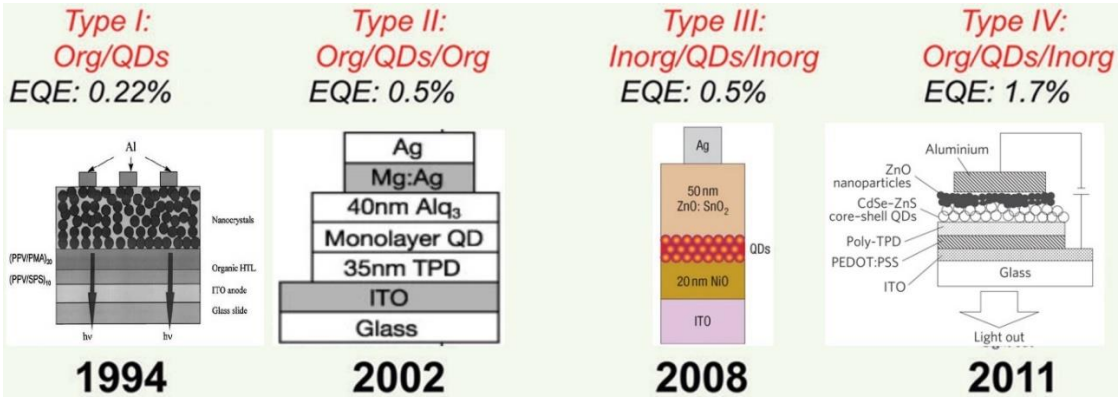

Figure 2.6 Cd-based QLEDs device structure evolution over time[29]

It is worth mentioning that the hybrid organic-inorganic device structure not only has efficient charge injection into QDs, but it also effectively confines charges into the QD layer preventing significant leakage. However, hybrid device architectures are not ideal yet regarding the charge balance since the recombination zone will be toward the CTL/QD interfaces, depending on the type of excessive carrier[8].

To meet different application requirements, different QLED structures are developed. As illustrated in **Figure 2.7**, QLED architecture can generally be classified according to the direction of EL emission or the polarity of the bottom electrode. Typically, one of the electrodes is transparent to transmit the generated light in the QD layer out of the device. One of the most commonly used transparent electrodes is indium tin oxide (ITO)[18]. In an upright structure, ITO is employed as an anode due to its high work function which enables efficient hole injection. When the bottom ITO is employed as the cathode, the architecture is considered an inverted structure. QLEDs with the inverted structure are advantageous for display applications since the bottom transparent cathode can directly be connected to the thin-film transistors (TFT) backplanes[36].

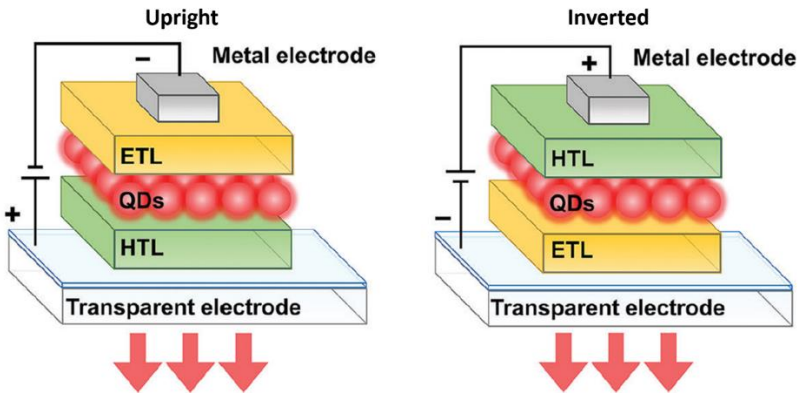

Figure 2.7 Classification of QLEDs structure in terms of the bottom electrode polarity[29].

2.3.3 Materials in QLEDs

Throughout the significant number of efforts for improving the QLEDs' efficiency and stability, a hybrid multilayered structure has been established for QLEDs, discussed earlier as a type IV structure. This architecture is designed to enable efficient electron and hole injection into the QDs EML from the cathode and anode, respectively. Due to the large energy level offset between QDs and electrodes, providing a stepwise pathway for charge injection is essential for efficient charge injection into QDs.

This requires the use of charge injection/transport layers with suitable energy levels on the carrier pathways between the electrodes and the QDs. Moreover, the performance of QLED is strongly contingent upon the stability of materials. Depending on the chosen device architecture, whether upright or inverted, the deposition sequence of materials and the associated considerations vary. For example, the first CTL coated beneath the QD layer must have resistance to the QD organic solvent. In this regard, small molecule CTLs are often unsuitable due to their susceptibility as most of them can be affected by the QDs' organic solvent. However, the CTL beneath the QD layer can undergo high-temperature annealing if necessary. Another critical consideration is that the layers coated subsequent to the QDs deposition should have a low-temperature annealing to avoid the QDs damage in addition to solvent orthogonality. Therefore, the choice of materials plays a key role in QLEDs' efficiency and stability.

2.3.3.1 Quantum Dots

QLED performance relies on various factors among which the QD PL is of high importance. Precise control of QDs optoelectronic properties is done based on composition, structure, and surface chemistry optimization. An in-depth understanding of exciton dynamics within QDs is also pivotal to enhancing the performance of QLEDs.

With the decrease of size, the surface-to-volume ratio of QDs increases until the B-QDs owning a smaller size than the other primary colors of red and green, have the largest surface-to-volume ratio. Thus, the surface of QDs has unsaturated dangling bonds that create defect states and are favorable to receive carriers or excitons that act as non-radiative recombination centers. Surface passivation techniques are effective in improving the fluorescence characteristics and stability of QDs. In this regard, using a wide bandgap shell together with using organic chemicals as surfactants is useful for QDs surface passivation.

To have an appropriate material selection for the shell of the QDs, in addition to the energy level alignment, it is also important to match the core material in terms of crystal structure and lattice constant. Otherwise, the stress at the core/shell interface leads to defect states that quench the QDs PLQY. For example, Klimov et al. proposed inserting an intermediate layer for the CdSe core with continuous grading of $CdSe_XS_{1-X}$ at the core/shell interface[37]. They showed that the QDs PLQY greatly increased since a smooth composition change relieves the strain caused by lattice mismatch, thereby preventing non-radiative recombination. For the outermost shell of QDs, the wide bandgap ZnS is

extensively used, and considering the gradient alloyed composition, QDs mostly end up having CdZnSeS/ZnS composition to minimize the lattice mismatch and possess exciton confinement.

Moreover, the surface chemistry of QDs also plays a crucial role in QDs PLQY. For instance, Brown et al. showed that the ligands capping the QDs can change the QDs energy level up to 0.9 eV by creating synergistic effects of dipoles induced by QD-ligand interactions or the ligands molecules themselves[38]. Li et al. reported that replacing the long-hydrocarbon Oleic Acid (OA) ligands with short conductive chloride (-Cl) ones changes the inter-dot distances thereby affecting the charge transport properties of the QDs and changing the charge injection efficiency[39]. Thus, in addition to surface passivation and preserving the QDs PLQY, ligands can influence the carrier mobility and charge injection efficiency in the QD layer.

In summary, QD structure optimization strategies revolve around three main directions: i) employing alloying structures to suppress non-radiative recombination, ii) introducing strong confinement to mitigate field-induced exciton dissociation, and iii) controlling QD energy levels through modification with various ligands.

2.3.3.2 Charge Transport Layers (CTLs)

In general, the characteristics of CTLs such as work function, band structure, conductivity, intra-band states, and optical properties significantly affect the efficiency of the EL process in QLED operation. Consequently, the chemistry of CTLs must be versatile and robust, enabling systematic and tailored engineering of their optoelectronic attributes as needed. An ideal device structure should not only have balanced carrier injection to mitigate carrier-induced quenching but also establish inert interfaces to suppress the negative effects of surrounding CTLs.

Given that the mobility of electron or hole carriers is different in commonly used ETL or HTL, respectively, device structure design can focus on two primary objectives: enhancing charge injection balance and restricting the quenching effects induced by the CTLs. Furthermore, an appropriate choice of CTL should support an effective blockage of the counter carrier to minimize the leakage current in the device. The imbalance charge injection results in either charge accumulation at the QD/CTL interface or the excess charges may charge the QDs and leak across the counter CTL. Both of these phenomena lead to exciton quenching and efficiency loss.

In the recent state-of-the-art hybrid QLEDs, organic small-molecule or polymer HTLs are used. In case of QLEDs, 4,4′-Bis(N-carbazolyl)-1,1′-biphenyl (CBP)[40] and tris(4- carbazoyl-9-ylphenyl)amine (TCTA)[41] for small molecules, and poly(9,9-dioctylfluorene-alt- N-(4-sec-butylphenyl)-diphenylamine) (TFB)[12] and polyvinyl carbazole (PVK)[42] for polymers are some examples of the most popular organic HTLs which are widely used.

The mobility of holes within these materials is crucial for effective hole transport through the HTL. Additionally, the HOMO level plays a critical role in facilitating efficient hole injection at both the interfaces of HTL/anode and QD EML/HTL. On the other hand, a shallow LUMO level can be advantageous in creating a higher energy barrier for electrons at the junction of QD EML/HTL and electron leakage blockage.

Particularly in B-QLEDs, due to the wider bandgap of B-QDs compared to other colors, it is more important to find a better energy-level match between the HOMO of the HTL and the VBM of B-QDs. Having a wider bandgap in B-QDs doesn't necessarily mean that the HTL with the deepest HOMO level is the best match for B-QLEDs. This is because as the bandgap of QDs changes due to composition, the energy levels might also shift upward. In addition, hole mobility is another key factor. In summary, there is still an open debate in the field about whether holes or electrons are the easily injected carriers in B-QLEDs. Although it is a complex system with entangled factors affecting the choice of CTLs to finely optimize the charge balance, TFB with relatively high hole mobility compared to other organic HTLs has been a good candidate for use in B-QLEDs that results in high device efficiency. Thus, although an ideal hole transport material should possess high hole mobility along with deep HOMO and shallow LUMO levels, the criteria may differ depending on the QD EML energy levels or the ETL used in the device.

Compared with the organic ETLs, ZnO as an inorganic ETL has superior properties like high conductivity, excellent electron transport efficiency, and well-matched energy levels with Cd-based QDs for electron injection. However, since its electron mobility is higher than hole mobility in most organic HTLs, an overload of electrons happens in QLEDs. To address this issue, doping of metals into ZnO is suggested to manipulate the sub-bandgap defect states, work function, bandgap, and mobility. To have efficient electron injection into wide bandgap B-QDs, it is essential to use Mg-doped ZnO or ZnMgO due to its shallower work function which reduces the energy barrier for electron injection into

B-QDs. In **Figure 2.8**, the energy levels of some of the commonly used materials in hybrid QLEDs are presented.

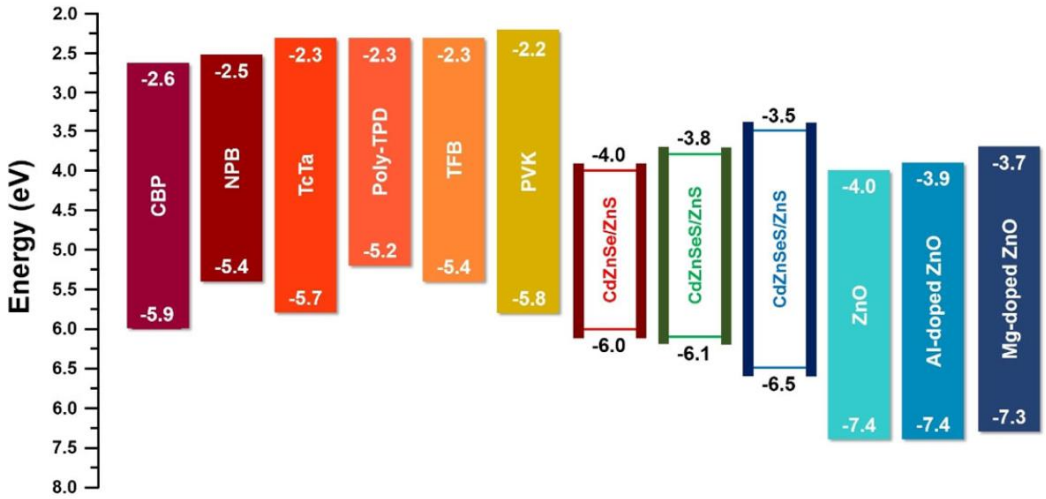

Figure 2.8 Band energy levels of some of the commonly used CTLs and alloyed QDs[43].

2.3.4 Factors Determining the QLEDs Performance

The performance of QLEDs is evaluated by two key factors: efficiency and EL stability. Efficiency provides insights into the device operation mechanism quality that leads to photon emission and photon output from the QLEDs. Stability, however, pertains to the duration over which the QLED can uphold its EL characteristics during continuous operation, indicating that efficiency is maintained throughout its operation which also requires maintaining its efficiency in storage. This section provides an overview of parameters for the assessment of QLEDs performance.

2.3.4.1 Luminance

Luminance refers to luminous intensity per unit area of light traveling in a given direction. It describes the amount of light that is emitted from a particular area and falls within a given solid angle. This parameter indicates how bright the surface of a light source is to the human eye from a particular angle of view that considers the eye's sensitivity to different wavelengths. Luminance is a tool to measure the fluorescence from a light source and is expressed in cd/m^2.

2.3.4.2 EL Efficiency

To compare the efficiency of different color-emitting devices based on identical criteria, external quantum efficiency (EQE) is used. In QLEDs, the EQE represents the number ratio of photons that get emitted from the device to the carriers that get injected into the device under the electrical bias and is described by:

$$\mathrm{EQE} = \mathrm{IQE} \,.\, \eta_{\mathrm{OC}} = \gamma\chi\eta_{\mathrm{r}}\eta_{\mathrm{OC}} \qquad (2.1)$$

Where IQE, η_{OC}, γ, χ, and η_{r} are the internal quantum efficiency, the ratio of the light out-coupling efficiency, the charge balance factor, the fraction of excitons with an allowed radiative transition, and the photoluminescence quantum yield (PLQY) of the QDs, respectively. For Cd-based QDs, $\chi \approx 1$ is not uncommon, and is a primary factor in the strong interest in these materials[7]. IQE is associated with γ and η_{r} that shows how many photons are produced through excitons radiative recombination with the injected electron/holes from the electrodes. Out-coupling efficiency quantifies the percentage of photons extracted from the internal structure of the device, typically falling within the range of 20% to 30%. This metric encompasses various photon interactions within the device, such as cavity effects, as well as reflection and refraction across its multiple stacked layers.

Other figures of merits for QLEDs efficiency are current efficiency (CE) and power efficiency (PE). Current efficiency is defined as the required current density to pass through the device area to produce a certain luminance and is expressed in candelas per ampere (cd/A). In addition, power efficiency quantifies the ratio of the luminous flux produced by a light source relative to the consumed electrical input power, which is expressed in lumens per watt (lm/W).

2.3.4.3 Electrical (Operational) Stability

During the operation of QLEDs, the luminance gradually decreases induced by different degradation phenomena. Device stability is expressed as a lifetime parameter LT X (or T_x), which indicates the time elapsed for device luminance to degrade from its initial value (L_0) to X% of it under continuous constant electrical driving. Often, the lifetime of QLEDs is defined as half-lifetime (LT50). The comparison of QLED stability is reported by lifetime measurements which are typically carried out at a constant current density with different initial luminance and driving voltages. In this case, the number of injected carriers is kept constant and the initial luminance values are reflective of the number of excitons being

recombined in the device. The driving voltage trend while the device aging can depict the electric field applied to the device during the degradation.

To compare the QLEDs' lifetime, the initial luminance is an important factor that should be considered. The initial luminance of 100 cd/m^2 or 1000 cd/m^2 are the conventional values that are used to report the QLEDs' lifetime. Other than comparison, for highly stable devices such as red QLEDs(R-QLEDs), it's not practical to wait such a long time for the device to degrade. Therefore, the equation below is used to convert the equivalent lifetime of QLEDs and extrapolate the results at the same initial luminance[36].

$$(L_a)^n\,(t_{x\%}) = (L_b)^n\,(t'_{x\%})\,, \quad 1 < n < 2 \tag{2.2}$$

Where, L_a and L_b are two different initial luminance values, n is the exponential luminance dependence of the device luminance decay, which can vary within the range of 1.5 to 2.5 depending on the degradation mechanism, and t is the time it takes for the luminance to decay from the initial luminance value to x percent of that value.

Progress in QDs synthesis and device architecture engineering to date has led to significant progress in improving the EQE of QLEDs [12, 28, 44-48]. QLED degradation is a complex issue, and device stability generally depends on the choice of materials, device structure, fabrication process, and operation and storage conditions.

In terms of QLEDs electrical stability, T_{50} lifetimes, here defined as the time elapsed under electrical bias before the EL intensity of the QLEDs decreases to 50% of the initial value of 100 cd/m^2 exceeding 2,300,000 h[12, 49-50] have been demonstrated in red- and green-emitting QLEDs. The electrical stability of B-QLEDs (T_{95} @ 100 cd/m^2~ 4400 h) however remains far below that of their red and green counterparts and technology requirements[47, 51-54], and continues to be an obstacle for QLEDs commercialization. A major factor behind the limited success in addressing the B-QLEDs' poor stability issue is the fact that the underlying degradation mechanisms remain largely unknown or not well understood.

Knowing that charge imbalance is inherent in QLEDs, it is still not clear whether electrons or holes are in shortage or excess condition in the case of B-QLEDs whereas the electrons are known to be the excess carriers in R-QLEDs using ZnO as the ETL. As the QD emission peak moves toward the shorter wavelengths e.g. B-QD, the bandgap of the core increases, meaning that the potential well margin

between the core and the shell shrinks, leaving a lower potential barrier for carrier confinement in the QD. Therefore, since the carrier confinement is more difficult to be established in wide bandgap B-QDs rather than R-QDs, there is a possibility that both carriers are hard to be confined in B-QDs. However, there is still a lack of knowledge of the main degradation factors and the strategies to address them in the case of B-QLEDs. This thesis predominantly focuses on systematically studying the root causes of B-QLEDs' poor stability comprising the shelf life and operational stability of upright B-QLEDs, through a comprehensive targeted analysis of the stability of the materials used in the device stack, charge injection mechanism, and the reversibility of the changes occurring during the device operation.

2.3.4.4 Shelf Life

For practical applications, a very long shelf life is necessary for the QLEDs after fabrication. The QLED efficiency changes over time in storage implies the device has a short shelf life. Moreover, a long shelf life is also a prerequisite for high operational stability. Due to the interaction of the layers in the device stack, the QLED EL efficiency may change over time. Chemical redox reactions, diffusion or intermixing of the layers, or changes in chemical or physical properties of the layers may occur and sometimes be accelerated by external ambient moieties that influence the device's shelf life. The QLED changes happening over time without bias can be either spontaneous or induced by factors such as encapsulation. Regardless of the changes being positive i.e. efficiency increase or negative i.e. efficiency decrease, the changing behavior is not favorable for devices considered to have a long shelf life. Although it seems encapsulation is necessary for the device's stability to protect them against ambient species, it is one of the known factors that can influence the QLEDs' shelf life through positive aging and negative aging processes via not very widely known mechanisms. Therefore, there is a space to further study the shelf life of QLEDs and investigate alternative approaches to avoid encapsulation or optimize the encapsulation procedure or sealant material to stop the QLEDs changing behavior.

2.4 Literature Review

EL stability is commonly influenced by a combination of external and internal factors. External factors pertain to the surrounding environment, including elements like moisture, oxygen, UV light, and so forth[26]. These factors are typically addressed as engineering challenges and can often be mitigated through suitable encapsulation methods. Conversely, internal factors primarily involve degradation stemming from inherent alterations within the functional materials and interfaces. This

aspect poses a notable hurdle in stability research. In this section, we delve into the mechanisms of degradation reported in the literature.

Some QLED degradation mechanisms have been reported in the literature. These include chemical or morphological changes in the organic materials[55], QD chemical degradation[51] e.g. ligands detachment, and QD charging[56] are some of the involved factors that are introduced, originating from inherent charge imbalance. In addition, trap/defect states in the adjacent layers or at the interfaces of the QD film are also considered to play a detrimental role in the QLEDs' EL stability.

Therefore, the mechanisms proposed to describe the QLEDs degradation are namely: creation of quenching sites, leakage current, and electrochemical reaction causing damage to the functional layers or their interfaces. The film's morphology and chemical properties may also be changed due to storage time, long-term electrical stress, or Joule heating.

Some of the effects discussed above can be either spontaneous or induced by electrical stress during the device's operation. Due to the materials' interactions, effects of oxygen and moisture in the atmosphere, ion migration, or encapsulation the shelf life of the QLEDs may also be affected. These factors have consequences such as morphology changes, intermixing of the layers, electrochemical reactions, changes in QDs' chemistry, increase in defect density of states influencing the shelf life.

In this section, a review of some of the QLED degradation issues and the proposed strategies to address them are discussed. The reports can be mainly attributed to QDs PLQY stability, CTLs, and encapsulation affecting the shelf life of the QLEDs. This chapter covers the studies regarding the QLEDs' aging mechanisms and the effective methods used for QLEDs' lifetime improvement. The main focus though is on the challenges in B-QLEDs which limit their EL stability.

2.4.1 Operational Stability

2.4.1.1 QDs PLQY Stability

Due to the significant efforts in colloidal QD structure and composition optimizations, very high i.e. near unity, PLQY values are achieved in all colors. However, the stability of high PLQY values for QDs as a thin film in QLEDs is a crucial factor in the device's shelf life or electrical stability. The EL characteristics of QLEDs can be affected, permanently or temporarily, under operation through mechanisms such as QD charging, CTLs degradation, and Joule heating.

Imbalanced charge injection into QDs during QLED operation is unfavorable as it leads to QD charging. It is well known that the multi-carrier state of QDs leads to Joule heating and as a result, introduces QD damage. Especially at higher current density bias, Joule heating significantly reduces the device stability temporarily due to thermal-induced emission quenching or permanently if it continues due to QD chemical damage. Additionally, the excess electron injection, for example, causes electrochemical reactions in QDs and damages it. Moreover, the elevated temperature can lead to ligands debonding and consequently, defect increasing. To mitigate the excessive heating effect, 1-dodecanethiol (DDT) ligands are adopted with higher binding energy to the QDs surface compared to the conventional OA ligands[35]. Besides that, excess carrier injection of one type initiates electrochemical reactions that degrade the QDs PLQY. Using electrochemically inert ligands for QDs can effectively address this issue[30].

In addition, excess carrier injection into QDs forms trions which facilitates non-radiative Auger recombination. For example, Bae et al. showed that in R-QLEDs, the initial stage of device degradation is because of QDs being negatively charged due to excess electron injection, and after cooling the device or a long rest time, the observed PLQY drop is reversed[56]. They also showed that continuous excess electron injection leads to a leak into the HTL and irreversibly degrades the HTL due to the decomposition of chemical bonds.

QDs PLQY can also be affected by oxygen and/or moisture in the presence of light. CdSe-based QDs are reported to show enhanced PL after exposure to light and moisture. This phenomenon is called photoactivation. It is reported that the surface traps are passivated due to the adsorbed water species. Thus, the trapped electrons repopulate to the conduction band of the QDs and band-edge radiative recombination increases. Photoactivation is also reported to occur due to the chemisorbed oxygen. However, long-term exposure to oxygen or moisture irreversibly degrades the QDs PLQY via chemical changes. Oxygen can oxidize the surface of QDs, forming surface trap states, and as a result, cause fluorescence quenching. The competition between the two processes is responsible for the complex kinetics of the change in the QDs PLQY[26, 57-58]. Moreover, QDs are reported to undergo a luminescence enhancement known as photo-enhancement due to photoactivation when irradiated by UV light. It is found that photo-enhancement is faster under UV light compared to ambient light and higher intensity UV accelerates it. However, prolonged exposure to UV light in the presence of oxygen or moisture eventually leads to a decrease in PLQY[59].

There has been a consensus that the primary factor behind the photo-enhancement is smoothing the QD core surface and removal of its defects. However, distinct forms of photoactivation can be discerned based on the approach taken to mitigate surface defects. Furthermore, it is found that each surrounding medium of the QDs induces a unique surface reconstruction or rearrangement of the surface atoms within the nanocrystal.

Furthermore, given that the PL characteristics of QDs are highly sensitive to the surface structure, typically determined by the synthesis techniques employed, the mechanisms underlying the photoactivation process may not be fully identical for different QDs. The specific mechanism governing the photoactivation process might vary among different systems. In other words, since the photoactivation mechanism is not unique, there is a discrepancy and confusion between different proposed explanations by the different research groups.

The studies on the photostability of QDs indicate that the stability of QDs hinges on a multitude of factors stemming from both the intrinsic physicochemical properties of QDs and external environmental conditions. Key determinants include QD size, charge concentration, outer coating bioactivity (comprising capping material and functional groups), as well as oxidative, photolytic, and mechanical stability. These factors, whether considered collectively or individually, play key roles in shaping QD stability. Notably, among these physicochemical attributes, the functional coating and core stability of QDs emerge as prominently significant factors likely to exert substantial influence on QD photostability[59].

2.4.1.2 Hole Transport Layer

2.4.1.2.1 Hole Transport Layer Challenges

Typically, QLEDs consist of organic small molecule HTLs such as CBP, and TCTA or organic polymers like TFB and PVK. Organic materials are inherently less stable than inorganic materials. Studies demonstrate that these materials are susceptible to deterioration and structural deformation when subjected to electrical stress and charge carrier impact, which can create non-radiative recombination centers. The degradation of HTLs is one of the key obstacles to achieving high-stability QLEDs.

It is observed that in R-QLEDs electron injection is much higher than hole injection due to the difference in the electron and hole mobilities of the commonly used HTLs and ZnO as the ETL,

respectively. Therefore, due to imbalanced charge injection into QDs, the holes accumulate at the HTL/QD interface and excessive electrons can leak into the HTL. As a result, HTL degradation is introduced, in some reports, as the reason for QLED degradation[60]. In 2019, Xue et al. proposed that the formation of non-radiative recombination sites created in HTL is the origin of R-QLEDs degradation[61]. A different perception from the negative effect of electrons on HTL is proposed that TFB is oxidized permanently due to the HIL/HTL barrier leading to poor stability in QLEDs[62].

Moreover, it is found that excess electrons flowing to HTL can cause structural deformation of TFB and PEDOT: PSS. To establish charge balance and prevent electron leakage into the HTL, the QD EML is blended with small molecule HTL to improve hole supply for QDs and it could significantly increase the QLED lifetime[63]. Regarding excessive electron injection and its effect on HTL degradation, Jin et al. showed that electron surplus induces electrochemical reactions in HTL leading to the HTL degradation and deteriorating its effective hole injection capability. They compared EL spectra of fresh and aged devices and showed that opposite to the fresh devices, the TFB emission peaks emerge only in the aged devices' EL emission, proving that hole injection efficiency is decreased after aging[64].

Although amenability to fabrication by solution coating processes is an advantage in QLEDs, solvent damage of pre-coated layers, usually HTLs when coating the QD layers continues to be a challenge for material integrity and can negatively affect QLEDs' operational stability. Therefore, in solution-coating, the underlying layer always has to be resistant against the solvent of the subsequent layer, i.e. solvent orthogonality. In upright architecture where the HTL is coated prior to QDs, the choice of QDs solvent and the HTL chemical robustness have to be considered, otherwise, the HTL may be washed off, or at least, the HTL film quality may be affected by the next layer solvent.

In addition to the factors of solvent damage in solution-processed devices and exciton-induced degradation of HTL, charge accumulation is also known to be a reason behind QLED degradation. Charge accumulation at the QD/HTL interface can lead to QD charging or HTL degradation which are detrimental for radiative exciton relaxation in QDs.

2.4.1.2.2 Hole Transport Layer Engineering

Recently, it has been realized that in addition to the reduced hole injection efficiency, electron transfer from QDs to HTL occurs through extra energy states, created in the tail of density of states distribution for HTL, due to the HTL molecule spacial reorganization. Recently, Jin et al. designed a new HTL (PF8Cz) with a shallower LUMO level from TFB due to its robust static molecular structure

and reduced energetic disorder. The synthesized HTL eliminates electron leakage more than TFB which significantly improves blue and green QLEDs stability[12].

Another approach to avoid HTL degradation due to excess electron injection is improving hole injection efficiency. It is proposed that using oxygen plasma treatment for PEDOT: PSS film forms PSS-O bonding that reduces the work function of PEDOT:PSS and therefore, the HIL/HTL barrier decreases[64].

In another example, our group reported that there exist excitons in HTL under bias due to the electron leakage and the organic HTLs undergo exciton-induced degradation that leads to a great loss in QDs PLQY. Therefore, energy transfer from QDs to the quenching molecules that appeared after HTL degradation contributes to QLEDs degradation[61].

In QLEDs that both CTLs along with the QD layer are deposited using a spin-coating process, solvent erosion of the underlying layers affects the device's performance. In 2018, Liu et al. introduced a PVK/TFB double-layer HTL in inverted QLEDs using an orthogonal solvent of 1,4-dioxane. It is shown that PVK with deep HOMO level and TFB with high mobility of (10^{-2} cm^2 V^{-1} S^{-1}) and shallow HOMO level of (-5.4 eV) improves the hole injection into red/green/blue QDs. They claimed that with this double-layer HTL, the highest efficiency until that date is achieved for inverted red, green, and blue QLEDs, and the operating lifetime is increased in the case of R-QLEDs due to the stepwise energy level using double HTL[65].

In addition, some other approaches are often pursued to mitigate the next layers solvent effect including employing materials with sufficient solvent orthogonality, introducing protective interlayers, mixing HTLs, using double-layer HTLs, or adding dopants to stimulate cross-linking of organic HTLs[35, 66-70]. For example, in 2020 Tang et al. introduced a blended HTL of small molecule CBP-V and TFB in order to make TFB get cross-linked. They observed a 7-fold lifetime increase in R-QLEDs using cross-linked blended HTL. The improvements are attributed to the resistivity of blended HTL to solvent erosion and the reduced hole injection energy barrier[67].

To address the charge accumulation issue, it is proposed that by replacing a single CBP HTL with three cascading HTL (CHTL) structures with consecutive steps of HOMO level, the R-QLEDs stability is improved by 25 times. It is because the CHTL restricts the hole accumulation at the QD/HTL interface along with the fact that QD charging is prevented due to the introduction of several interfaces. CHTL also shifts the HTL degradation origin away from the QD layer causing less exciton quenching[40].

In 2021, Shen et al. replaced TFB with PVK in B-QLEDs and observed that the maximum EQE of the devices increased from 10.6% to 15.9% due to a lower hole injection barrier in the case of PVK. However, the operational lifetime of the B-QLEDs reduces with PVK probably due to poor chemical stability of PVK. They also suggest that hole injection is more efficient than electron injection in the B-QLEDs using TFB which is opposite to R-QLEDs where the electron injection is more efficient[54].

2.4.1.3 Electron Transport Layer

2.4.1.3.1 Electron Transport Layer Challenges

Currently, almost all state-of-the-art QLEDs have hybrid (Type IV) architectures in which an organic HTL and an inorganic ETL are used [12, 35, 47]. Recently, ZnO NPs have been widely used for ETL in QLEDs. This is due to their high electron mobility, good hole-blocking properties, and better energy level match with QDs[35, 71-72]. The use of ZnO however leads to some shortcomings. The more efficient carrier injection and transport in ZnO ETL relative to those of their organic HTL counterparts can lead to charge imbalance and decreased efficiency[73-74]. ZnO NPs are also known to have a high concentration of O_2-vacancies that can lead to charge trapping and QDs PLQY quenching[75]. Additionally, the small energy offsets between the QDs and ZnO CBM can induce spontaneous charge transfer at the QD/ETL interface that results in exciton dissociation and efficiency losses[76]. Furthermore, Shim et al. suggest that when ZnO is spin-cast on the QD film, Zn- and O-containing species can diffuse to the QD layer and cause QD charging. Consequently, contamination of QDs facilitates QLED degradation by oxidizing the HTL and QD ligands[77].

Although various studies count the excess electron injection as a challenge in R-QLEDs, there is no consensus on the type of excess carriers in wider-band gap G- and B-QLEDs, using ZnO. Some studies suggest that B-QLEDs are electron deficient and need further electron injection enhancement to obtain stable and highly efficient devices[54, 78-79]. For example, Qian et al. speculated that in B-QLEDs, electrons might accumulate at the QD/ZnO interface raising the voltage drop on ZnO and resulting in B-QLEDs degradation[62].

While ZnO and ZnMgO offer significant advantages in achieving highly efficient QLEDs, many efforts have been directed toward enhancing the stability of QLEDs. This involves addressing the shortcomings stemming from the ETL.

2.4.1.3.2 Electron Transport Layer Engineering

Various approaches for mitigating these shortcomings have therefore been pursued. For example, tight control of ZnO NPs size is used as a tool to fine-tune its bandgap and thus control exciton quenching[71, 80]. Polymeric materials are sometimes also introduced in the ETL, intermixed with ZnO NPs or in a separate layer at the QD/ZnO interface, for the purpose of improving charge balance and reducing interfacial quenching of excitons [66, 81-82]. The incorporation of cations with small atomic radii such as Li, Mg, Ga, or Al into the ZnO NP is pursued to reduce the O_2-vacancy sites in the ETL, regulate the electron mobility and band structure including, the bandgap and energy levels depending on the type and amount of metal dopants[83-91]. In this regard, Mg-doped ZnO (ZnMgO) has been found to be particularly effective in both increasing electron injection and mitigating surface defect-induced exciton quenching due to an up-shifted CBM and reduced O_2-vacancy defects[73-75, 92-95]. According to reports, Mg doping is known to widen the energy gap together with upshifting the CBM and VBM levels versus undoped ZnO. Therefore, ZnMgO is extensively employed as the ETL especially for wide-bandgap B-QLEDs due to facilitated electron injection and reduced defect-assisted exciton quenching compared to ZnO NPs[47, 73, 90].

For example, Li- and Mg-doped ZnO NPs were used by Kim Et al. to achieve high-efficiency QLEDs. Doping Mg or Li increases the bandgap and resistivity, therefore better charge balance is established in the QLED[87]. Likewise, Yang et al. optimized the Mg dopant content in ZnO NP for high-efficiency B-QLEDs. They showed that by increasing the Mg content, the ETL mobility reduces to a better match value to the organic HTL mobility and therefore achieves a better charge balance[91]. The ETL optimization work ended up commonly using $Zn_{1-x}Mg_xO$ (typically called ZnMgO) NPs for efficient B-QLEDs.

In addition, Chen et al[96]. identified an efficiency-loss channel in ZnO ETL involving exciton quenching induced by surface-bound ethanol. They developed a treatment for ZnO NPs to replace the surface-bound ethanol with an electrochemically inert alkali carboxylate. The efficiency and stability of the R-QLEDs were significantly improved by replacing the ZnO NP surfactants due to hindering the potential hole transfer to the ZnO NP layer.

Another study revealed that introducing halide dopants in the ZnO NPs significantly enhances the R-QLEDs' lifetime. It is proposed that halide dopants act as hole scavengers, neutralizing the positive charges in the ZnO ETL, thereby contributing to enhanced device stability[97]. Additionally, a separate

study found that subjecting the ZnMgO NPs to moisture can greatly improve the B-QLEDs' efficiency and stability. The H_2O-passivated ZnMgO NPs benefit from passivated surface defects and altered electron injection properties versus the pristine ZnMgO NPs that lead to enhanced device performance[98].

2.4.2 Shelf Life

QDs are known to be degraded via various molecular interactions with oxygen and moisture. In addition to QD structure engineering to have bulky ligands that protect the QDs, it is imperative for QLEDs to be sealed from the ambient environment. Typically, QLEDs are encapsulated using a glass cover that is sealed to the device substrate using an ultraviolet (UV)-curable resin glue. This encapsulation process is recognized to have positive and negative effects on device efficiency over time which is unfavorable for the QLEDs shelf life. Positive aging is a phenomenon observed in QLEDs encapsulated using UV-curable resins. During positive aging, the efficiency of the QLEDs increases over time, while the devices are not subjected to any electrical bias, a behavior that saturates within two to seven days. In the long term, however, there's a reversal of this trend, and the devices experience a spontaneous gradual decline in efficiency, even in the absence of any electric bias. This phenomenon, commonly termed spontaneous negative aging, persists in encapsulated QLEDs. Despite significant research efforts, the underlying mechanism driving the spontaneous negative aging behavior remains elusive. Consequently, the shelf life of QLEDs, including state-of-the-art models, remains generally limited.

2.4.2.1 Positive Aging

Positive aging represents a remarkable and intriguing phenomenon in QLEDs, particularly in hybrid devices incorporating metal oxide ETL. Currently, various perspectives exist to explain the positive aging effect, all of which are linked to inorganic electron transport materials such as ZnO and ZnMgO. These materials are widely regarded as the actual drivers behind the positive aging phenomenon in QLEDs. Although there are reports investigating the root causes of positive aging, it is still not clear. Typically, these investigations have concentrated on elucidating the combined influence of encapsulation and ZnO ETL.

In 2017, Acharya et al. first reported the shelf aging phenomenon in red, green, and blue QLEDs, noting an increase in device efficiencies over time. The behavior was attributed to the interaction between the surface of the ZnO ETL and the weak acids present in the encapsulation resin. This

interaction led to the formation of zinc carbonate and a subsequent reduction in the defect densities of ZnO[99]. Also, Su et al. showcased that an interfacial reaction between ZnMgO and Al proceeds gradually over several days, culminating in the formation of AlO_x. This compound's presence is speculated to foster an enhancement in electron injection and prevent exciton quenching at the interface of ZnMgO with the Al cathode[100]. In another work, the efficiency improvements are ascribed to the hole leakage channel blockage via ZnMgO defects passivation. Similarly, it is proposed that the active-surface adsorption sites for oxygen in ZnO can be stabilized by the H^+ in acidic resin, leading to suppressed non-radiative recombination[101]. In another work, it is hypothesized that the organic acid leads to the diffusion of silver cathode into the oxide ETL, thereby increasing the conductivity of the ZnO layer[102]. In addition, previously our group showed that the significant efficiency enhancement is primarily due to the electron injection improvement at the QD/ZnMgO interface and not just due to the suppressed exciton quenching at that interface[103].

Despite extensive research into the shelf-aging mechanism of encapsulated QLEDs, a unified conclusion remains elusive. While the mechanism behind positive shelf aging remains a topic of debate, it is widely accepted that it is closely linked to the intrinsic properties of ZnO or ZnMgO. The divergence in the types of ZnO NPs and encapsulation methods employed by various research groups has resulted in inconsistent observations of shelf aging behaviors. These variations encompass differences in duration, extent of efficiency improvement, current enhancement, and other factors. As a result, the elucidation of the mechanism is still ongoing[29].

Although positive shelf aging has the potential to improve QLED performance, its unpredictable nature makes it undesirable for practical applications. Consequently, researchers have embarked on exploring various strategies to mitigate or eliminate the shelf aging phenomenon.

2.4.2.2 Negative Aging

In the long term, the QLEDs that have experienced positive aging behavior inevitably undergo a gradual decline in device performance, termed negative aging. Negative aging is known as efficiency drop and decreased current density in the J-V characteristics of the device with increased turn-on voltage. Studies suggest that the acrylic acid in the sealant induces chemical reactions which result in positive aging. The progression of these reactions inevitably leads to a deterioration in device performance in the long term. It is reported that the acid resin causes the silver cathode corrosion and converts the conductive ETL to metal carboxylate and water is a byproduct of this reaction that results

in the corrosion of silver cathode and conversion of oxide ETL to insulating metal carboxylate with accumulation of water leads to device degradation and negative aging[102]. Previously in our group, it was reported that the spontaneous negative aging in a long time primarily arises from the degradation of organic HTL which replacing it with a cross-linked polymer HTL significantly extends the shelf life of B-QLEDs[104].

The spontaneous negative aging in encapsulated QLEDs underscores the impracticality of relying on positive aging to enhance QLED performance for practical applications. Also, the insufficient shelf life of current state-of-the-art QLEDs necessitates urgent solutions.

2.5 Summary

Various research works regarding the QLEDs degradation mechanisms or approaches for improving the QLEDs EL stability are discussed. The literature review mainly focuses on the studies about QDs PLQY stability, CTLs' role in QLEDs degradation, or the mechanisms affecting the shelf life of the QLEDs.

Factors such as QD charging, or Joule heating can temporarily or permanently lead to QD PLQY degradation. Moreover, oxygen and moisture together with light can enhance the QDs PLQY via surface defect passivation, however, it results in QDs degradation in the long term. Improving charge balance in QLEDs, engineering the QDs core/shell structure, and designing suitable ligands have been shown to be essential for obtaining stable PLQY for QDs, particularly for B-QDs owning the most susceptibility to non-radiative recombination pathways. However, it is not clear whether B-QDs' PLQY stability is a contributing factor to the B-QLEDs' poor EL stability.

Moreover, various factors are introduced to be responsible for organic HTL degradation. Excessive electron leakage into the HTL, charge accumulation at the HTL/QD interface, or solvent damage are some of the reasons that lead to HTL damage. This highlights the significance of designing and employing appropriate HTL with high chemical stability, better energy levels matched with the QD EML for efficient hole injection, and better electron-blocking properties. Some of the HTL engineering methods such as doping to induce cross-linking, using cascaded HTLs to stepwise the hole injection barrier and eliminate charge accumulation, HIL plasma treatments, and synthesizing new HTLs discussed to be effective in enhancing QLEDs stability in various ways.

Although it is agreed to use ZnMgO as the ETL currently in state-of-the-art B-QLEDs, it seems that there are other unknown aspects of the ETL role in B-QLEDs stability to be identified. Some studies have revealed notable changes in QLED performance by modifying the ZnMgO ETL, for example, air exposure for defect passivation or encapsulation entangled with ZnMgO seems to have significant impacts on QLED performance. However, further investigations are necessary, particularly for B-QLEDs, to pinpoint the fundamental challenge(s) impeding the device EL stability, before pursuing incremental enhancements through detailed modifications.

To date, several research studies have tried to introduce the degradation mechanisms in QLEDs, and a few are focused on B-QLEDs. Although notable advancements have been achieved in enhancing R- and G-QLED EL stability through the proposed material and structural design improvement, the underlying degradation mechanisms are not yet fully understood for B-QLEDs, leaving their EL stability inferior to the other primary colors. To this end, further research is needed to obtain a comprehensive understanding of the degradation mechanisms to develop appropriate strategies to address them and achieve highly stable B-QLEDs.

Chapter 3

Research Methodology

This chapter describes the research methodology employed in this study, for fulfilling the research objectives defined earlier. Here, the methodology utilized in this study is thoroughly outlined, encompassing essential detailed aspects such as device layout, fabrication process, and device characterization. By presenting a thorough methodology in line with the objectives, this chapter ensures transparency, reliability, and validity of the research process, establishing a solid foundation for the subsequent findings.

3.1 Device Layout

Figure 3.1 presents a schematic overview of a fabricated device, showcasing the emissive and transport layers' coverage and the vertical overlap of the ITO and metal electrodes that establish the dimensions of the QLED. Each QLED investigated in this study was manufactured on a glass substrate measuring 50.8 mm × 50.8 mm, featuring 100 nm-thick pre-patterned ITO electrodes and a resistivity of 20 Ω sq^{-1}. A total of 14 ITO electrodes, each with a width of 2 mm, are positioned on two opposing sides of the substrate to delineate one dimension of the QLED area. As they approach the substrate's edge, the width of these 14 ITO pads widens to 4 mm to enhance contact with the test fixtures within the measurement systems. Adjacent to these sets of ITO electrodes are ITO pads, 7.4 mm in thickness, serving as the counter electrode. These are connected by a 100 nm thick layer of Al, defining the second dimension of the QLED. The intersection between the bottom ITO electrode and the Al top electrode yields QLEDs measuring 2 mm × 2 mm. Within this structure, the emissive and transport layers, each around 100 nm thick, are enclosed between the two electrodes. Notably, the rectangular feature within the ITO pad at the top right of the schematic serves as a marker for substrate orientation.

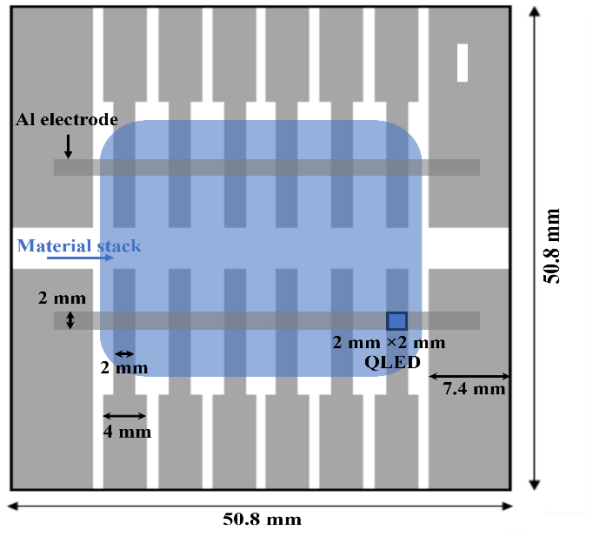

Figure 3.1 Schematic of the QLED substrate layout used in this work.

3.2 Fabrication Process

3.2.1 Upright QLED Fabrication

The patterned substrates with ITO were first cleaned by Micro90 and then sonicated in DI water, acetone, and isopropanol, respectively for 10 minutes each. The cleaned substrates were treated with oxygen plasma for 5 minutes. Then, poly(3,4-ethylenedioxythiophene)-poly(styrenesulfonate)(PEDOT:PSS) (Heraeus-Clevios PVP AI 4083, filtered through a 0.22 μm PTFE filter) was spin-coated at 5000 rpm for 60 s using a Laurell WS-400A-6NPP/LITE spin coater. The PEDOT: PSS films were annealed at 150 $^{\circ}C$ for 15 minutes in the air. The substrates were transferred to a nitrogen-filled glove box for the rest of the process. The poly[(9,9-dioctylfluorenyl-2,7-diyl)-alt-(4,4′-(N-(4-butylphenyl))-diphenylamine)] (TFB) HTL, dissolved in chlorobenzene (8 mg/ml) was spin-coated at 4000 rpm for 40 s and annealed at 120 $^{\circ}C$ for 20 minutes. Then B-QDs (CdZnSeS/ZnS, from Mesolight Inc.), suspended in octane (10 mg/ml) were spin coated at 3000 rpm for 40 s followed by 20 minutes of annealing at 100 $^{\circ}C$. The same spin coating and annealing recipe were used for ZnMgO NPs from Mesolight with 25 mg/ml concentration in ethanol as the ETL. Aluminum anode (Al, Angstrom Engineering) was then deposited using a thermal evaporator (Angstrom Engineering) at a rate of 2 Å s^{-1} and vacuum level of 5 × 10^{-6} Torr. The active size of the QLED is 4 mm^2. Finally, the

devices were encapsulated using UV-curable resin glue (from Mesolight Inc.) and cover glass, cured under 365 nm UV radiation for 20 minutes. For the devices using the VB-FNPD, the HTL(VB-FNPD) dissolved in chlorobenzene (10 mg/ml) was spin-coated at 3000 rpm for 40 s and annealed first at 100$^{\circ C}$ for 15 minutes and then at 220 $^{\circ C}$ for 60 minutes.

3.2.2 Upright QLED with Marking Layer

All the steps are followed as the typical upright QLED except that ZnMgO concentration is reduced from 25 mg/ml to 12.5 mg/ml to obtain thinner ETL. Next, the devices are moved to a thermal evaporation chamber to co-deposit TPBi host ETL and DCJTB red emitting organic fluorescent material at a rate of 0.2-2 Å s^{-1} in an Angstrom Engineering EvoVac thermal evaporation chamber at a base pressure of 5×10^{-6} Torr.

3.2.3 Sol-gel Synthesized ZnO.

The thin film sol-gel synthesized ZnO is used as an ETL. Sol-gel method is widely used chemical synthesis of metal oxide thin films. For ZnO synthesis, 197 mg zinc acetate with 54 µl of ethanolamine, as the surfactant, is diluted in 6 ml of ethanol. The solution is stirred for 40 minutes, and the solution is filtered using (Heraeus-Clevios PVP AI 4083, filtered through a 0.22 µm PTFE filter) two times, and spin-coated at 1000 rpm speed for 60 s in the atmosphere. The samples are then annealed at 150 $^{\circ C}$ for 30 minutes.

3.2.4 Encapsulation

After coating the Al cathode, the devices were encapsulated in a nitrogen-filled glove box. A cover glass (microscope slide) with the size of 1.5 cm × 0.8 cm was used to fully cover three device areas of each quarter made from the full substrate. Firstly, the cover glass was coated with UV-curable resin glue by syringe and flipped on the Al cathode aligned with the device areas of each quarter. After applying the cover glass on all four quarters, a UV-365 nm lamp was used to illuminate the samples for 20 minutes to solidify the resin sealant. Due to the positive aging phenomenon in encapsulated QLEDs that the device needed three days to achieve its peak EQE, all the fabricated devices for electrical tests (aging, characterization, etc.) were encapsulated and the experiments were started after the three days for symmetry. This excludes the samples for Chapter 4 where the shelf life of QLEDs and film morphologies were studied.

3.3 QLED Characterization

Comprehensive characterization of each device involved various analyses including current density-voltage-luminance (JVL) measurements, electroluminescence (EL) and photoluminescence (PL) spectral measurements, and EL stability measurements. Specialized techniques such as transient photoluminescence (TRPL) spectroscopy were employed to delve into specific device characteristics of the devices following the initial characterization measurements. Unless otherwise specified, all device tests were carried out in a test box under a N_2 gas atmosphere.

3.3.1 Current density-Voltage-Luminance Characteristics

J-V-L measurements entailed sweeping the QLED's driving voltage from 0 V to 10 V by an Agilent 4155C semiconductor parameter analyzer, capturing the current at each increment. The current density was determined by dividing the measured current by the QLED area (4 mm^2). Luminance was measured by a silicon photodiode linked to the semiconductor parameter analyzer, allowing each photocurrent value to be correlated to the voltage step. Subsequently, the photocurrent was calibrated to a luminance value established at a driving current of 20 mA/cm^2 by a Minolta Chroma Meter CS-100. The EQE of the QLEDs was calculated as outlined by Okamoto *et al*. assuming a Lambertian emission distribution[105].

3.3.2 Electrical Stability

Electrical lifetime measurements were carried out using a McScience M600 PLUS Lifetime Test System, typically under a constant current density of 20 mA/cm^2 bias application to the QLEDs while a silicon photodiode recorded the luminance of the devices throughout the testing duration. In the case of pulsed current aging, a pulsed current bias was used with a frequency of 50 Hz, 50% duty cycle, and an amplitude of 20 mA/cm^2. In order to compare these results with constant current aging, a constant current density of 10 mA/cm^2 driving was used to keep the average number of injected carriers constant. The actual luminance of the QLED over time was calibrated to the initial luminance measured by a Minolta Chroma Meter CS-100. The driving voltage of the QLED was also monitored as a function of testing time. To measure the LT50 of a device, the test was terminated when the luminance of the QLED had declined to 50% of its initial luminance value.

3.3.3 Electroluminescence Spectroscopy

The EL emission spectra of the QLEDs were captured using an Ocean Optics QE65000 spectrometer equipped with an optical fiber covering a range of 350-750 nm. The QLEDs were consistently driven with a constant current density of 20 mA/cm^2 unless otherwise specified. The light intensity measured by the spectrometer was normalized to the peak of interest, typically corresponding to the highest intensity peak. This normalization aided in comparing the various contributors to the EL spectrum effectively.

3.3.4 Photoluminescence Spectroscopy

The PL emission spectra of the QLEDs and other films were measured using an Ocean Optics QE65000 spectrometer equipped with an optical fiber spanning a range of 350-750 nm. PL was induced by illuminating the samples with a 200 W Hg-Xe lamp controlled with an Oriel 77200 monochromator to isolate specific peaks in the incident light emission spectrum. Generally, the Hg-Xe peaks near 330 nm and 365 nm were used in this work for the materials used herein. The measurements were conducted in nitrogen flow as an inert gas to minimize the effect of the atmosphere. The intensity of light measured by the spectrometer was then normalized to the peak of interest, generally corresponding to the highest intensity peak to facilitate comparison between the different contributors to the PL spectrum of the specimen.

3.3.5 Time-Resolved Transient Photoluminescence Spectroscopy

TRPL decay measurements were conducted using an Edinburgh Instruments FL920 spectrometer equipped with a 380 nm peak emission EPL375 picosecond pulsed laser diode. The laser diode optically excited the sample, and the emitted light from the sample at the target wavelength, resulting from exciton recombination, was recorded over time from the initial excitation. The TRPL characteristics of a material are correlated to its exciton lifetime. Therefore, this technique is valuable for understanding the exciton quenching processes in devices or energy transfer dynamics between two materials. These measurements were carried out under ambient conditions.

3.3.6 Capacitance-Voltage (C-V) Measurements

The capacitance-voltage measurement was conducted using Keithley's Model 4200-SCS Parameter Analyzer. The C-V characteristics of QLED were used to assess the charge distribution and annihilation in the device. For this measurement, the QLED comprising different CTLs or QD layers with electrodes

can be considered as parallel rectangular capacitances. For C-V characterization in sweeping mode, the voltage value swept a range from -1 V to above 5 V with specific steps, and meanwhile, the capacitance of the device was measured using a sinusoidal signal with an amplitude of 30 mV and frequency of 5 KHz. The charges typically are transported through the CTLs and get injected into the QD layer under bias. If at one interface, the energy barrier hinders the proper carrier injection and results in charge accumulation, the effective thickness of the capacitance decreases, and therefore, the capacitance value increases. On the other hand, when there is charge annihilation at some voltage, the carrier recombination leads to a smaller number of charges stored in the device, and its capacitance value drops.

In sampling mode, the targeted bias voltage of the device was set, and the capacitance value was measured as a function of time. This technique allows for observing charge distribution over time in a device under a desired operation bias voltage. Here again, a sinusoidal signal with an amplitude of 30 mV and a frequency of 5 KHz was used as the bias to capture the capacitance. The capacitance vs. time allows for investigating the charge annihilation and accumulation in the device over time during the operation.

3.3.7 Surface Morphology & Roughness

A Bruker FastScan/Icon atomic force microscope (AFM) was used to characterize the surface morphology and roughness of deposited films. There are two characteristics of interest in the evaluation of roughness: peak-to-valley or Z-range, and root-mean-square (R_{rms}) roughness. Z-range represents the difference between the maximum height and minimum valley in a given image whereas R_{rms} is the square root of the sum of squared film heights over the entire measured area. Both values are useful in the characterization of a film surface and R_{rms} can be taken to represent the global film roughness and is the roughness value generally reported on in literature. This measurement technique was carried out under ambient conditions.

3.3.8 Time-of-Flight Secondary Ion Mass Spectrometry (TOF-SIMS)

TOF-SIMS is a powerful technique employed for species composition analysis. It operates by utilizing pulsed ion beams to ablate material from the outermost surface layer, subsequently detecting the secondary ions released from the surface. As a result, TOF-SIMS provides insights into the distribution of chemical composition throughout the entire depth of the film. This technique requires conductive substrates to neutralize the bombarded ions and avoid sample charging. It can be carried out

in either positive or negative polarity done with Bi or Cs sputtering ions allowing for different species to be sputtered and detected.

Chapter 4

Investigating the Shelf Life of the B-QDs' PLQY as a Potential Factor Affecting the EL Stability

Some of the material in this chapter has been submitted as " Increased Quenching by ZnMgO Over Time and the Limitations for the Long-Term Stability of Quantum Dot Light-Emitting Devices ", The Journal of ACS Applied Nano Materials, under review.

The EL stability of B-QLEDs hinges primarily on B-QDs PLQY stability under two scenarios of storage over time and during the operation under electrical stress. In other words, the requirement to have stable B-QLEDs during their operation is that B-QDs should be able to maintain their PLQY during the storage time in an inert atmosphere and simultaneously under bias. Thus, to systematically investigate the underlying causes behind the poor EL stability of B-QLEDs, the stability of B-QDs PLQY over time in storage (shelf life) is studied separately from the stability of B-QD PLQY during device operation under electrical stress.

Having a long shelf life for B-QLEDs requires that the B-QDs in the device stack be able to photo luminance during the time that the devices are kept in storage without any bias application for a long period. In addition to the sole B-QDs PLQY long shelf life, other layers that are used in the device stack need to be stable in storage as they might affect the B-QDs PLQY if they are unstable. However, devices with long shelf life can undergo degradation under electrical stress due to factors induced by bias that can ultimately lead to B-QDs PLQY loss. Therefore, the stability of the B-QDs PLQY needs to be examined first without bias and then under bias to pinpoint the origin of the device's poor EL stability. This chapter mainly unveils the findings of investigating the B-QDs PLQY stability in the absence of electrical stress. It delves into the influence of adjacent CTLs, i.e. ETL and HTL, as well as the intrinsic

stability of B-QDs PLQY as a thin film. It sheds light on the impact of HTL and ETL on B-QDs PLQY, elucidating the underlying mechanisms at play.

4.1 Results and Discussion

4.1.1 B-QDs intrinsic PLQY stability

The first step is to identify if the B-QDs as a thin film have stable PLQY over time in the absence of electrical stress. To test the temporal stability of B-QDs PLQY, the B-QD film is coated on glass and its PL spectrum is monitored initially and after 24 hours of storage. The samples are stored in N_2 gas flow as an inert gas to avoid ambient effects.

Figure 4.1a shows the changes in the PL spectrum of the B-QDs film, collected at 330 nm excitation wavelength. The results show that B-QDs undergo a significant PLQY loss over 24 hours of storage. Although the storage condition is provided in the inert N_2 gas flow, one can assume that there might be impurities in the experiment condition of ambient oxygen and moisture that affected the B-QDs. As the B-QDs have a small size with a large surface area, in addition to their large exciton energy, they are vulnerable to quenching processes caused by oxidation.

In order to further verify the B-QDs PLQY loss over time, the B-QD films are covered with a 100 nm-thick Al to further avoid the ambient moieties. **Figure 4.1b** depicts the PL spectra of B-QDs initially and after 24 hours of storage in N_2 gas. The results show that the B-QDs PL spectrum is not changed over time if covered with Al. Thus, one can conclude that B-QD film has stable PLQY over time that can be considerably sensitive to the atmosphere. Given that B-QDs are sandwiched between CTLs in the device stack, one can assume that it is unlikely that B-QDs be affected by the atmosphere and consider that the PLQY of the B-QDs thin film inherently has a shelf life of more than 24 hours.

a) b)

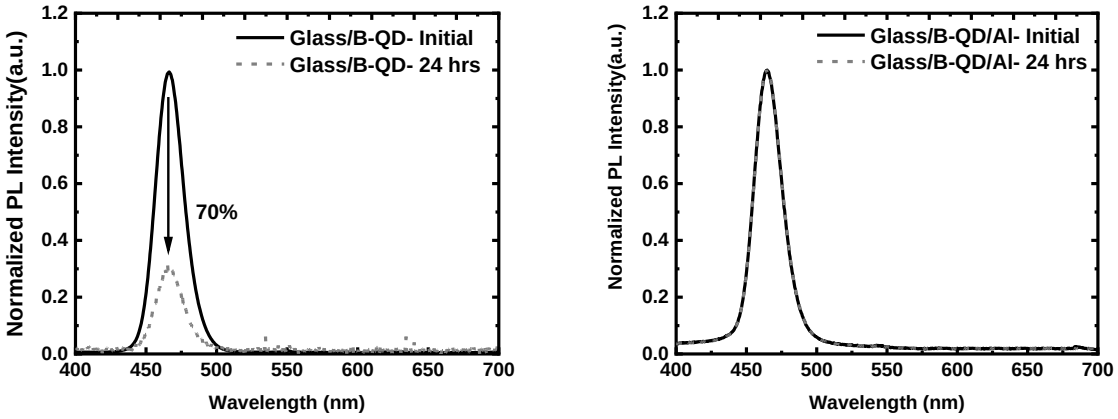

Figure 4.1 PL spectra of a) Glass/B-QDs b) Glass/B-QD/Al initially and after 24 hours of storage. The excitation wavelength is 330 nm

4.1.2 The Role of HTL on B-QDs PLQY Stability

Confirming that B-QDs PLQY is intrinsically stable in solid film over 24-hour period of time, the investigation is further pursued by testing the effect of adjacent layers that exist in the device stack on each side of B-QD film. Therefore, samples with the structure of Glass/ITO/ PEDOT:PSS(40 nm)/ TFB(20 nm)/ B-QD(20 nm)/Al(100 nm) are prepared to examine the influence of the hole supply part of the device (Anode/HIL/HTL) and the HTL/B-QD interface on the shelf life of the B-QDs PLQY.

Figure 4.2 demonstrates the PL spectrum of B-QDs initially and after 24 hours of storage in the inert N_2 gas flow, with the TFB PL spectrum in the inset. The spectra are collected under 330 nm excitation wavelength. The TFB spectrum encompasses two peaks at 436 nm and 465 nm which overlaps with B-QDs PL emission peak at 465 nm. The results show no change in the PL of the sample over time suggesting that HTL and HIL have minimal effect on the B-QDs PLQY in storage.

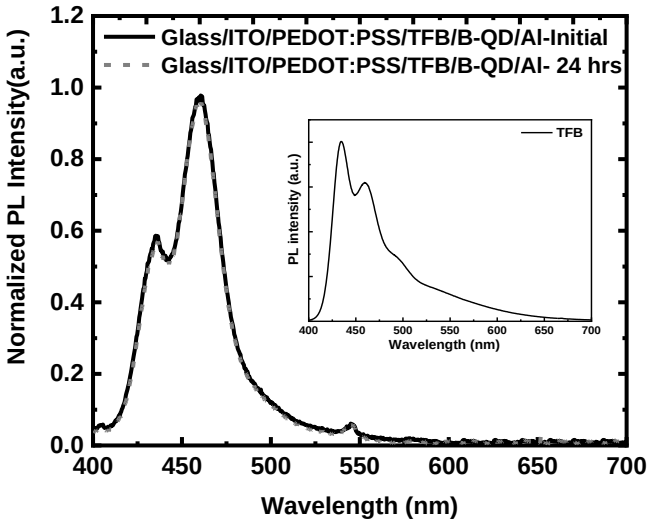

Figure 4.2 PL spectra of a) Glass/ITO/ PEDOT:PSS(40 nm)/ TFB(20 nm)/ B-QD(20 nm)/Al(100 nm) initially and after 24 hours of storage. The inset shows the PL spectrum of TFB film. The excitation wavelength is 330 nm.

4.1.3 The Role of ETL on B-QDs PLQY Stability

Subsequently, the B-QDs PLQY shelf life is assessed when in contact with the ETL. For this purpose, since ZnO and ZnMgO NPs are the two commonly used ETLs in QLEDs, they were chosen to study the role of ETL on B-QDs PLQY, and the results are compared. The samples have the structure of Glass/ B-QD (20 nm)/ ZnO or ZnMgO (60 nm)/Al (100 nm), similar to the case in upright B-QLED as shown in **Figure 4.3a**. Before checking the changes of B-QDs PLQY in the samples over time, the PL and TRPL characteristics of the samples are initially compared.

Figure 4.3b presents the TRPL decay characteristics at 465 nm collected under 380 nm excitation. The PL spectra of the samples, collected under 330 nm excitation, are shown in the inset. In this figure, the heights of the spectra are normalized in accordance with their relative intensities. As can be seen in **Figure 4.3b**, the exciton decay rate of B-QDs is faster when they are placed in contact with ZnMgO as compared to that in the case of ZnO. The PL spectra show a single peak at 465 nm, corresponding to the B-QDs PL emission. Comparing the B-QDs PL spectra in the two cases, one can see a lower intensity for the case when the B-QDs layer is in contact with ZnMgO as opposed to the ZnO. Thus, the results show that ZnMgO degrades the B-QDs PLQY more than ZnO in fresh samples.

To investigate how the O_2-vacancy defects in the ETLs contribute to the observed PLQY loss of B-QDs, as they could possibly lead to quenching via charge[75, 93], or energy transfer[106-109], we compare the PL spectra of the ETLs. **Figure S4.1** presents the PL spectra of ZnMgO and ZnO from fresh samples collected under 330 nm excitation. The results show that the broad emission band in the 450-700 nm, a range commonly ascribed to the O_2-vacancy defects[110-112], is less in the case of ZnMgO. This is despite the TRPL and PL results in **Figure 4.3b** showing that ZnMgO quenches the B-QDs PLQY more than ZnO. The results show that although ZnMgO has fewer O_2-vacancy defects than ZnO as expected, it still causes more quenching. Hence, one can conclude that O_2-vacancy defects cannot be the main factor behind the strong quenching effect of ZnMgO.

a) b)

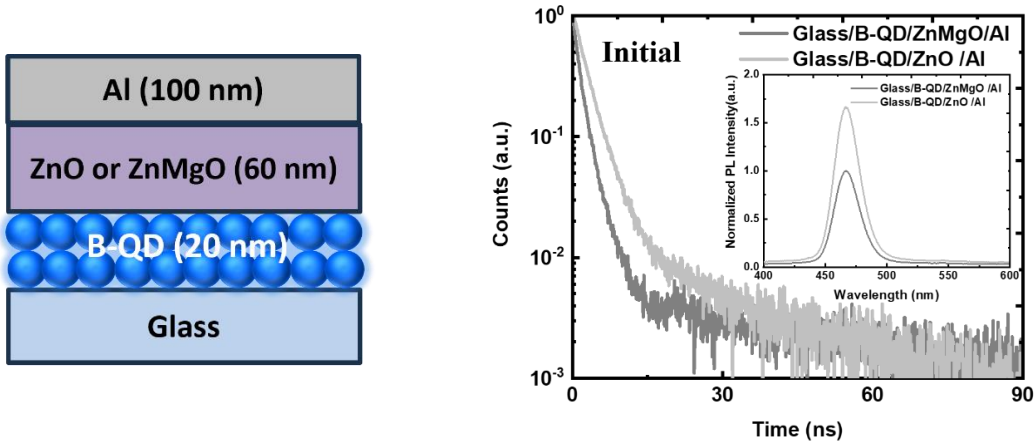

Figure 4.3 a) Schematic diagram of the samples with the B-QDs described in the text. b) TRPL decay characteristics of the B-QDs in contact with the ZnO or ZnMgO layer. The inset shows the corresponding PL spectra with normalized intensities. The excitation wavelength is 330 nm.

Moving back to the study of B-QDs PLQY shelf life, the possible changes in the B-QDs PLQY over time are studied in those samples. **Figures 4.4a** and **b** show the TRPL decay characteristics of B-QDs layers in contact with ZnMgO or ZnO layers, respectively, initially and after 24 hours of storage in nitrogen. The insets in the figures present the PL spectra of the same samples, again initially and after 24 hours, normalized to the peak initial height (at t=0). Interestingly, as can be seen from the TRPL

results, the quenching of the B-QDs increases over time in the case of ZnMgO resulting in a faster exciton decay rate, an effect that is not observed in the case of ZnO. The PL spectra also show a significant decrease in peak intensity in the case of the ZnMgO sample after 24 hours consistent with the increased quenching. They also show the emergence of broadband in the 500-600 nm range, overlapping with the emission from O_2-vacancies in the ETL shown in **Figure S4.1**[110-112]. In contrast, the PL spectra of the ZnO sample show no change over the same period of time. The increased quenching effect of the B-QDs by ZnMgO indicates that some phenomena, exclusive to the ZnMgO samples, must be taking place over time that progressively affect the B-QDs PLQY. These can include interfacial changes at the B-QDs/ZnMgO interface, morphological changes in the ZnMgO layer, or the diffusion of species from the ZnMgO layer into the B-QDs layer.

Previously in the literature, it was reported that encapsulation can mitigate the quenching effect of ZnO/ZnMgO on B-QDs PLQY, and the results are maintained over time[103]. However, as previously discussed in the literature review, encapsulation imposes changing behavior in the performance of QLEDs during different time stages that are not favorable for QLED commercialization. Moreover, there is no consensus on the mechanisms behind the encapsulation effects. As a result, it is recommended to obtain highly efficient and stable devices avoiding the encapsulation and therefore, there is still value in further exploring the possible mechanisms and causes behind the quenching effect of ZnMgO on B-QDs PLQY without encapsulation.

a) b)

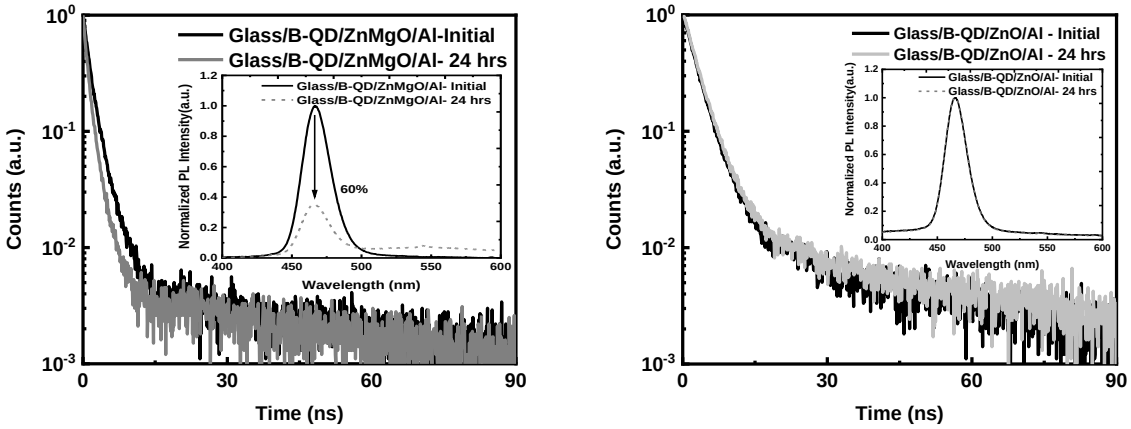

Figure 4.4 TRPL decay characteristics of the B-QDs in contact with a) the ZnMgO b) the ZnO layer initially and after 24 hours. All the insets show the corresponding PL spectra with normalized intensities.

4.1.4 ZnMgO Quenching Mechanisms on B-QDs PLQY

Before investigating the underlying reasons, it becomes important to first test if the quenching effect of the ZnMgO is limited to B-QDs or if it similarly affects narrower bandgap QDs, where the exciton binding energy is stronger and the rate of any energy transfer from the QDs to quenching sites will be expectedly lower [113]. We therefore conduct similar PL measurements on samples of the same structure but containing red QDs (R-QDs) instead. **Figure S4.2a** presents the TRPL decay characteristics of the fresh samples at 625 nm collected under 380 nm excitation, again with the PL spectra shown in the inset. As can be seen from the figure, here again, the ZnMgO leads to stronger quenching of the R-QD than ZnO, the same as in the case of B-QDs samples. In addition, the PL spectra and TRPL decay characteristics change over time for R-QDs in contact with ZnMgO or ZnO layers are presented in **Figures S4.2b** and **c,** respectively. Again, the ZnMgO quenching increases over time in contrast to ZnO, similar to the previous observations in the case of the B-QDs samples.

To explore the reasons behind the increasing B-QDs PLQY loss when in contact with ZnMgO versus ZnO, the surface roughness and morphological stability of the two ETLs as well as the B-QDs as single-layer films or bilayer stacks coated on glass substrates are studied using AFM measurements. **Figure**

4.5 presents the 3D AFM images collected from a representative 20 µm × 20 µm area from each sample immediately after fabrication (Initial) and 24 hours later. **Table 4.1** shows the surface roughness rms value and z-range for each case. Looking at the fresh samples first (left column), one can see that both ZnMgO and ZnO have very similar surface topography and rms values, but with the ZnMgO having a wider z-range (10.7 vs 6.0nm). In contrast, the QD film topography shows a coarser texture with larger spikes and valleys and a comparatively wider z-range than either ETL film. This coarser texture remains visible even after coating the B-QDs with the ZnO or ZnMgO, but the ZnO seems better at leveling it out, reducing the number of spikes that remain visible per unit area as well as the z-range. This may perhaps be due to the larger size of the ZnO vs ZnMgO NPs (~ 10 nm, and 5nm, respectively) hence their lower ability to fill in the smaller grooves of the B-QD film surface, limiting their ability to conform to the B-QD layer surface features. From this standpoint, the smaller size of the ZnMgO NPs and therefore their ability to conform better and to have more contact points with the B-QDs at the interface may perhaps be playing a role in the stronger initial quenching effect of the QDs by ZnMgO versus ZnO.

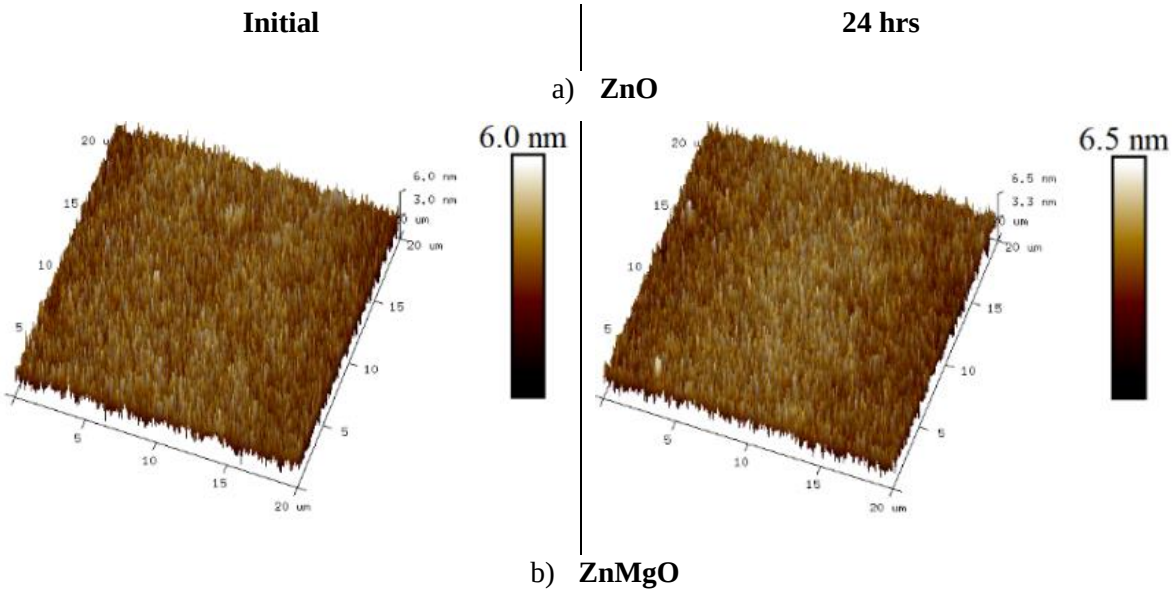

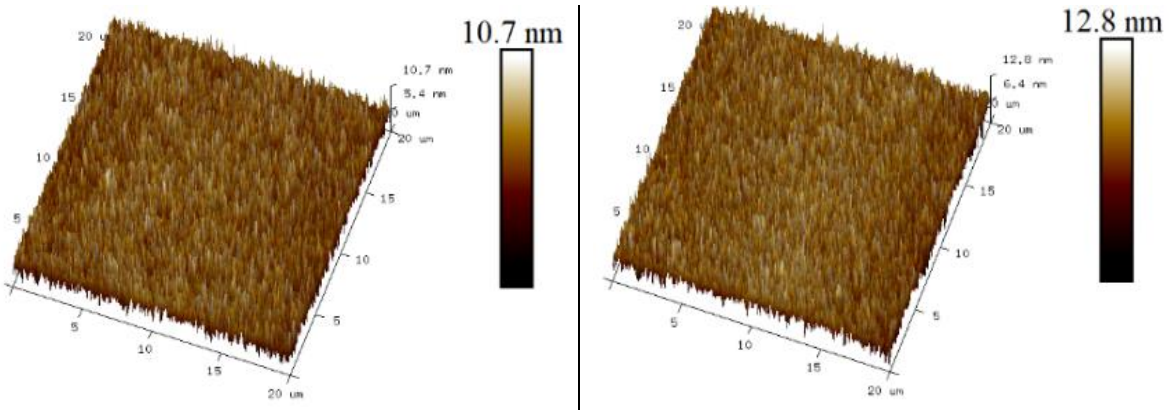

c) **B-QD**

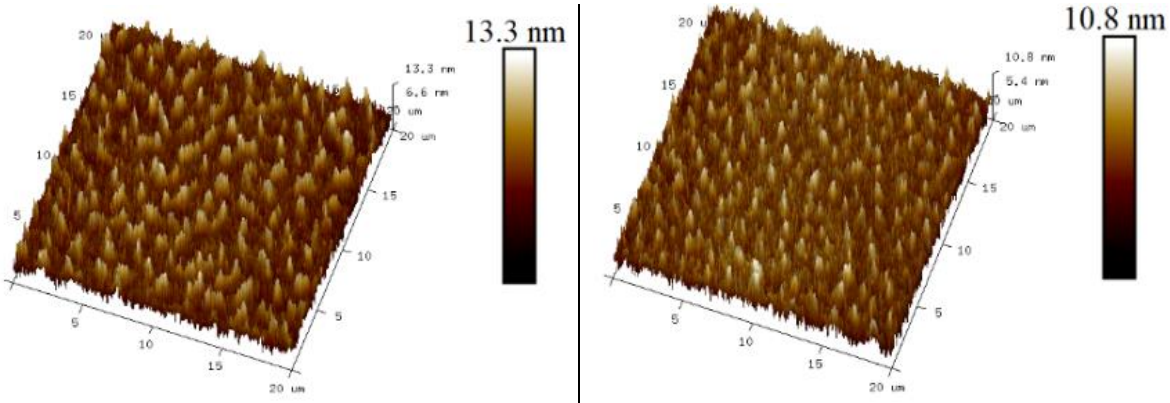

d) **B-QD/ZnMgO**

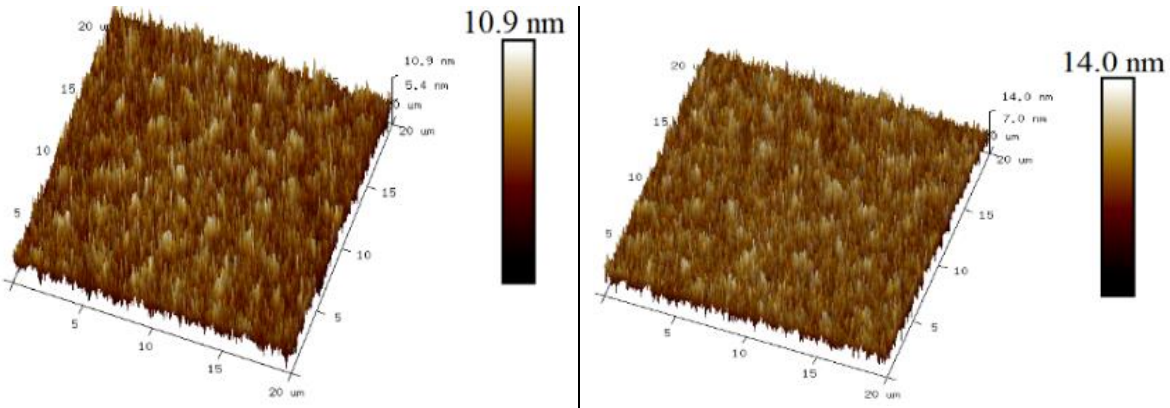

e) **B-QD/ZnO**

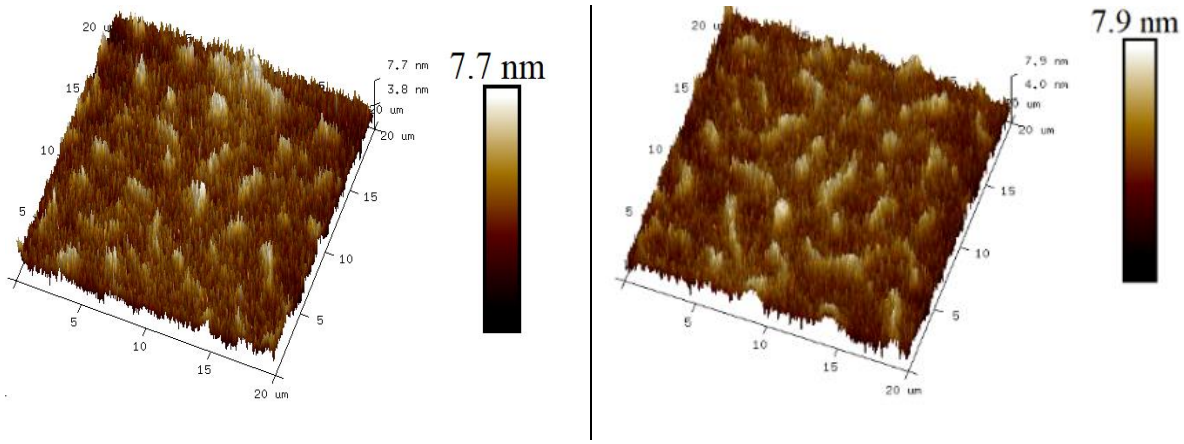

Figure 4.5 The AFM surface topography of a) ZnO b) ZnMgO c) B-QD d) B-QD/ZnMgO e) B-QD/ZnO films, all coated on glass, initially and after 24 hrs of storage.

Table 4.1 Roughness (rms) and z-range values of the AFM images in Figures 2 and 3 for the samples initially and after 24 hours of storage.

Time	ZnO		ZnMgO		B-QD		B-QD/ZnMgO		B-QD/ZnO	
	R_{rms} (nm)	z-range (nm)	R_{rms} (nm)	z-range (nm)	R_{rms} (nm)	z-range (nm)	R_{rms} (nm)	z-range (nm)	R_{rms} (nm)	z-range (nm)
Initial	1.1	6.0	2.18	10.7	2.2	13.3	2.28	10.9	1.19	7.7
24 h	1.17	6.5	2.71	12.8	2.06	10.8	2.72	14	1.16	7.9

Looking at the results from the samples after the 24 hours, one can see that although there are no significant changes in general, there is a non-negligible increase in the z-range values in the case of the ZnMgO and QD/ZnMgO (**Figures 4.5b**, and **d**) samples suggesting that ZnMgO undergoes some morphological changes when compared to ZnO (**Figures 4.5a,** and **e**). These changes are perhaps more clearly visible in optical microscopy images taken from the same samples (**Figure S4.3**) that show an increase in the feature sizes over the 24-hour period in the case of the B-QD/ZnMgO. Seeing these changes in the case of the B-QD/ZnMgO but not in the B-QD/ZnO sample suggests that morphological changes in ZnMgO, possibly leading to more defect sites, cannot be ruled out from playing a possible role in the progressive quenching behavior. This may perhaps explain why the progressive quenching

behavior is similarly observed in both B-QD and R-QD samples; since in both cases, it is driven by morphological changes that occur in the ZnMgO layer.

The QDs single film however shows a decrease in z-range over time suggesting the film becomes smoother possibly due to a spontaneous gradual mass transfer. Such mass transfer can occur in uncovered films by thermodynamical driving forces to lower Gibb's free energy.

In order to test if morphological changes in ZnMgO over time may indeed be behind, or at least be contributing, to the progressive quenching behavior, fluorescence images from B-QD/ZnMgO/Al, B-QD/ZnO/Al, and B-QD/Al stacks, all coated on glass substrates, are collected from them immediately after fabrication (Initial) and again after 24 hours. **Figure 4.6** presents the images. As can be seen, while the images show uniform fluorescence from all samples initially, the fluorescence becomes non-uniform after 24 hours in the case of the ZnMgO sample, exhibiting some features or texture. These features, essentially areas of different fluorescence intensity, point to variations in quenching, indicating that the features must be affecting the luminescence output of the B-QDs. Clearly, no such features or non-uniformities can be seen in the other two samples after the same 24 hours, indicating that the features are associated with ZnMgO. These results, therefore, prove that in comparison to QD/ZnO/Al, QD/ZnMgO/Al samples are less stable morphologically and that the morphological changes that occur over time can affect the PLQY of the B-QDs.

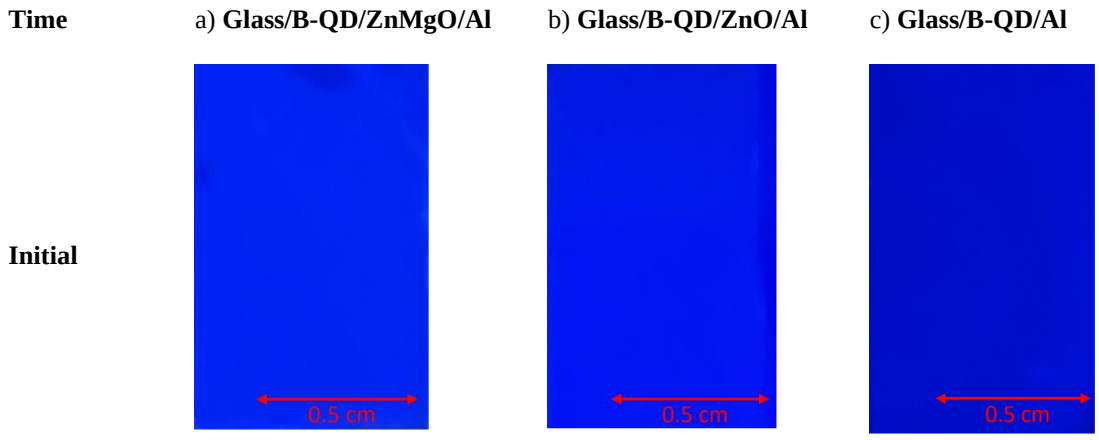

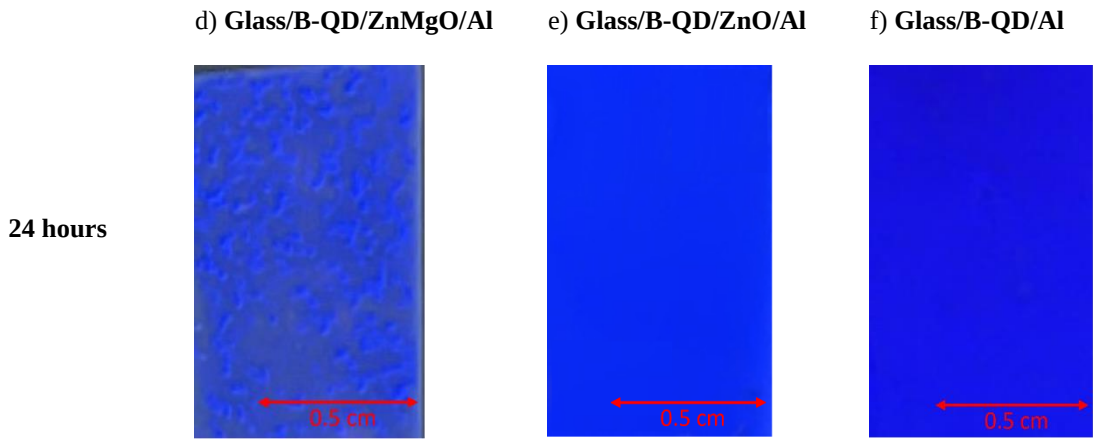

Figure 4.6 The PL images of the samples under 365-nm UV illumination initially and after 24 hours of storage.

In order to further investigate the phenomena behind the progressive quenching behavior, we fabricate and similarly test samples in which a ZnO layer, 30 nm thick, is interposed in between the QDs and ZnMgO layers. **Figure 4.7a** presents a schematic diagram of the sample. **Figure 4.7b** shows the TRPL characteristics and PL spectra collected (in the inset) from this sample as well as from the samples without the spacer for comparison, immediately after fabrication (initial). The TRPL decay characteristics demonstrate that the sample with the ZnO spacer layer has an exciton decay rate that lies in between those of the QD/ZnMgO/Al and QD/ZnO/Al. The PL spectra are normalized to the QD/ZnMgO/Al sample as the reference. Similarly, the PL spectra show that the height of the peak for the sample with the ZnO spacer layer lies in between those of the QD/ZnMgO/Al and QD/ZnO/Al, i.e., the fastest exciton decay rate for the sample with the lowest PL intensity. Therefore, the results suggest that the introduction of the ZnO spacer layer reduces the ZnMgO quenching effect in fresh samples.

Figure 4.7c shows the TRPL characteristics of the samples with the ZnO spacer initially and after 24 hours. The inset shows the PL spectra. The 24-hour characteristics of the sample without the spacer are also included for comparison. As previously presented in **Figure 4.7b**, the presence of the spacer causes the exciton decay rate to be somewhat slower than that of the ZnMgO-only reference sample (but still faster than the ZnO-only reference sample) initially. However, the exciton decay rate of the sample with ZnO spacer increases after 24 hours becoming almost equal to the ZnMgO-only reference as shown in **Figure 4.7c**. These results point to the out-diffusion of some species from the ZnMgO towards the QDs layer as another likely factor in the progressive quenching behavior. In this regard, the presence of the ZnO spacer slows down the arrival of diffused species to the QD layer delaying the

quenching effect. From this standpoint, the sample with a spacer has a faster exciton decay rate relative to the ZnO-only reference sample. This may be due to some initial diffusion of the same species from the ZnMgO into the ZnO and QD layer that occurs during sample fabrication causing some partial quenching even in the fresh sample. As this diffusion continues, the concentration of those species in the QD layer increases over time and eventually reaches those in the ZnMgO-only reference sample.

a)

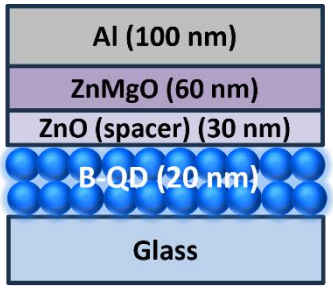

b)

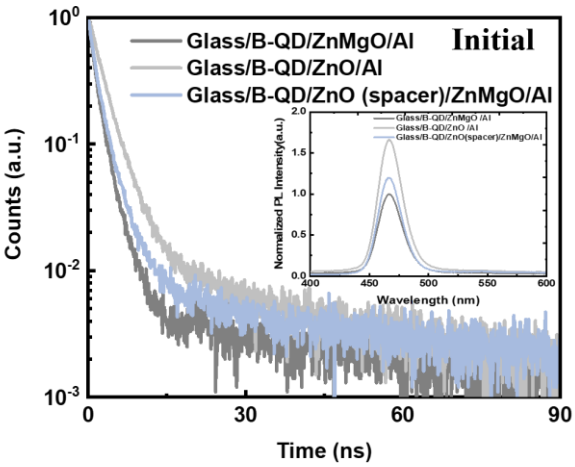

c)

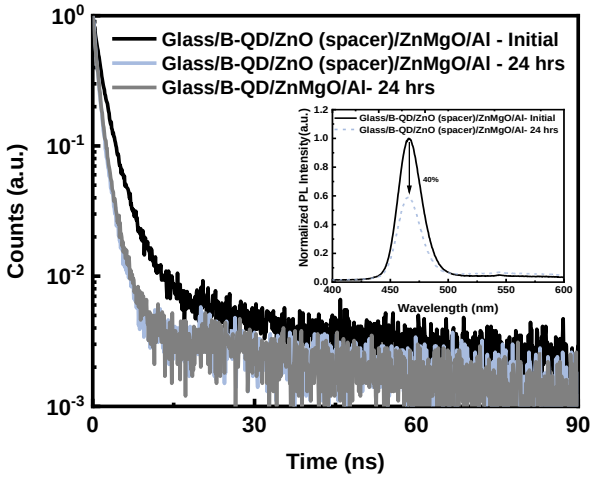

Figure 4.7 a) Schematic diagram of the sample with ZnO spacer layer. b) TRPL decay characteristics of the B-QDs in contact with ZnO, ZnMgO, and ZnO(spacer)/ZnMgO layers. The inset shows the corresponding PL spectra with intensities normalized to the Glass/B-QD/ZnMgO/Al sample. c) TRPL decay characteristics of the Glass/B-QDs/ZnO(spacer)/ZnMgO/Al initially and after 24 hours compared to that of Glass/B-QDs/ZnMgO/Al after 24 hours.The inset shows the PL spectra for the sample with the ZnO spacer layer initially and after 24 hours.

To further investigate the diffusion scenario possibilities, we test the effect of peeling off the Al layer from the samples after 24 hours using scotch tape. The TRPL characteristics of B-QD/Al, B-QD/ZnO/Al, and B-QD/ZnMgO/Al samples collected immediately before and after the Al is peeled off are presented in **Figure S4.4 a-c**, respectively. As can be seen in **Figure S4.4a**, in the case of B-QD/Al, the TRPL decay rate becomes slower after the Al removal, becoming similar to that of the uncoated (i.e. never coated) B-QD-only reference as the metal-induced quenching is eliminated[114]. Also in **Figure S4.4b**, the TRPL decay rate becomes slower after removing the Al in the B-QD/ZnO/Al sample that approaches that of the B-QD-only sample. The TRPL decay rate after Al peel-off becomes slower than that in the cases of B-QD/ZnO and B-QD/ZnO/Al. Therefore, the results indicate that the ZnO in this sample is removed together with Al. However, in the case of B-QD/ZnMgO/Al in **Figure S4.4c**, the TRPL decay rate is not changed after the Al is peeled off. The results suggest that either ZnMgO cannot be removed with Al or that ZnMgO leaves some residual quenching species that have penetrated into the QD layer bulk or remain adsorbed on the surface and that continues to affect the TRPL decay

rate even after the other layers are removed. From the perspective of the TRPL results from the ZnO spacer samples presented earlier, the observations here give further credence to the notion that the out-diffusion of some quenching species from ZnMgO into the QDs is behind the progressive quenching behavior observed in samples containing ZnMgO.

To delve deeper into and verify the diffusion hypothesis, we carry out TOF-SIMS measurements in order to test for any differences in concentrations of the elements present in the materials used in these samples and their relative distributions across the film thickness [115]. To this end, TOF-SIMS depth profiling measurements are conducted on ITO(100 nm)/B-QD(30 nm)/ZnMgO(60 nm)/Al(100 nm) and ITO(100 nm)/ZnMgO(60 nm)/Al(100 nm), the latter to be used as reference for the purpose of calibrating the sputtering time needed to reach the QD/ETL interfaces in the first sample. The samples are tested 24 hours after fabrication. **Figures 4.8a-d** show the TOF-SIMS elemental analysis data collected for negative and positive ions cases as a function of the sputtering time**.** A similar set of samples with ZnO is measured for comparison in **Figure S4.5**. Indium species are used as a probe for determining when the substrate has been reached.

a)

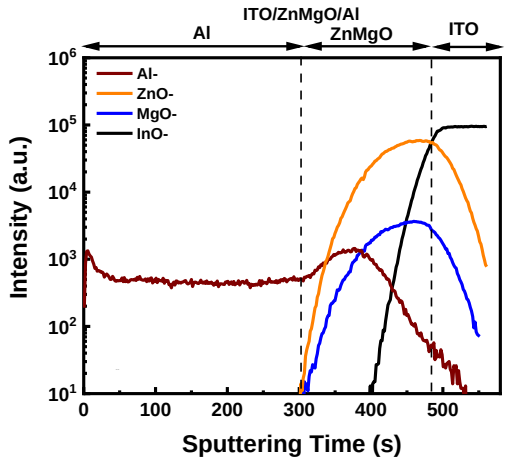

b)

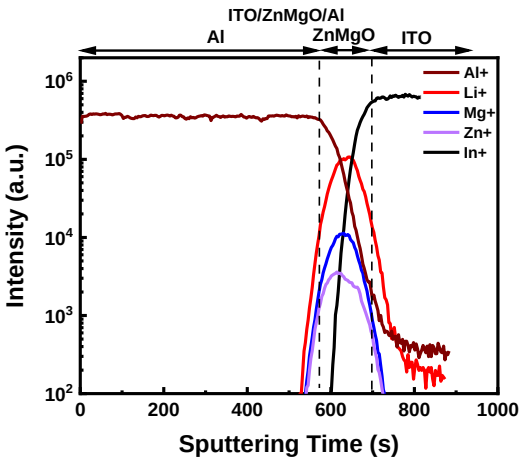

c)

d)

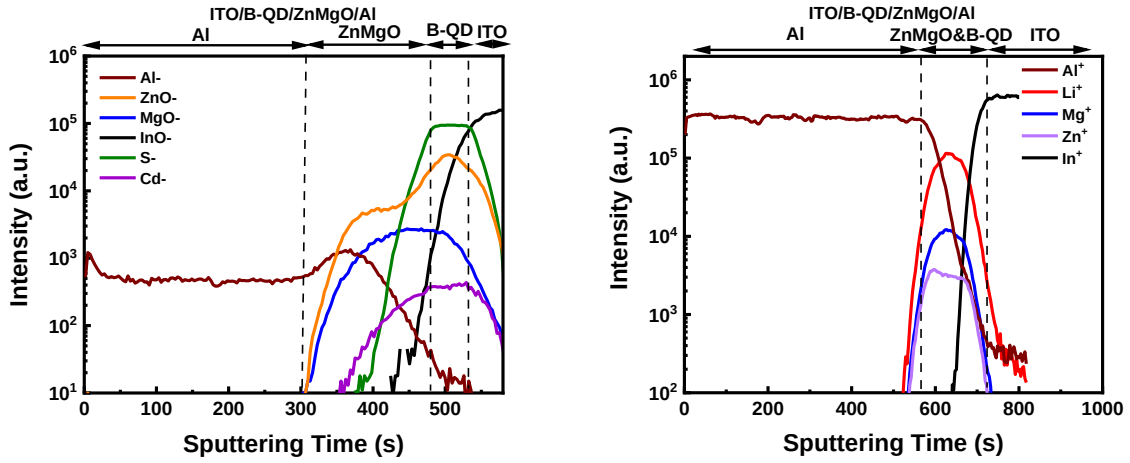

Figure 4.8 The TOF-SIMS depth profiles of a) ITO/ZnMgO/Al (Negative polarity) b) ITO/ZnMgO/Al (Positive polarity) c) ITO/B-QD/ZnMgO/Al (Negative polarity) d) ITO/B-QD/ZnMgO/Al (Positive polarity).

Figures 4.8a and **c** show the TOF-SIMs results from the samples without and with the B-QDs, respectively for the negative ions case. As shown in **Figure 4.8a**, sputtering through the Al takes about 300 s, which is when the ZnO^- and MgO^- species start to be detected, indicating that the ZnMgO layer has been reached. Thus, one can assume that after 300 s, the ZnMgO layer starts to be sputtered and that this process continues until 480 s, when the concentration of InO^- saturates; pointing to the ITO substrate being reached. Looking now at the data from the sample with the B-QD layer (in **Figure 4.8c**), Cd^-, S^-, and ZnO^- profiles (from the CdSe/ZnS B-QDs) start saturating at 480 s, the sputter depth that corresponds to the end of the ZnMgO as established earlier. The Cd^-, S^-, and ZnO^- species remain saturated until 530 s when the InO^- concentration stabilizes, indicating that the 480-530 s range corresponds to the B-QD layer. A comparison of the data in **Figure 4.8c** versus **a** shows that the MgO^- spectrum extends from the 480 s to 530 s (versus only 300 s to 480 s in **Figure 4.8a**) that is past the ETL and into the QD layer suggesting that the diffusion of MgO^- species from the ETL into the QD layer may indeed be happening. Looking at **Figures S4.5 a** and **c** verify that S^- and Cd^- species saturation onset identifies the transition from ETL to the B-QDs layer. In these samples, for example, the S^- and Cd^- species start to saturate at 400 s and remain saturated up to 450 s when the InO^- saturates and the substrate is reached. Moreover, no Mg species are detected in these samples, expectedly.

Figures 4.8b and **d** show data collected from the samples containing ZnMgO for the positive ions case. As can be seen in **Figure 4.8b**, it takes 580 s for Al to be sputtered and thereafter Mg^+ and Zn^+ ions from the ZnMgO layer become detectable and continue until 690 s when the In^+ saturates. However, in **Figure 4.8d**, it takes until 720 s to sputter through the ZnMgO and B-QDs layers and reach In^+ saturation. The Mg^+ and Zn^+ ions have continuous profiles in samples with and without B-QDs which makes it difficult to distinguish the ZnMgO from the B-QD layer. One can also see the presence of Li^+ over the same range where Mg^+ is present. The Zn^+ ions originate from either the ZnMgO oxide itself and/or from the shell part of the QD layer (CdSe/ZnS). Whereas, Li^+ and Mg^+ species are exclusively originating from ZnMgO, and observed all across the entire ZnMgO and B-QD layers, continuously. The Mg^+ species can be readily attributed to the doping component of ZnMgO and its presence past the ZnMgO layer and into the B-QD layer is consistent with the MgO^- results in **Figure 4.8c**. Although the source of the Li^+ may not be clear at first glance, LiOH is a commonly used precursor in ZnMgO NPs synthesis [116-117] and therefore the detected Li^+ can be due to residuals from it in the ZnMgO layer. Again, in **Figure S4.5 b** and **d,** none of the Mg or Li species are detected in ZnO samples verifying that the observations are exclusively originating from ZnMgO. Thus, the results show that Mg and Li from the ZnMgO can diffuse into the B-QDs possibly due to concentration gradient. Therefore, one can speculate that the out-diffusion of Li or Mg might also be a contributing factor in the QDs PLQY degradation in contact with ZnMgO over time acting as some exciton quenching pathways.

Considering the TRPL and PL results from the samples with ZnO spacer layer over time which are discussed earlier, the diffusion of species from the ZnMgO into the QD layer can also be another factor to the progressive quenching effect of ZnMgO in addition to the ZnMgO morphological changes observed earlier.

4.2 Conclusions

The research in this chapter shows that B-QDs can intrinsically have stable PLQY over time as a thin film when protected from ambient moisture and oxygen. Moreover, the results indicate that HTL and HIL are not detrimental to the shelf life of B-QDs PLQY. However, the results verify that ZnMgO reduces the QDs PLQY instantly and progressively over time. Surprisingly, the ZnMgO instant quenching effect is stronger than ZnO and the gradual QDs' PLQY loss is exclusively observed for ZnMgO cases. The AFM results show larger z-range values and changes for ZnMgO samples as

opposed to ZnO that can contribute to the faster QDs TRPL decay rates with ZnMgO than ZnO, instantly and over time. In addition, the TOF-SIMS measurements prove that Mg or Li can diffuse from ZnMgO into the QDs layer and can likely be involved in the QDs PLQY degradation by ZnMgO. The results highlight the limitations of ZnMgO for the shelf life of B-QLEDs where using ZnMgO is unavoidable due to better energy level matching for efficient electron injection into wide bandgap B-QDs. However, according to the literature, encapsulating the devices using UV-curable resin might help suppress the ZnMgO quenching effect on B-QDs although it may not be an optimized solution as it may introduce other issues in the long term. Thus, moving forward, all the devices in this work are encapsulated to minimize the B-QDs PLQY drop induced by ZnMgO or for symmetry.

Chapter 5

Investigating the Role of Electrical Stress on the B-QDs' PLQY as a Potential Factor Affecting the EL Stability

Some of the material in this chapter is reprinted with permission from " Stability Improvement in Quantum-Dot Light-Emitting Devices via a New Robust Hole Transport Layer ", J. Phys. Chem. C 2022, 126, 42, 18144–18151. Copyright 2024, American Chemical Society.

In addition to the shelf life of the B-QDs PLQY, it is necessary for the B-QDs to maintain the high initial PLQY during the B-QLEDs operation under electrical stress. The QLEDs operation involves positive (holes) and negative (electrons) charges to be injected from the electrodes and travers through the CTLs and recombine radiatively in the QD layer. Therefore, electrons and holes are crucial factors that potentially can affect the QDs PLQY directly or by initiating degradation in certain layers in the device stack that ultimately results in the QDs PLQY loss.

Given that the primary objective of this study is to discern the underlying causes behind the poor B-EL stability of B-QLEDs, it is beneficial to investigate the B-QDs PLQY stability under electrical stress. To systematically identify the potential impacts of electrons and holes— the two primary factors present during device operation—the PLQY of B-QDs is examined in single-carrier devices. Building upon the insights gained from the preceding chapter, the ZnMgO ETL exerts a quenching effect on B-QDs PLQY. Also, there are reports on the positive aging effect of encapsulation on defect passivation on ZnO/ZnMgO or QDs. Consequently, moving forward, the devices are encapsulated to possibly mitigate the ZnMO quenching effect, and simultaneously the shelf life of the devices is monitored. Thus, encapsulated hole-only devices (HODs) and electron-only devices (EODs) are fabricated. These devices consist of B-QDs sandwiched between two ETLs in EODs or two HTLs in HODs, and the devices' PL spectra are monitored after the devices are subjected to electrical stress.

This chapter mainly focuses on investigating the stability of B-QDs PLQY under electrical stress through single-carrier devices. In addition, the exploration is further pursued by proposing a solution to address the identified issues—replacing the problematic charge transport layer (CTL) to enhance the EL stability of B-QLEDs. The proposed solution is further tested on G-QLEDs, and the results are presented.

5.1 Results and Discussion

Electrons and holes are two of the primary species present in B-QLEDs operation that can drive device degradation during electrical stress. Therefore, it is critical to explore how these factors can affect the device's stability. So, to decouple these factors' impact, EODs and HODs are fabricated, and the PL spectra of the devices are measured before and after the electrical aging.

5.1.1 The Effect of Bias on B-QDs PLQY Stability in EODs

The encapsulated EODs are fabricated with the structure of Glass/ITO/ ZnO(sol-gel)(60 nm)/ B-QD(20 nm)/ZnMgO(60 nm)/Al(100 nm), and the device is aged under a constant current density of 20 mA/cm^2 under forward bias, i.e., when ITO is at a more positive potential relative to Al contact for 24 hours. Since the device is a single carrier device, the current dominantly corresponds to electron current flow. So, it allows for investigating whether electrons can affect the B-QDs PLQY. Thus, the PL spectra of the device are measured initially and after 24 hours of bias application, and the results are shown in **Figure 5.1a**. There is also a reference device in storage to have a record of temporal changes without any bias, as shown in **Figure 5.1b**. The spectra show a peak at 465 nm which corresponds to the B-QDs emission peak. The results show that the B-QDs peak intensity is increased in both cases with a larger change in the reference device. Provided that the devices are encapsulated, it can be due to positive aging after encapsulation which in literature is attributed to the result of defect passivation process in ZnMgO or B-QDs conducted by encapsulant(resin), so that the trap states which can quench the excitons are disappeared[103]. More importantly, the results show that the 24 hours of continuous electron current flow have minimal effect on the B-QDs PLQY. Therefore, B-QDs and ZnMgO are stable under electron current, and electrons cannot be the detrimental factor to B-QLEDs EL stability.

a) b)

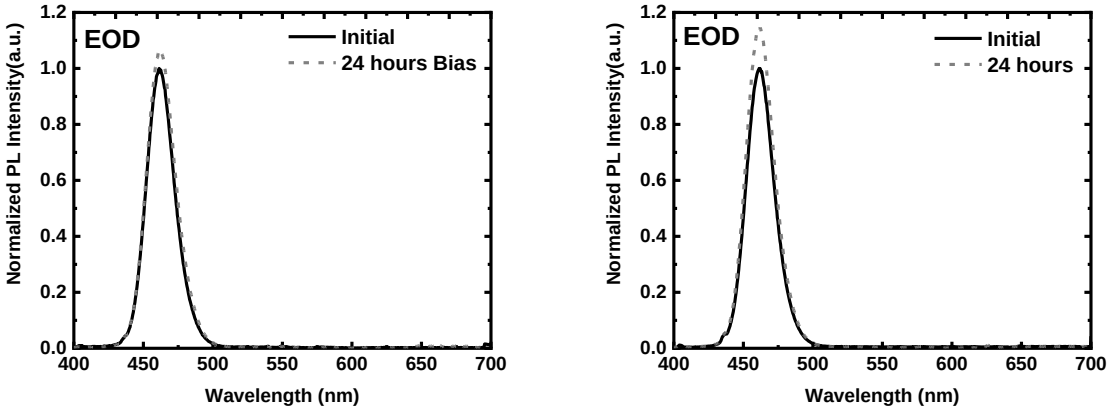

Figure 5.1 PL spectra of Glass/ITO/ ZnO(sol-gel)(60 nm)/ B-QD(20 nm)/ZnMgO(60 nm)/Al(100 nm) a) initially and after 24 hours of bias with a current density of 20 mA/cm^2 b) initially and after 24 hours of storage. The excitation wavelength is 330 nm.

5.1.2 The Effect of Bias on B-QDs PLQY Stability in HODs (TFB)

The study is continued by testing the B-QDs PLQY in HODs. To investigate the role of holes in B-QDs PLQY degradation, the encapsulated HODs with the structure of Glass/ITO/PEDOT:PSS(40 nm)/TFB(20 nm)/B-QD(20 nm)/CBP(20 nm)/MoO_3(5 nm)/Al(100 nm) are fabricated, and the device is aged under a constant current density of 20 mA/cm^2 under forward bias, i.e., when ITO is at a more positive potential relative to Al contact for 24 hours. The PEDOT:PSS hole injection layer (HIL) and TFB HTL are used in the upright B-QLEDs, MoO_3 is HIL that prevents electron injection to assure that the current of the device is dominantly hole current flow. Since MoO_3 is a metal oxide that can cause PL quenching, a 20-nm thick CBP HTL is used as a separator to avoid the undesired effect of MoO_3 PL quenching[118]. The PL spectra of the device are measured initially and after 24 hours of bias application, and the results are shown in **Figure 5.2a**. There is also a reference device in storage to have a record of temporal changes without any bias, as shown in **Figure 5.2b**. The inset in the figures shows the PL spectrum of TFB as a single film and all the spectra are collected using 330 nm excitation wavelength.

a) b)

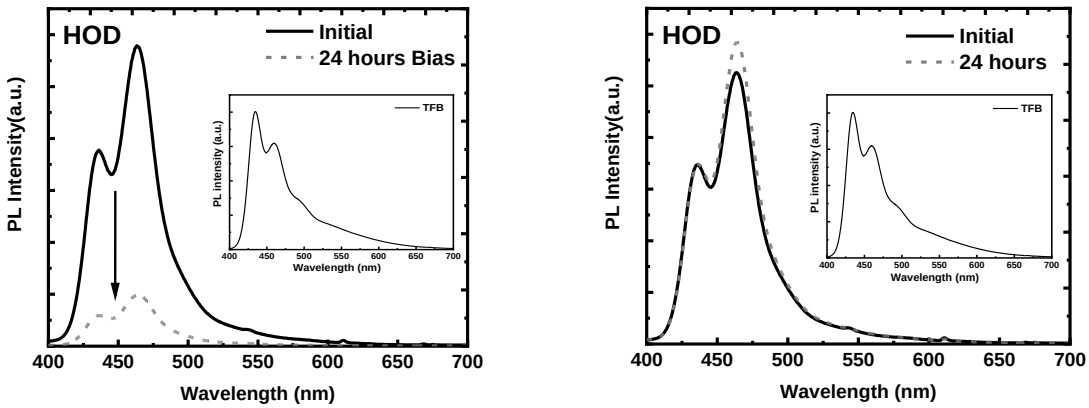

Figure 5.2 PL spectra of encapsulated HODs with the structure of Glass/ITO/PEDOT:PSS(40 nm)/TFB(20 nm)/B-QD(20 nm)/CBP(20 nm)/MoO_3(5 nm)/Al(100 nm) a) initially and after 24 hours of bias with a current density of 20 mA/cm^2 b) initially and after 24 hours of storage. The insets show the TFB film PL spectrum. The excitation wavelength is 330 nm.

The PL spectrum of TFB includes two peaks at 436 nm and 465 nm which the former coincides with the B-QDs PL emission peak. Therefore, the 436 nm peak can identify TFB and the latter B-QDs. As can be seen in **Figure 5.2a**, the HOD undergoes a significant PL loss in TFB and B-QDs emission bands during the aging under bias. On the other hand, looking at **Figure 5.2b**, not only the B-QDs PLQY is not decreased over time in storage, but also it is partially increased due to the enhancement induced by encapsulation[103]. Therefore, the results show that electrical stress negatively affects both B-QDs and TFB. It is possible that both or one of the layers undergo degradation due to hole current flow, and consequently affect both of the materials' PL emissions. Thus, holes can play a role in B-QLEDs electrical stability. To pinpoint the origin of degradation induced by holes, TFB is replaced with another polymer HTL in HOD, and the experiment is repeated.

5.1.3 The Effect of Bias on B-QDs PLQY Stability in HODs (VB-FNPD)

The encapsulated HODs with the structure of Glass/ITO/PEDOT:PSS(40 nm)/VB-FNPD(20 nm)/B-QD(20 nm)/CBP(20 nm)/MoO_3(5 nm)/Al(100 nm) are fabricated. In these devices, 9,9-Bis[4-[(4-ethenylphenyl)methoxy]phenyl]-N2, N7-di-1-naphthalenyl-N2,N7-diphenyl-9H-Fluorene-2,7-diamine (VB-FNPD) is a thermally cross-linked polymer HTL used instead of TFB. **Figure 5.3a** shows

the PL spectra of the device initially and after subjecting it to 24 hours of electrical stress. There is also a reference device in storage to have a record of temporal changes without any bias, as shown in **Figure 5.3b**. The insets show the PL spectrum of VB-FNPD single film. As can be seen, B-QDs PL intensity is increased to some extent over time due to the encapsulation defect passivation effect. Notably, the electrical stress exhibits minimal influence on the PLQY of the B-QDs, evidenced by the negligible change in the PL spectrum under bias. Therefore, comparing the results from **Figure 5.2a** and **Figure 5.3a**, it is evident that TFB experiences significant degradation under electrical stress, resulting in the creation of quenching sites for B-QDs. Consequently, both materials show a considerable PLQY loss.

a) b)

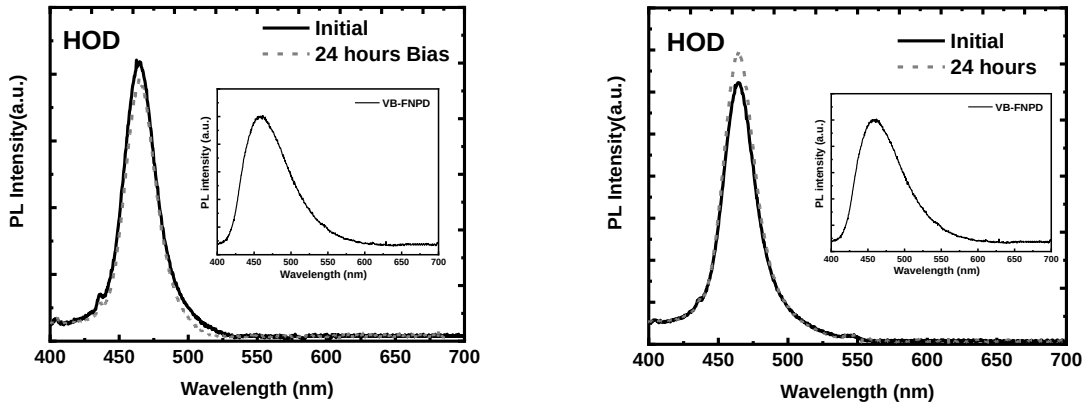

Figure 5.3 PL spectra of encapsulated HODs with the structure of Glass/ITO/PEDOT:PSS(40 nm)/VB-FNPD(20 nm)/B-QD(20 nm)/CBP(20 nm)/MoO_3(5 nm)/Al(100 nm) a) initially and after 24 hours of bias with a current density of 20 mA/cm^2 b) initially and after 24 hours of storage. The insets show the VB-FNPD film PL spectrum. The excitation wavelength is 330 nm.

5.1.4 Comparing Upright B-QLEDs using TFB vs. VB-FNPD HTLs

Indeed, although TFB is a commonly used HTL in B-QLEDs allowing for high efficiencies, the results suggest that TFB is not electrically stable, potentially leading to the B-QLED degradation during operation. On the other hand, VB-FNPD seems to be stable under electrical stress. Hence, a comprehensive comparative study is conducted, assessing the differences between the two HTLs (TFB

and VB-FNPD) in terms of solvent resistance, film morphology, and the B-QLEDs' efficiency and electrical stability.

a)

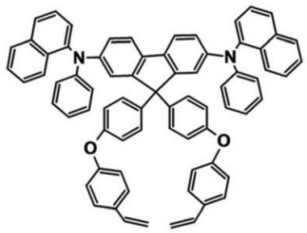

VB-FNPD

b)

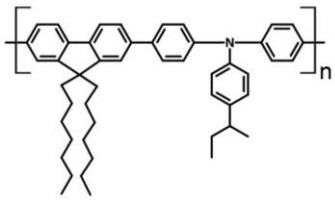

TFB

c)

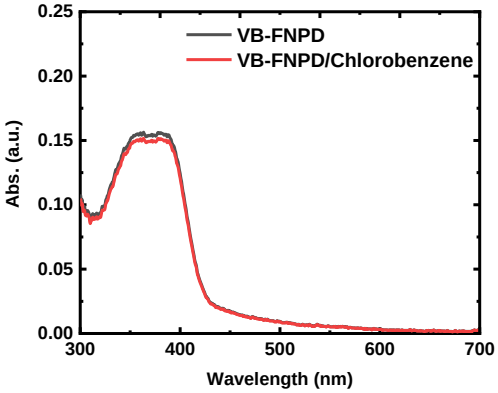

d)

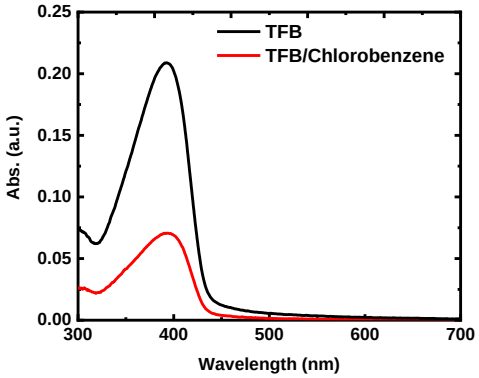

e)

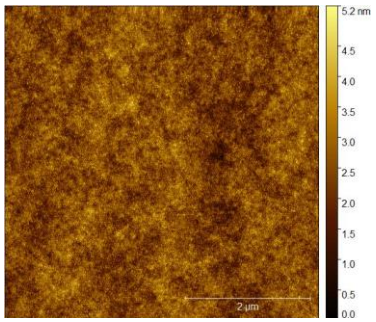

f)

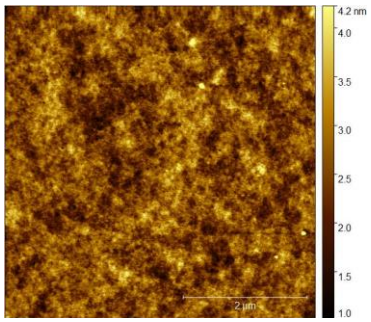

Figure 5.4 Chemical structures of a) VB-FNPD b) TFB. UV-Vis absorption spectra of c) VB-FNPD (d) TFB before and after rinsing with chlorobenzene. AFM images of e) VB-FNPD f) TFB coated on ITO/PEDOT:PSS substrates.

In all-solution-processed devices, solvent resistance of the layers is of high importance, because the morphological properties of the films can change during the successive spin coating steps, and it would affect the device's efficiency and EL stability. Therefore, to compare the two HTLs, UV-Vis absorption spectra of the HTL films are collected before and after being rinsed with chlorobenzene, as the solvent used for HTL solutions. The UV-Vis spectra of the HTLs are presented in **Figures 5.4c** and **d** along with their molecular structure in **Figures 5.4a** and **b**. As can be seen, TFB film absorption is greatly decreased after being exposed to chlorobenzene, indicating that the film can be partially washed off by exposure to the solvent. In contrast, the VB-FNPD absorption spectrum is changed negligibly when it is rinsed by the solvent, suggesting that VB-FNPD is crosse-linked during the annealing and is no longer soluble in its prior solvent. In addition, we probe the surface morphology of the HTLs. Since the QD emission layer (EML) is coated on HTL in the upright device architecture, any roughness or pinholes would affect the EML or subsequent layers' film quality leading to nonuniformities and thus poor device stability[66, 82]. **Figures 5.4e** and **f** demonstrate the AFM surface scans from a 20 nm-thick HTL film spin-coated on ITO/PEDOT:PSS substrates. The root-mean-square surface roughness (Rrms) for TFB and VB-FNPD were 1.8 nm and 0.4 nm, respectively. TFB shows more aggregation and nonuniformities as compared to VB-FNPD. Therefore, VB-FNPD gives smoother films which can be an advantage to have stable devices.

The VB-FNPD HTL suitable film properties and its energy level similarities with TFB make it a promising alternative candidate to TFB for use in B-QLED, aiming to enhance the device's EL stability. Upright B-QLEDs with the structure of Glass/ITO/PEDOT:PSS(40 nm)/HTL(20 nm)/B-QD(20 nm)/ZnMgO (60 nm)/Al(100 nm) are fabricated and compared using TFB or VB-FNPD as the HTL. The devices are encapsulated and their key performance characteristics are presented in Table 5.1.

Table 5.1 summary of the key performance characteristics of the B-QLEDs

HTL	V_{on} (V)	Performance at 20 mA cm^{-2} driving current density			
		Luminance (cd m^{-2})	Driving Voltage(V)	EQE (%)	CIE (x,y)

TFB	2.6	1170	3.02	5.8	(0.139, 0.077)
VB-FNPD	2.8	754	3.6	4.2	(0.137, 0.066)

Figure 5.5a shows the J-V-L characteristics of the devices. The turn-on voltage, the voltage for the onset of electroluminescence taken here as reaching an electroluminescence of 10 cd/m^2, for both devices is roughly close to the bandgap of B-QDs emitting at 470 nm luminance peak emission. The turn-on voltage and threshold voltage in VB-FNPD QLED are almost similar to those of TFB QLED which is not surprising given the very similar HOMO energy levels in both HTLs, and therefore, the hole injection barrier is identical in both cases. In addition, the VB-FNPD device has a lower current density at any given voltage in comparison to the TFB device. This can be attributed to lower hole mobility in VB-FNPD ($\mu_h \sim 10^{-4}$ cm^2 V^{-1}S^{-1})[119] versus that of TFB ($\mu_h \sim 10^{-3}$ cm^2 V^{-1}S^{-1})[67].

a) b)

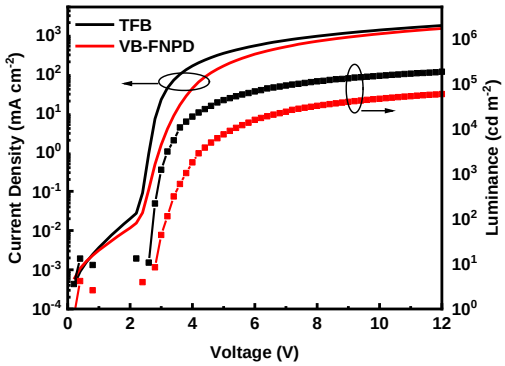

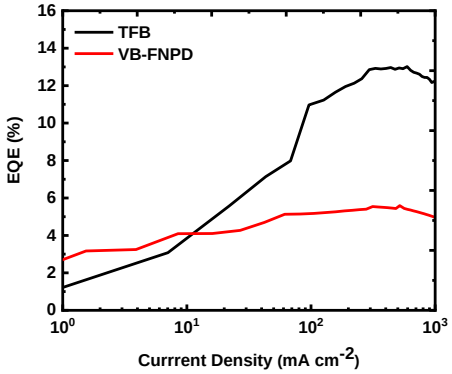

c) d) e)

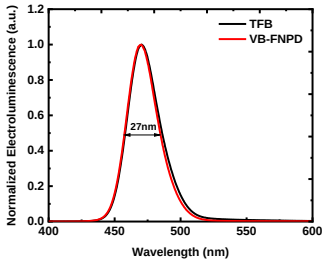

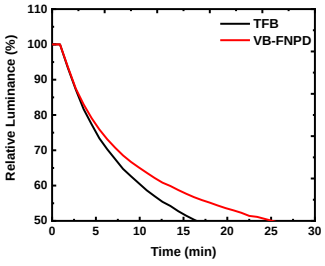

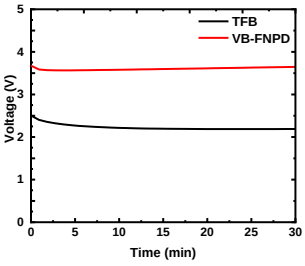

Figure 0.5 a) J-V-L characteristics b) EQE vs current density characteristics c) Normalized EL spectra of the B-QLEDs. d) Change in luminance normalized to the initial value vs. time. e) Change in driving voltage vs. time. Devices driven with a constant current density of 20 mA cm^{-2}.

Figure 5.5b presents the EQE versus current density characteristics. The EQE values at 20 mA/cm^2 driving current density are 5.8% and 4.2% in the case of TFB and VB-FNPD, respectively. The differences in efficiencies can possibly be due to the more injected holes in TFB QLEDs resulting in more electron injection efficiency into the QD layer due to Coulombic interaction[56] leading to a higher electron-to-hole ratio in the case of TFB. The EL spectra in **Figure 5.5c** show a single emission band with a peak at wavelength 470 nm and a full-width half maximum (FWHM) of 27nm.

Figures 5.5d and **e** present the change in normalized luminance (relative to the initial luminance, L_0) and the driving voltage over time (driving voltage at the time, t) operated under a constant driving current density of 20 mA/cm^2. The B-QLED with TFB exhibits an LT50, defined as the time passed for L_0 to degrade by 50% under continuous electrical driving, of 16 min (for a L_0 of 1170 cd m^{-2}). This translates to an LT50 of 22h at an L_0 of 100 cd m^{-2} using the lifetime equation of L_0^n LT50 = constant, where n is the acceleration factor of 1.8, commonly used for QLEDs. In contrast, the LT50 of VB-FNPD B-QLED is 25 min (for an L_0 of 754 cd m^{-2}) which corresponds to 16h for an L_0 of 100 cd m^{-2}. The lifetime results coincide with no big change in driving voltage that is different from what usually is observed in the aged devices' voltage trend. Therefore, it is likely that the fast EL loss is not due to a permanent degradation caused by charge accumulation at any interfaces in the device.

5.1.5 Comparing Upright G-QLEDs using TFB vs. VB-FNPD HTLs

Despite the VB-FNPD thin film advantages making it promising for potentially improving the B-QLEDs EL stability, the results show that the B-QLED using VB-FNPD exhibits shorter converted LT50 compared to the TFB device. This suggests that the poor EL stability of B-QLEDs may not mainly be due to HTL degradation. However, to further verify the role of HTL in the device EL stability and distinguish whether B-QLEDs are any different from the QDs with different emission peaks, green QLEDs (G-QLEDs) with the same structures are fabricated and compared.

Figure 5.6a shows the J-V-L characteristics of the upright G-QLEDs using VB-FNPD or TFB as the HTL. Here again, the turn-on voltage for both devices is observed at a bias that roughly corresponds to the bandgap of the G-QDs (2.3 eV). The turn-on and threshold voltages in the case of VB-FNPD and

TFB are similar. In addition, the VB-FNPD G-QLED has a lower current density at any given voltage than the TFB device, as in B-QLEDs, due to the different hole mobility in the HTLs.

Figure 5.6b depicts the change in normalized luminance and the changes in driving voltage over time of the devices under continuous driving at a constant current density of 20 mA/cm^2. The TFB G-QLED exhibits an LT50 of 35 h (from a L_0 of 15600 cd m^{-2}). This translates to an LT50 of 4900 h at an L_0 of 1000 cd m^{-2}. In contrast, the LT50 of VB-FNPD QLED reaches 145 h (for an L_0 of 10600 cd m^{-2}) which corresponds to 10100 h for an L_0 of 1000 cd m^{-2} which is two times higher than that of the TFB device. Clearly, replacing TFB with VB-FNPD results in a higher EL stability that overcompensates for the somewhat lower EQE of the VB-FNPD devices.

a) b)

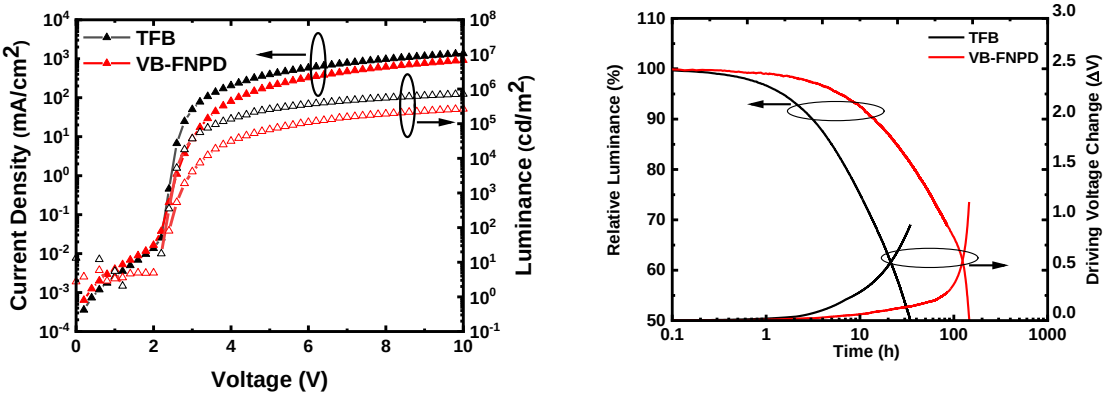

Figure 5.6 a) J-V-L characteristics b) Change in luminance normalized to the initial value and change in driving voltage vs. time. Devices driven with a constant current density of 20 mA cm^{-2}.

The study is further continued to understand the reason for higher EL stability in G-QLEDs using VB-FNPD. One of the possible factors for device degradation is charge imbalance leading to exciton quenching and charge accumulation in the device. Therefore, to identify the charge distribution in the two G-QLEDs, the capacitance-voltage-luminance (C-V-L) characteristics of the devices are measured and compared. **Figures 5.7a** and **b** present the C-V-L characteristics for the TFB and VB-FNPD G-QLEDs. At reverse bias, the capacitance corresponds to the geometric capacitance of the three HTL, G-QD, and ETL layers in their depleted state, which can be treated as planar capacitors connected in

series. As the bias voltage increases to positive values, since electrons and holes have different injection thresholds and mobilities, one of the carriers is injected first. Thus, one of the charge transport layers is removed from the depletion region, resulting in an abrupt increase in the capacitance. This persists until the applied electric field becomes high enough for the injection of the counter carriers and subsequent radiative recombination to start to happen. This phenomenon is marked by the observed capacitance drop at the onset of efficient electron-hole recombination.

a) b)

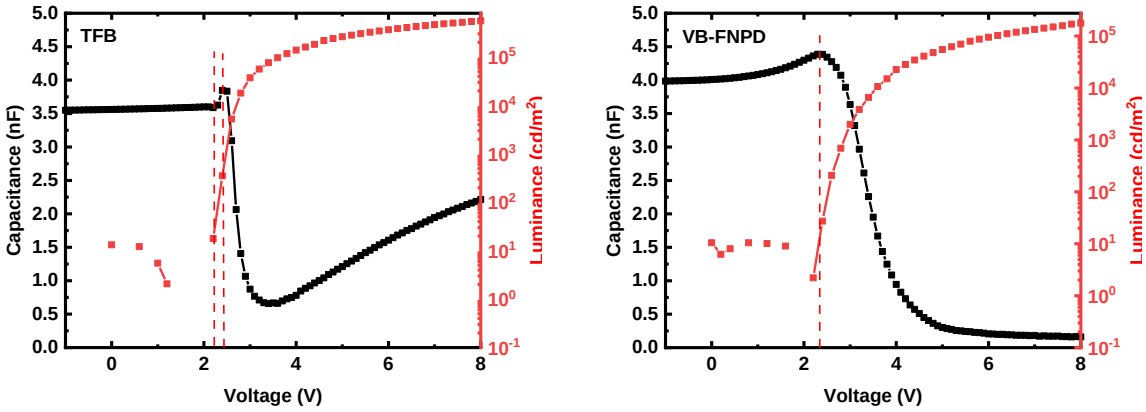

Figure 5.7 The C-V-L characteristics of G-QLEDs using a) TFB, and b) VB-FNPD as the HTL.

Looking at the case of the VB-FNPD G-QLED, one can see that the turn-on voltage coincides with the capacitance peak, both occurring at ~ 2.3 V, and that at higher biases the capacitance drops to near zero and stays unchanged for all luminance levels. In the case of the TFB G-QLED, on the other hand, the turn-on voltage is observed at 2.2 V; whereas the peak capacitance occurs at a higher voltage, 2.5V. Since there is always a strong competition between fast non-radiative Auger recombination and radiative recombination, having the peak capacitance occurring at a higher voltage than what is needed for efficient radiative recombination may suggest significant Auger quenching pointing to charge build-up at the interfaces. Such increased charge build-up may be a leading factor in the lower stability of the TFB device[54, 120-121]. Furthermore, different from the VB-FNPD device, the capacitance increases with voltage from its minimum value. This observation again suggests significant charge accumulation in the TFB device at the higher voltages. The C-V-L measurements therefore point to significant

differences in charge accumulation between the two devices, with VB-FNPD being more advantageous. The reduction in charge accumulation when using VB-FNPD is perhaps one of the main factors behind the higher EL stability of VB-FNPD devices.

Thus, the results show that using VB-FNPD improves charge balance and therefore, EL stability in G-QLED. However, replacing TFB with VB-FNPD in the case of B-QLEDs is not beneficial for the devices' EL stability despite the higher PL stability of VB-FNPD HODs under electrical stress. Therefore, other contributing factor(s) might be responsible for the B-QLEDs' fast EL loss which is possibly of higher priority than TFB degradation.

5.2 Conclusions

The findings of this chapter show that electrons are not detrimental to B-QDs PLQY. However, hole current flow significantly affects the TFB which leads to PLQY loss of TFB and B-QDs. The results show that the thermally cross-linked HTL (VB-FNPD) instead of TFB leads to stable PLQY of B-QDs in HODs under electrical stress. Having a smoother film with more cross-linking properties makes VB-FNPD a possibly promising alternative for TFB. Comparing the data of upright G-QLEDs using TFB or VB-FNPD confirms that VB-FNPD devices have higher EL stability by a factor of two. The C-V-L measurements showed that VB-FNPD establishes a better charge balance in the devices. However, replacing the TFB with VB-FNPD shows almost no change in the B-QLEDs EL stability implying that TFB degradation is unlikely to be the fundamental reason behind the fast EL loss in B-QLEDs. Therefore, further exploration is needed to identify the fundamental contributing factor that results in B-QLEDs' rapid EL loss and affects the devices more predominantly than the TFB degradation.

Chapter 6

Changes in Hole and Electron Injection under Electrical Stress and the Rapid Electroluminescence Loss in Blue Quantum-dot Light-emitting Devices

The material in this chapter has been published in "Changes in Hole and Electron Injection under Electrical Stress and the Rapid Electroluminescence Loss in Blue Quantum-Dot Light-Emitting Devices". Small 2023, 2304580. It has been reprinted with permission from the publisher.

In this chapter, the root causes of the EL loss that occurs under electrical bias in B-QLEDs are investigated. Comparative PL and EL measurements are conducted on B-QLEDs as well as on QLEDs that combine blue and red QDs in various configurations. Electrical measurements on single-carrier devices are also carried out. Results show that the EL loss stems primarily from a deterioration in charge balance caused by changes in hole and electron injection in the B-QDs that occur while the devices are under electrical bias, and is not associated with permanent changes in the QDs or their PLQY as is sometimes suspected[12, 122-123]. The changes in charge injection are also found to be partially reversible upon stopping the electrical bias, and therefore using pulsed (instead of continuous) electrical driving can slow down some of these effects, resulting in a 2.5X longer device LT50, from the same initial luminance of 500 cd/m^2 and at a similar average current density of 10 mA/cm^2. C-V measurements on unaged and electrically-aged devices compared with J-V-L characteristics show that the threshold voltage decreases and the turn-on voltage increases after aging due to the changes in charge injection efficiencies which are corroborating these conclusions.

6.1 Results and Discussions

The EL stability behavior of B-QLEDs with the following structure is studied: ITO (100 nm)/PEDOT: PSS (40 nm)/TFB (20 nm)/ QDs (20 nm)/ZnMgO (60 nm)/Al (100 nm). The device structure is depicted in **Figure 6.1a**. In this structure, ITO and Al function as hole and electron-injecting contacts, respectively, whereas PEDOT:PSS, TFB, and ZnMgO function as hole injection layer, HTL, and ETL, respectively. A group of 12 devices of the same structure are tested. **Figure 6.1b** shows the typical J-V-L characteristics of these devices. The turn-on voltage is observed at a bias that roughly corresponds to the bandgap of the B-QDs (2.6 eV). **Figure 6.1c** shows the B-QLEDs' EQE versus the current density (EQE-J) with a maximum EQE of 13%. **Figure 6.1d** presents the change in EL luminance (normalized to the initial luminance value, L_o) and the driving voltage of one of these QLEDs under continuous electrical driving at a constant current density of 20 mA/cm^2. The B-QLED exhibits fast EL loss and its EL stability is much poorer than that of other colors[124-125]. The driving voltage slightly decreases and remains constant during the aging. Data from a R-QLED using the same CTLs and encapsulation are also provided in **Figure S6.1** for comparison.

To investigate whether the EL loss in the B-QLEDs stems from changes in the PLQY of the B-QDs due to the electrical stress, PL spectra under 330nm were collected every 5 minutes during the stress (with the bias temporarily stopped in order to allow collecting the PL signal without inadvertently collecting EL). As can be seen in **Figure S6.2a**, the PL spectra of the B-QLEDs are comprised of two peaks at 436 nm, and 467 nm. The 436 nm band corresponds to emission from TFB whereas the 467nm band arises primarily from the QDs with some small contributions from TFB which also emits at this wavelength. As can be seen in **Figure S6.2a**, since the 436 nm peak does not change over time, one can conclude that the small changes (~10%) in the intensity of 467 nm band are exclusively attributed to the B-QDs. Changes in B-QDs PL intensity over time, normalized to the initial value, are shown in **Figure 6.1d**. As can be seen, while the PL intensity decreases over time, signifying a decrease in PL, the change is below 10 %, much smaller than the corresponding EL loss (PL spectra collected under 405 nm excitation, and also at 440 nm where the absorption by TFB is negligible, are also provided in **Figures S6.2b** and **c** for comparison, again proving that the changes in QD PL are indeed small and are not confounded by TFB background). The decrease in PL could be due to the well-known QD charging effects[56] during the device operation. The much smaller decrease in PL indicates that QD PLQY losses are not the primary reason behind the device's EL loss. The small decrease in PL also suggests that the poor EL stability of B-QLED is not associated with permanent damage (e.g., irreversible chemical

changes) in the B-QDs. The much larger EL vs PL loss suggests that the EL loss must be associated with factors that are unique to the electrical excitation process of the QDs, such as, for example, i) gradual changes in electron/hole supply to the QD, or in their confinement within the QD under electrical stress, or ii) charge buildup either within the QD layer or at its interfaces with the CTLs that activates charge-mediated quenching pathways (e.g. via trions and/or Auger quenching) temporarily reducing the PLQY.

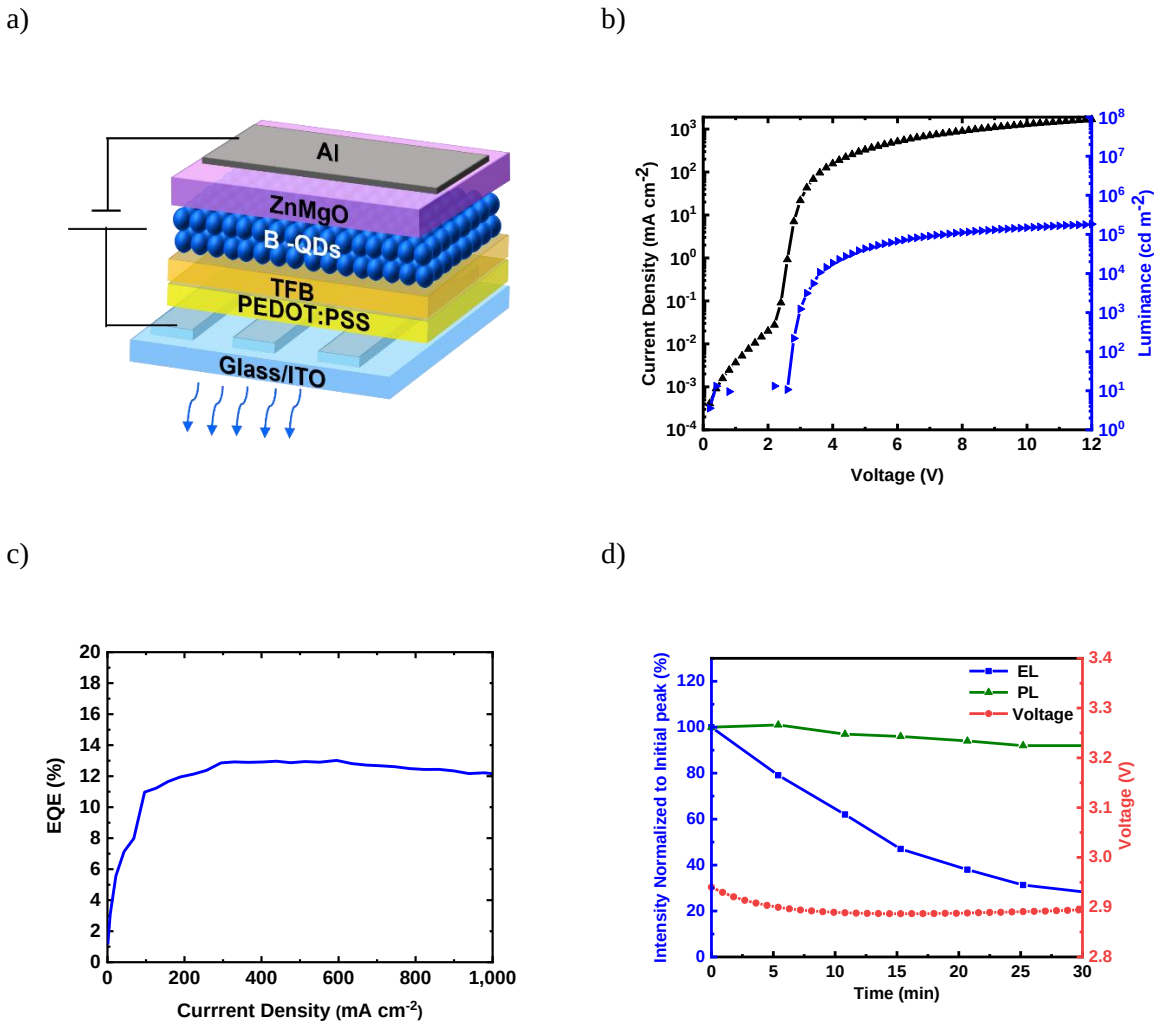

Figure 6.1 a) A schematic diagram of the B-QLED structure b) J-V-L characteristics of the B-QLED c) EQE versus current density of the B-QLED d) EL and PL (excitation wavelength,330 nm) intensities of B-QDs normalized to their initial value, and driving voltage of the B-QLED as a function of time under a constant driving current density of 20 mA/cm^2.

In order to probe the underlying causes further and investigate if the CTLs play a role in the degradation behavior, we fabricate and test another set of devices in which a small amount of R-QDs is doped into the B-QD layer for comparison. The device structure is the same as before except that the B-QD emission layer is doped with R-QDs (at 1 wt.%). **Figure S6.3** shows the J-V-L characteristics of one of these devices (denoted by B:R) and of a neat B-QLED for reference. At voltages above the threshold voltage, the two devices have essentially identical characteristics except that the B:R QLED has a slightly lower turn-on voltage (2.4 V vs. 2.6 V) which may be attributed to a slightly smaller barrier for charge injection into the narrower band-gap R-QDs suggesting that a fraction of the R-QDs must be contacting at least one of the two CTL interfaces (i.e. not all R-QDs are surrounded by B-QDs). The device also shows higher leakage currents (currents at voltages <2.2 V), which can also be attributed to the somewhat easier injection. **Figure 6.2** shows EL and PL spectra of the B:R QLED collected at 5-minute intervals during electrical driving at a constant current density of 20 mA/cm^2. The EL spectra consist of two distinct bands with peaks at 470 nm and 627 nm which correspond to the B- and R-QD emission peaks, respectively. The PL spectra – again collected under 330 excitation and while the bias is temporarily turned off - are comprised of three peaks at 436 nm, 467 nm, and 625 nm corresponding to TFB, B-QDs, and R-QDs, respectively. The 625 nm band is much weaker relative to the 467nm band indicating that energy transfer from the B- to the R-QDs is very limited and that most of the EL from the R-QDs in the B:R QLED must be due to e-h recombination on the R-QDs directly as opposed to being the result of energy transfer from the B-QDs. Despite the presence of the R-QDs, the intensity of the blue EL again decreases to 50% of its initial value in only 15 min; exhibiting a similar decay rate as that in the neat B-QLEDs observed earlier. Interestingly, and in stark contrast to the blue EL band, the intensity of the red EL band does not decrease over the same period of time; and instead increases. The fact that the R-QDs EL does not similarly decrease despite being in the same device stack and supplied carriers by the same CTLs rules out the possibility that the fast loss in blue EL might be the result of degradation in the CTLs or charge accumulation-induced quenching at the CTL interfaces. Knowing that R-QDs layers tend to be electron-rich whereas B-QDs layers tend to be hole-rich even when supplied through the same CTLs[126], the observations suggest that the changes in EL could be associated with an increase in h/e currents ratio across the emission layer during the electrical stress that further reduces the charge balance for the B-QDs while possibly improving it for the R-QDs. Here again, the changes in the intensity of the two bands in the PL spectra due to the electrical stress are very little indicating that the EL changes are not due to aging-induced changes in

the PLQY of the materials and suggesting that the EL changes may predominantly be due to changes in charge balance or in their confinement within the QD layer.

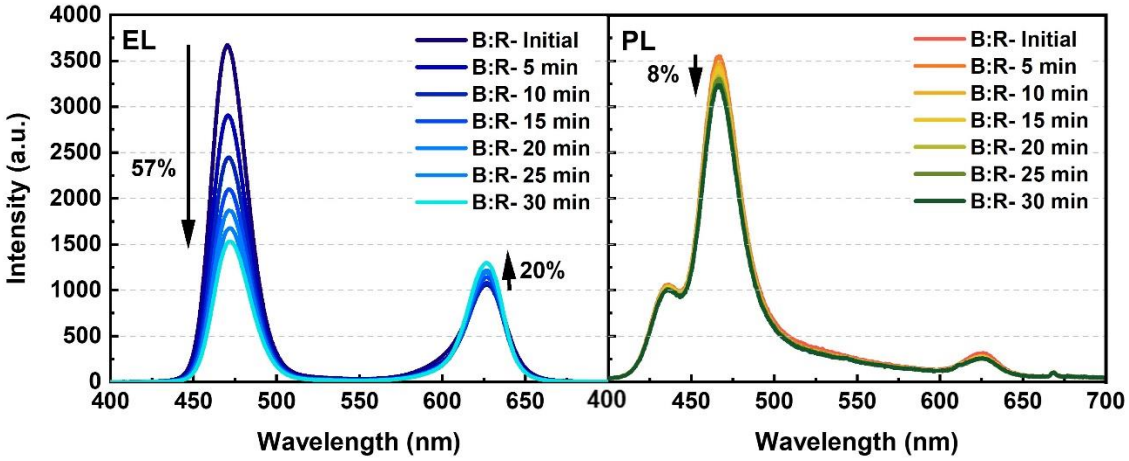

Figure 6.2 EL and PL spectra of the B:R QLEDs, both measured after the shown aging time under a constant driving current density of 20 mA/cm^2 driving. The excitation wavelength is 330 nm.

6.1.1 Single-Carrier Devices Electrical Characteristics

Having ruled out that the fast loss in EL from the QDs is caused by electrical stress-induced permanent chemical changes in the QDs, by degradation in the CTLs, or by charge accumulation at the CTL interfaces, we next investigate if it could be due to changes in charge injection into the B-QDs or in their accumulation (or confinement) within the B-QD layer. Due to the wider bandgap of B-QD relative to the other colors, charge injection into them can be expected to be more difficult. In addition, the wider band gap of the cores naturally leads to smaller core/shell energy offsets which would lead to weaker charge confinement in B-QDs than in other colors. As a result, one would expect them to be more susceptible to charging (e.g., due to the limited confinement of one type of charges (e.g., electrons) over the other (e.g., holes), leaving a larger population of the latter without recombination on the QD cores that can easily produce trion species) and/or loss of charge balance. Therefore, probing changes in electron and hole injection into B-QDs or in their confinement over time under electrical stress using single carrier devices might provide useful insights.

HODs with the structure of ITO/PEDOT:PSS/TFB/B-QD/MoO_3/Al and EODs with the structure of ITO/ZnO(sol-gel)/B-QD/ZnMgO/Al as shown in **Figures 6.3a** and **b** are therefore fabricated and

changes in their electrical characteristics are studied over time under electrical stress. The devices are driven under forward bias, defined as a bias where ITO has a more positive potential relative to Al as depicted in the figure. **Figure 6.3c** presents the driving voltage needed for maintaining a constant current of 20mA/cm^2 versus the time characteristics of these HODs and EODs.

Characteristics of similar devices but without the B-QD layers are also collected and provided in the same figure for comparison. As can be seen from the figure, the driving voltage of the EODs increases rapidly within the first few hours, indicating that electron injection and/or transport across the device layers becomes more difficult over time under bias, before the effect eventually plateaus. In the HODs, in contrast, the driving voltage decreases in the first few hours, pointing to hole injection and/or transport becoming easier. Since the voltage trends of the devices without B-QDs exhibit almost no changes under the same conditions, it can be concluded that the changes in the electrical characteristics of the EOD and HOD with the B-QDs arise from changes in charge injection and transport in the B-QD layers themselves, i.e. that the injection of electrons into the B-QDs layer and/or their transport across the layer becomes more difficult whereas the injection and/or transport of holes across the layer becomes easier.

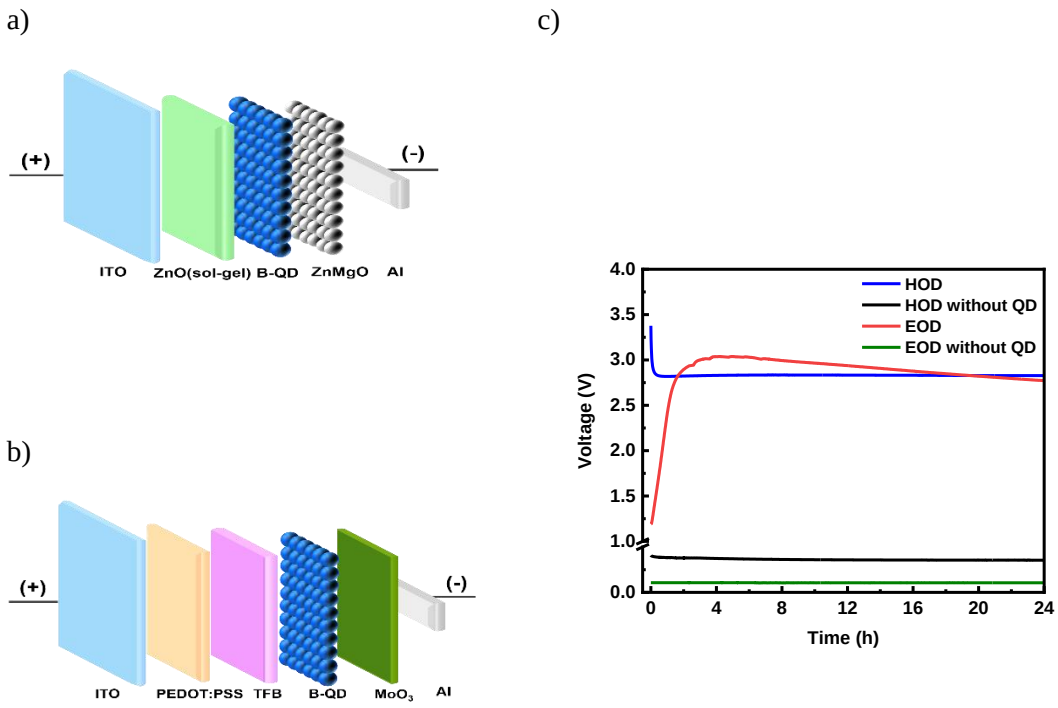

Figure 6.3 Structure schematic of a) EODs and b) HODs. c) Driving voltage versus time trends under constant current driving of EODs and HODs in a and b, and of similar ones without B-QDs, (ITO/ZnO(sol-gel)/ZnMgO/Al) and (ITO/PEDOT:PSS/TFB/MoO_3/Al), over time. All the devices are driven at a constant current density of 20 mA/cm^2.

To further investigate charge transport and injection changes in the B-QD layers, the J-V characteristics of the single carrier devices are analyzed. **Figures 4a** and **b** show the J-V characteristics of the HOD and EOD, respectively, on a log-log scale. The characteristics are collected before and after the electrical aging. Again, characteristics from the corresponding devices without the B-QDs are provided in **Figures S6.4a** and **b** for comparison.

In general, the J-V characteristics of single carrier devices consist of different regions representing four different regimes of power law dependence of J on V: Ohmic ($J \propto V$), trap space charge limited current (t-SCLC, $J \propto V^m$ $1<m<2$), trap-filled limited current (TFL $J \propto V^m$ $2<m<100$), and space charge limited current (SCLC, $J \propto V^2$)[127-129]. The Ohmic regime typically appears only in devices with

very low trap density and at very low voltages, thus is not usually observed especially for the voltage ranges tested here[128]. As shown in **Figure 6.4a**, the J-V characteristics of the unaged HODs only show t-SCLC and TFL regions with the SCLC region appearing at high voltages and only after aging. Although the t-SCLC current slightly decreases at low voltages after aging, which can be due to a small increase in shallow traps[128], the TFL regime starts to appear at lower voltages allowing for the appearance of the trap-free SCLC regime for the aged device. The V_{TFL}, the transition voltage between the TFL and trap-free SCLC regimes and at which the traps become filled is determined by[130]:

$$V_{TFL} = \frac{en_t L^2}{2\varepsilon_r \varepsilon_0} \qquad (6.1)$$

Where e represents the elementary charge, n_t the trap density, L the layer thickness, ε_0 vacuum permittivity, and ε_r the relative dielectric permittivity. Therefore, for a constant L, the value of V_{TFL} will depend on the density of trap states. As shown in **Figure 6.4a**, the V_{TFL} shifts to lower voltages suggesting that the density of hole traps gradually decreases after electrical aging possibly due to them being filled by charges over time, allowing for the current to start to increase more rapidly at lower bias voltages. In addition, the trap-free SCLC regime, which is not observed in the unaged devices, emerges due to lower trap density in the aged devices [127]. While the exact mechanism behind the reduction in trap density is still unknown, preliminary results from measurements on QDs with different ligands suggest that ligands may be playing a role in this behavior.

Turning our attention now to EODs characteristics in **Figure 6.4b**, it can be seen that – in contrast to the case of the HODs- the current considerably decreases after the aging, suggestive of an increase in the number of electron trap states. In addition, the V_{TFL} shifts to higher voltages is consistent with increased trapping. Although the underlying mechanism behind the increased trap states is also uncertain, one possible reason could be hole leakage to the ETL which has been reported to increase trap states in ZnO[97], an effect that may be exacerbated by the high h/e ratios in B-QLEDs.

The results from the HOD and EOD devices therefore convincingly show that the hole and electron supply efficiencies to the B-QDs change in opposite directions during electrical stress. With this change, one can expect the charge balance in the B-QD layer to deteriorate quickly especially considering that B-QD emission layers tend to generally have e/h <1 (i.e. are electron deficient) even before aging[126]. The deterioration in electron supply would reduce the number of excitons for potential radiative recombination. In addition, the increase in hole supply would lead to the buildup of a population of residual (i.e., unrecombined) holes in the B-QD layer which can lead to unfavorable

phenomena such as nonradiative Auger recombination. Auger recombination of positive trions has been shown to be more than ten times faster than neutral exciton radiative recombination[131]. This highlights the significantly detrimental quenching effect of increased hole concentrations in B-QLEDs.

a) b)

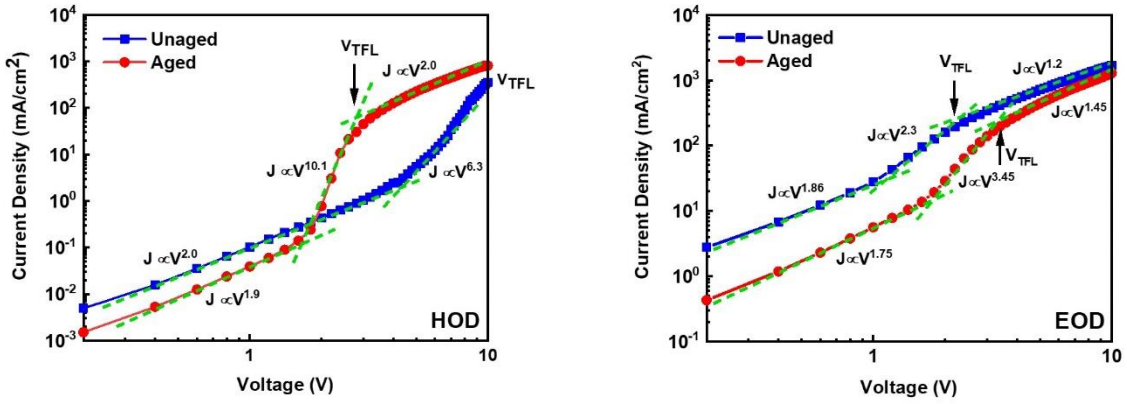

Figure 6.4 J-V characteristics of unaged and aged a) HODs and b) EODs. The devices are driven at a constant current density of 20 mA/cm^2 for 24 hours.

6.1.2 Marking Layer to Verify Charge Injection Changes in B-QLEDs

Seeing the results from the HODs and EODs, we use B-QLEDs that contain a thin layer of R-QDs as a marking layer to further verify the changes in charge injection in the full devices as the devices age. Devices that contain thin layers of R-QDs inserted in-between the B-QD layer and either the TFB HTL or the ZnMgO ETL, denoted by HTL/R/B/ETL and HTL/B/R/ETL, respectively are fabricated and tested. The devices structures are shown schematically in **Figure 6.5a**. (PL spectra from these devices are presented in **Figure S6.5**. The different blue-to-red band height ratios for the different orders of the QD layers prove that any intermixing between the layers during the fabrication process must be limited). The devices are aged for 24 hours under a constant driving current density of 20 mA/cm^2 and their EL spectra are compared.

a)

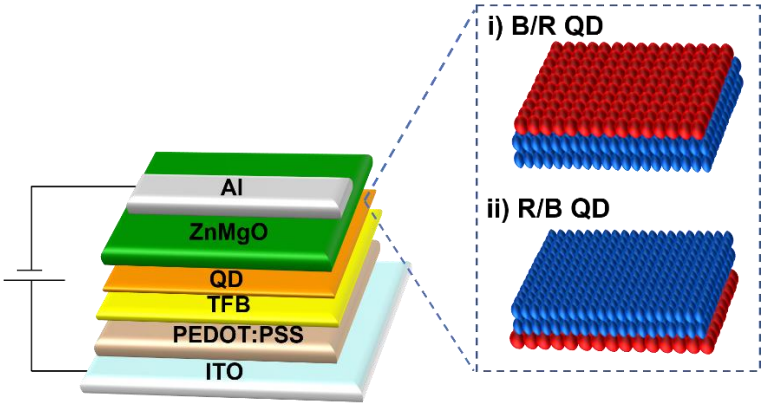

b)

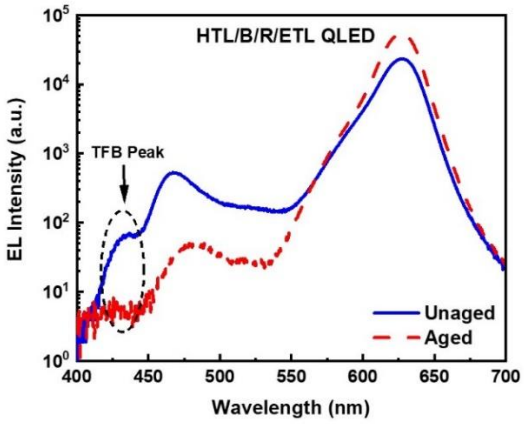

c)

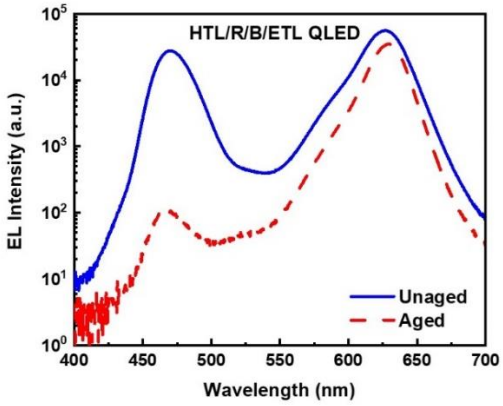

Figure 6.5 a) Structure schematic of (i) HTL/B/R/ETL QLED and (ii) HTL/R/B/ETL QLED. b) The EL spectra of unaged and aged HTL/B/R/ETL QLED. c) The EL spectra of unaged and aged HTL/R/B/ETL QLED. The devices are driven at a constant current density of 20 mA/cm^2 for 24 hours.

Figure 6.5b, shows the EL spectra of unaged and aged HTL/B/R/ETL QLED. The initial EL spectrum shows three bands with peaks at 436 nm, 470 nm, and 627 nm which correspond to emission from the TFB, B-QD, and R-QD layers, respectively, indicating that electrons and holes exist in all three layers. After aging, the TFB band becomes hardly visible suggesting that the number of electrons that cross the two QD layers and reach the HTL significantly decreases. This observation indicates that

electron injection and transport across the two QD layers indeed decrease as the devices age. Moreover, the intensity of the red band increases after aging, consistent with an increase in hole injection and transport across the B-QD layer as the devices age. These results therefore confirm that electron injection into the B-QDs decreases whereas hole injection and transport across them increases allowing more holes to escape towards the ETL as the devices age under electrical bias. The fact that the intensity of the red band increases also suggests that electron injection from the ETL to the R-QDs remains relatively efficient and indicates that the decrease in electron injection is limited to the B-QDs, a conclusion that is also supported by the observations from the B:R devices presented earlier (in **Figure 6.2**).

Figure 6.5c shows the EL spectra collected from the HTL/R/B/ETL QLEDs. Different from the former case, here we see no detectable emission from TFB, an effect that can possibly be attributed to efficient energy transfer from TFB to the R-QDs. Also, the height ratio of the 470 nm to the 627 nm bands is much higher in this case which can be directly attributed to the less efficient hole injection from the TFB into the R-QDs[126] or more efficient electron injection into B-QDs in this case compared to the former where the electrons are injected from R-QDs to the B-QDs which reduces h/e ratios and improves charge balance in the B-QD layer. More importantly, and opposite to the former case, the intensity of the R-QD EL band decreases after aging. This can be readily attributed to the fact that in this case, the electron supply to the R-QD layer occurs via the B-QDs, and therefore a deterioration in electron injection into the latter will necessarily affect both. Thus, the changes in EL spectra of the QLEDs with the marking layers further confirm our conclusions.

6.1.3 C-V-L Measurements

To further study the changes that occur in the devices as they age, C-V measurements are carried out in order to obtain further insights into changes in carrier injection and their subsequent recombination in the QLEDs[132]. **Figure 6.6a** shows the C-V and J-V-L characteristics of unaged and aged B-QLEDs.

For bias values below the threshold voltage, the device capacitance remains constant and corresponds to the geometric capacitance of the 4 mm^2 device with the four layers (PEDOT: PSS/TFB/B-QD/ZnMgO) in between the electrodes being depleted. As the voltage increases and reaches 2.2V, the threshold voltage, the carrier that is easier to be injected from the electrodes is injected first leading to a rise in capacitance for the unaged device. At this point, the electric field across the layers across which the carriers have been injected collapses and the field distribution in the device changes and becomes

limited to the layers that remain depleted [54, 62]. From the C-V characteristics, the maximum capacitance in the unaged devices (5.6nF) at this voltage corresponds to the geometric capacitance of the 60 nm thick ZnMgO layer (Ɛ~ 8.59)[133]. This shows that electrons are the secondly-injected carriers and that holes are injected first. This in turn indicates that hole injection is easier than electron injection in B-QLEDs and occurs first, leaving the ETL as the only layer remaining depleted until 2.6 V, the device turn-on voltage, when electrons also get injected, and the capacitance starts to drop rapidly due to efficient electron-hole recombination. As can be seen from the figure, the capacitance shows a small decrease between 2.0 V to 2.3 V in the aged device, the range over which only the firstly-injected carriers (i.e., the holes) are injected. This suggests that the holes are injected at lower voltage in the aged device compared to the unaged QLEDs, consistent with the hole injection becoming easier in the aged devices as previously observed.

In addition, the J-V-L characteristics also show a slightly lower threshold voltage (2.0 V instead of 2.2 V) for the aged device, which is consistent with the lower onset for hole injection in the aged device observed from C-V characteristics. Also, in the aged device, the maximum capacitance occurs at a higher voltage (2.8 V vs. 2.6 V), coinciding with the turn-on voltage, suggesting that electron injection into B-QDs requires a higher voltage. Thereafter, the capacitance decays at a slower rate suggestive of a lower charge annihilation rate which may be due to the less efficient electron injection in the aged device which reduces the electron-hole recombination rate and thus makes the capacitance decrease more slowly. Since the peak capacitance corresponds to the ZnMgO layer, the slightly smaller peak capacitance in the aged device can suggest that the ETL is not as depleted as in the unaged device possibly because of some residual charges in it associated with hole leakage. The J-V characteristics of the aged device show that at voltages above the electron injection onset (2.8V), the current density is lower than the unaged device which is consistent with the lower capacitance decay rate in the aged device.

Figure 6.6b shows the capacitance measured at different time intervals while the devices are being continuously driven at a constant voltage of 2.9 V, just above the turn-on voltage, corresponding to a current density of 20 mA/cm^2. As can be seen, the capacitance decreases in the first 40 seconds which might be due to efficient charge annihilation at the beginning but starts to increase after that. The gradual increase in capacitance can be an indicator of charge accumulation in the device which could possibly be due to the gradual increase in hole accumulation arising from the increase in hole injection in the B-QLEDs as they age [54]. **Figure S6.6** shows the C-V characteristics of the unaged devices, after

40s of electrical stress, after 720s of electrical stress (which corresponds to the LT50 of the device), and after 24 hours of electrical stress, to show the evolution of the C-V characteristics over time.

a) b)

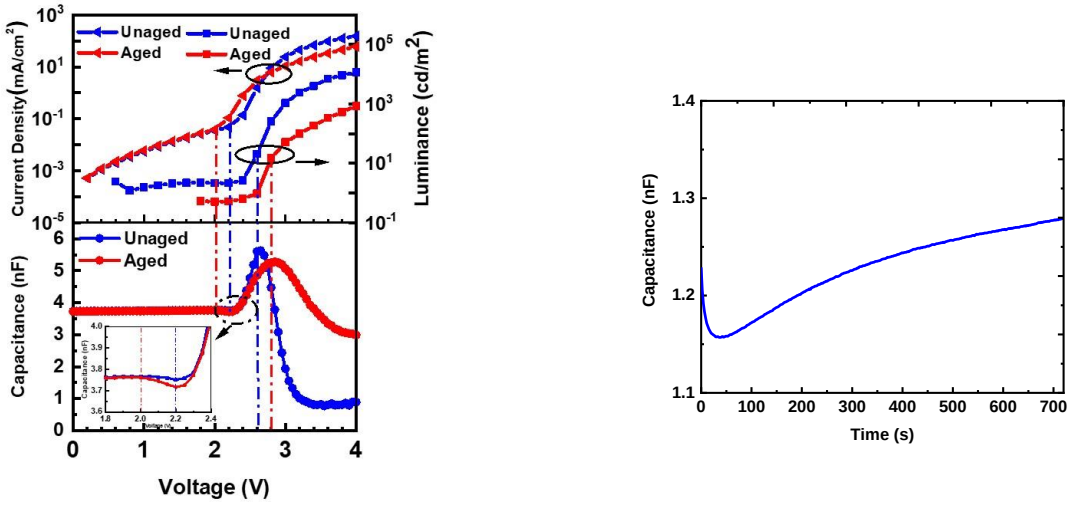

Figure 6.6 a) C-V and J-L-V characteristics of unaged and aged B-QLED. The devices are driven at a constant current density of 20 mA/cm^2 for 24 hours. b) Capacitance-time characteristics of B-QLEDs biased at 2.9 V.

6.1.4 Pulsed Vs. Constant Current Driving

Finding that the loss in EL in B-QLEDs under electrical bias is not associated with any permanent significant decrease in the QDs PLQY and that it arises primarily from changes in charge injection into the B-QDs that lead to a deterioration in charge balance and a possible hole accumulation (from the C-V results), the question whether the changes in charge injection would recover when the bias is stopped arises. To answer this question, we study the effect of interrupting the applied bias temporarily at fixed time intervals on the driving voltage versus time trends of the single carrier devices while they are being electrically driven. **Figure 6.7** shows the driving voltage trends of the EOD and HOD over time under forward bias driving at a constant current density of 20 mA/cm^2. The bias is paused for 30 minutes, first after 2 hours of driving and thereafter every hour, before the bias is resumed. As seen, the voltage changes in the single carrier devices recover to a significant extent after each pause showing that the aging-induced decrease in electron injection and the increase in hole injection in the B-QDs both recover upon electrical resting, a sign that the changes in charge injection are likely associated with charge accumulation and trapping in them. This partial recovery shows that the underlying phenomena

such as the trap filling or passivation in the case of the HODs and the increasing trap density of states in the case of EODs are reversible when the bias is removed.

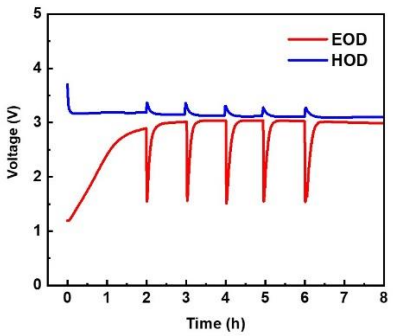

Figure 6.7 Driving voltage versus time trends under constant current driving of EODs and HODs driven at a constant current density of 20 mA/cm^2 with bias pauses for 0.5 hours.

The reversibility of the charge injection changes motivates us to investigate if aging the single carrier devices under pulsed current instead of continuous current driving would influence the voltage versus time trends. **Figure S6.7a** and **b** show the voltage of EOD and HOD over time under both pulsed current (50 Hz and 50% duty cycle) and continuous current driving, in both cases at an average current density of 10 mA/cm^2. The results show that using pulsed current bias can significantly reduce the changes in the driving voltage in both devices. The results suggest that using pulsed current instead of constant current bias helps reduce the charge accumulation – possibly due to allowing for some charge de-trapping to take place during the voltage pauses - in turn reducing the changes in charge in the B-QDs. These results point to charge trapping and accumulation in the B-QDs being a primary factor behind the aging-induced decrease in electron injection and increase in hole injection in these materials and the subsequent rapid EL loss. The results also suggest that using pulsed current instead of constant current bias may help slow down the EL loss in B-QLEDs thus making it possible to extend their operational lifetime.

To investigate and verify this possibility, comparative EL stability measurements are conducted on B-QLEDs under pulsed (again at 50 Hz and 50% duty cycle) and continuous current driving scenarios. To make the comparison more accurate, the amplitude of the pulsed current was set to 20 mA/cm^2,

double the value used for the continuous current driving scenario (10 mA/cm^2) such that both devices have the same average current density over time.

a) b)

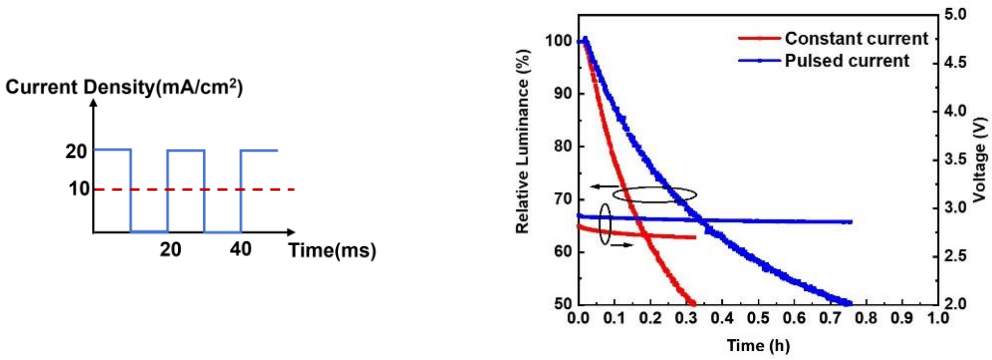

Figure 6.8 a) Schematic diagram of pulsed current and constant current bias b) Voltage and luminance, normalized to the initial value of B-QLEDs versus time, aged under an average current density of 10 mA cm^{-2} driving.

Figure 6.8b presents the changes in the EL luminance (normalized to the initial luminance, L_0) and the driving voltage of the QLEDs under the two driving scenarios. The continuous current driving scenario results in an LT50 of 0.32 h whereas using the pulsed current bias leads to an almost 2.5X longer LT50 of 0.78 h (both from a L_0 of 500 cd/m^2). The longer LT50 upon using pulsed driving can of course be directly connected to the role of the voltage pauses in helping reduce the charge trapping in the B-QDs that over time reduces electron injection and increases hole injection into them as was observed from the HOD and EOD results; both of which are evidently primary reasons behind the rapid EL loss in B-QLEDs thus their short EL lifetime.

6.2 Conclusions

In summary, this chapter shows the results of studying the root causes behind the B-QLEDs' low EL stability. Comparing the EL and PL spectral changes of B-QLEDs and B:R QLEDs under bias shows that the significant EL loss is not associated with PLQY loss in the B-QDs or CTLs material damage

but is mainly due to changes in charge injection. Analyzing the electrical characteristics of HODs/EODs in the unaged and aged devices suggests that hole injection into B-QDs increases over time while electron injection decreases, leading to a deterioration in charge balance. These changes arise from a modulation of hole and electron trap densities during electrical aging. Changes in EL spectra of devices with a marking layer confirm the reduction in electron supply in the B-QDs over time. Moreover, capacitance versus time, C-V measurements along with J-V-L characteristics of B-QLEDs confirm the charge injection changes over time under bias and that excess holes accumulate in the QD layer. The charge injection changes are also found to be reversible at least in part when the bias is removed. Therefore, driving the B-QLEDs under pulsed current instead of constant current extends the devices lifetime 2.5X at the same initial luminance; confirming that charge trapping and accumulation in B-QDs is one of the main factors that reduce the B-QLEDs operational lifetime. These results uncover the critical role of changes in charge injection in the fast EL loss of B-QLEDs and highlight the necessity of developing B-QDs that can establish more efficient and sustainable carrier injection with the currently used CTLs to achieve more stable B-QLEDs.

Chapter 7

Hole-Induced Degradation of ZnMgO and Its Role in the Limited Electroluminescence Stability of Blue Quantum Dot Light-Emitting Devices

The material in this chapter has been reprinted from the manuscript "Hole-Induced Degradation of ZnMgO and Its Role in the Limited Electroluminescence Stability of Blue Quantum Dot Light-Emitting Devices", Submitted.

In this chapter, it is elucidated that holes leak across the ZnMgO layer in blue QLEDs (B-QLEDs), and adversely affect the ETL, and consequently the device stability. Introducing a marking layer in B-QLEDs is used to confirm that holes escape the QDs layer and penetrate the ETL. To discern the potential effect of carriers, namely holes and electrons, on the ZnMgO layer, we design hole-rich and electron-rich device structures. The steady-state PL measurements reveal that holes are detrimental to the ZnMgO layer whereas the electrons exhibit minimal impact. The subsequent investigations involve using the pre-aged ZnMgO layers in inverted green QLEDs (G-QLEDs) following a series of peel-off and fabrication processes. The TRPL characteristics of the G-QLEDs show changes in optical and electron injection properties of the ZnMgO layer when subjected to holes. The change in electron injection property of the ZnMgO layer is further proved by altering the hole-to-electron (h/e) ratios in upright B-QLEDs, resulting in varying degrees of degradation occurring in the ETL. The results uncover a critical factor contributing to the limited stability of B-QLEDs.

7.1 Results and Discussion

Initial investigations are carried out on B-QLEDs with the following upright architecture: ITO (100 nm)/PEDOT:PSS (40 nm)/TFB (20 nm)/B-QD (20 nm)/ZnMgO (60 nm)/Al (100 nm). ITO and Al serve as hole- and electron-injecting contacts, respectively. PEDOT:PSS, TFB, and ZnMgO function as HIL, HTL, and ETL, respectively. To verify whether holes can escape the B-QDs layer, the upright B-QLED device structure is altered to contain a red fluorescent organic emitter as a marker placed in the ETL with minimal overlap with the emission peak of the B-QDs. **Figure 7.1a** depicts the schematic diagram of the B-QLED with the marking layer. The structure resembles the regular B-QLED except that the ZnMgO layer thickness is reduced to half and instead, a thin vacuum-deposited layer is replaced. A 20 nm-thick layer composed of organic ETL, 2,2′,2″-(1,3,5-benzinetriyl) tris(1-phenyl-1H-benzimidazole) (TPBi) doped with 5% florescent red emitter 4-(dicyanomethylene)-2-t-butyl-6-(1,1,7,7-tetramethyljulolidyl-9-enyl)-4H-pyran (DCJTB) is used to examine exciton formation in the ETL. **Figure 7.1b** shows the EL spectra of a regular B-QLED versus the B-QLED with the marking layer. As can be seen, both EL spectra show a peak at 471 nm corresponding to the B-QDs emission. In addition, the B-QLED with marking layer shows another peak at 605 nm which corresponds to the red emission from the marking layer in the ETL. The presence of the red emission peak is an indicator of exciton formation and radiative exciton recombination in the ETL, indicating that there must be leakage through the ZnMgO layer. Thus, one can conclude that there is hole leakage in B-QLEDs that can travel across the ZnMgO layer confirming the presence of positive charges in the ZnMgO layer during the device operation.

a) b)

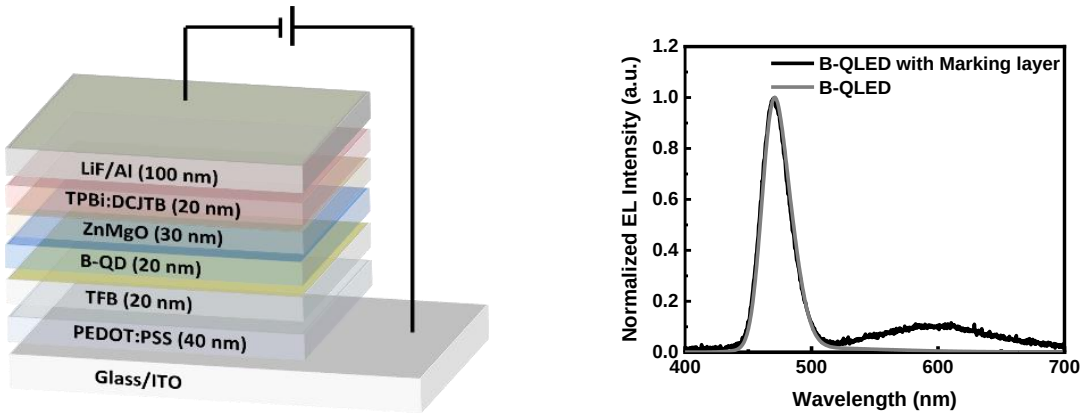

Figure 7.1 a) A schematic diagram of the B-QLEDs with marking layer b) The EL spectra of B-QLED and B-QLED with marking layer collected under 20 mA/cm^2 constant current density driving.

7.1.1 ZnMgO Aging under Electrical Stress

Having verified that holes leak from the B-QD layer and travel through the ZnMgO layer, we proceed to explore the potential impact of these holes within the ZnMgO layer during device operation. For that purpose, we propose two electron-rich and hole-rich device structures in which the ZnMgO layer is dominantly subjected to either electrons or holes current flow under bias while maintaining high similarities. To monitor the possible changes, a comparison between the PL spectra of the pristine and electrically aged devices is used.

Figure 7.2a and **b** show schematic diagrams for the electron-rich (ITO (100 nm)/ZnO (sol-gel)(50 nm)/ZnMgO (60 nm)/CBP (30 nm)/LiF (1 nm)/Al (100 nm)) and hole-rich (ITO (100 nm)/ZnO (sol-gel)(50 nm)/ZnMgO (60 nm)/CBP (30 nm)/MoO_3 (5 nm)/Al (100 nm)) devices, respectively. The ZnO (sol-gel) film serves as a robust and conformal layer, effectively preventing possible shunts between ITO and ZnMgO NPs in both devices. It also serves as a spacer to reduce the PL quenching effect of ITO to ZnMgO that enables observing the PL from the latter. Similarly, 4,4′-Bis(N-carbazolyl)-1,1′-biphenyl (CBP) is used to protect the ZnMgO layer against the PL quenching effect induced by ionic compounds like LiF or MoO_3 due to the strong tendency of metal diffusion[118, 134], enabling a more precise study of potential changes in the ZnMgO layer's PL spectra. CBP is selected

because of its bipolar characteristics, possessing the capability to transport both electrons and holes. This attribute provides us the flexibility to employ CBP in both electron-rich and hole-rich structures [135]. In the electron-rich device, LiF is employed to impede hole injection from the top contact, ensuring the electron-rich nature of the current. Conversely, in the hole-rich structure, MoO_3 serves as the hole injection layer, facilitating effective hole injection. The devices are aged for 24 hours under the shown bias direction with Al at a more positive potential relative to ITO under 20 mA/cm^2 constant current density driving.

Figures 7.2c and **d** show PL spectra collected from the pristine and aged devices with electron-rich and hole-rich structures, respectively. The inset in both cases presents the PL spectrum of CBP single film. All the spectra are collected under 330 nm excitation. As can be seen, the PL spectra of the electron-rich device resemble the CBP PL emission, having a broadband peak at 397 nm. Comparing the PL spectra of the pristine and aged electron-rich devices shows no notable changes, indicating that the flow of electrons does not alter the ZnMgO layer. However, the PL spectra of the hole-rich devices show the presence of a broad emission band spanning from 400-700 nm after aging. This band can be attributed to emission from sub-bandgap defect states in ZnMgO[110, 112]. The results show that the ZnMgO layer is affected by the flow of holes, leading to the development of defects in the ZnMgO layer after aging.

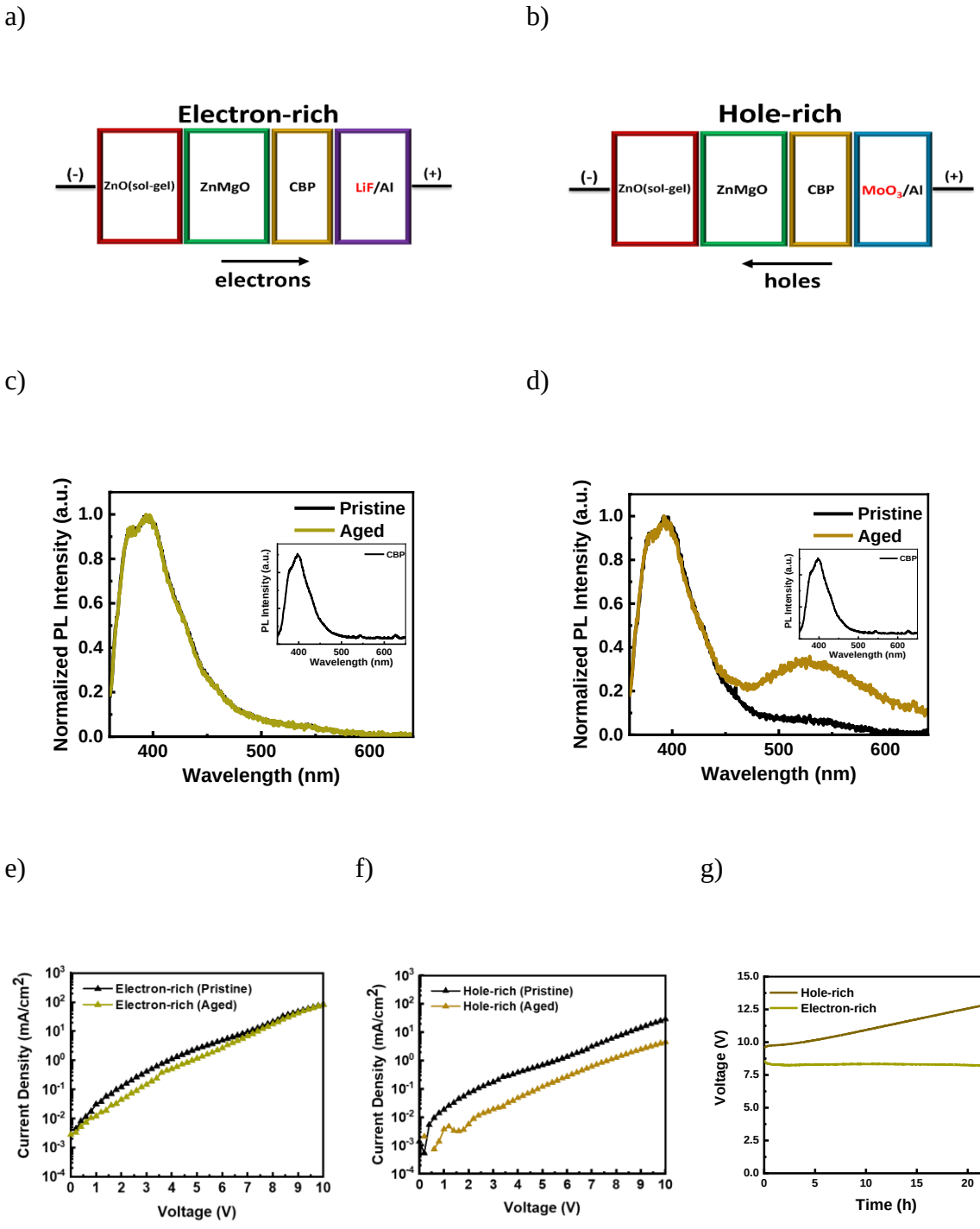

Figure 7.2 Schematic diagram of a) the electron-rich device, and b) the hole-rich device. PL spectra of the pristine and the aged c) electron-rich device, d) hole-rich device. J-V characteristics of the pristine and the aged

e) electron-rich device, f) hole-rich device. g) Voltage vs. time characteristics of electron-rich and hole-rich devices during electrical aging. The aging is conducted under 20 mA/cm^2 constant current density driving for 24 hours.

In addition to the PL spectral measurements, the electrical characteristics of the devices are also studied. **Figures 7.2e** and **f** show the J-V characteristics of electron-rich and hole-rich devices, respectively, for the pristine and aged cases. In **Figure 7.2g**, the voltage versus time (V-t) characteristics of the devices under 20 mA/cm^2 constant current density driving are presented. Once more, the J-V and V-t characteristics for the electron-rich devices show that electrons have little effect on ZnMgO as the J-V and V-t show negligible changes. On the other hand, in the hole-rich devices, the current at any given voltage in the J-V plot decreases considerably after aging whereas the V-t plot shows an increase in voltage, both pointing to a decrease in conduction. Considering the preceding PL spectra, these results imply that the ZnMgO layer changes under hole current, progressively accumulating defects. As a result, the generated defect states can trap charges and affect the transport properties.

So far, our investigations have revealed that the upright B-QLEDs suffer from hole leakage into the ZnMgO layer. We have also found that the leaked holes can negatively impact the ZnMgO layer, possibly inducing new sub-band gap defect states. Based on the findings above, we design an experiment to identify how the changes in the ZnMgO layer may influence QLED performance. In particular, we fabricate inverted QLEDs in which a pre-aged ZnMgO layer under a dominant electron or hole current flow is utilized as ETL. In this approach, device structures similar to hole-rich and electron-rich devices are used to age the ZnMgO layer, except for the ZnO(sol-gel) layer, as there is no ITO PL quenching concern. Following the aging process, the layers above ZnMgO are removed using scotch tape and the samples are prepared for making a QLED. Considering the nature of the experiment involving the ZnMgO layer aging process and using it in a new device, the QLED structure has to be inverted with the ETL coated as the first layer on ITO. Since inverted B-QLEDs tend to have very low efficiency in general, we use G-QDs in these inverted QLEDs.

7.1.2 Inverted G-QLEDs using the Pre-Aged ZnMgO Layer

To further assure the removal of the layers above the ZnMgO, after the tape peel-off, the samples are washed with octane, the same solvent used in the QDs solution, which is also effective in dissolving CBP to ensure the surface is free from any residual organic material. The peel-off procedure and the inverted G-QLED structure are shown in **Figure 7.3a**. The inverted G-QLED is fabricated using the

structure of ITO(100 nm)/ZnMgO(60 nm)/G-QDs(20 nm)/CBP(60 nm)/MoO_3(5 nm)/Al (100 nm). A group of 6 devices of the same structure are tested each time. For comparison, we also fabricate devices using a ZnMgO layer that has been placed in hole-rich devices but not subjected to electrical aging but subjected to CBP coating and removal to act as a reference.

a)

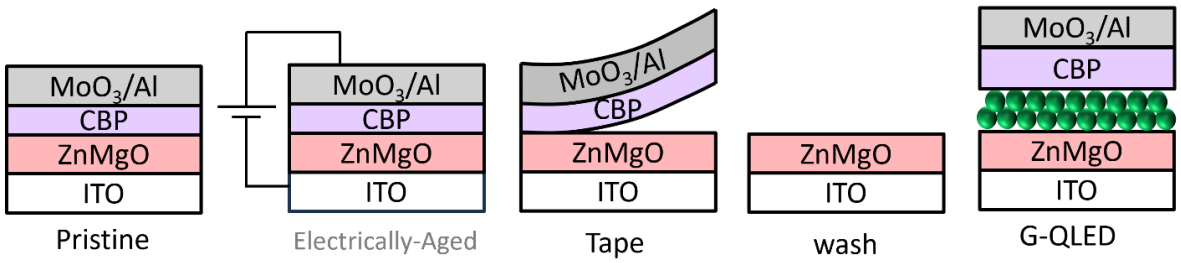

b) c) d)

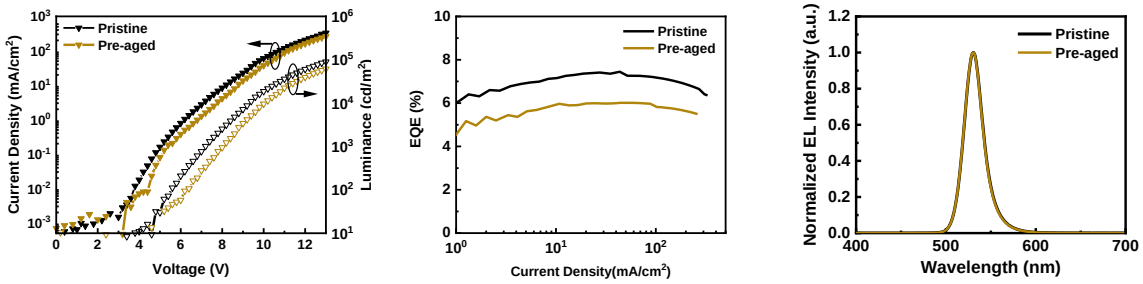

Figure 7.3 a) Schematic of aging ZnMgO in a hole-rich device and peel-off experiments and the subsequently fabricated inverted G-QLED structure b) The J-V-L characteristics of the G-QLED c) The EQE-J characteristics of the G-QLEDs d) The EL spectra of the G-QLEDs using pristine and pre-aged ZnMgO layer under hole-rich current flow. The EL spectra are collected under 20 mA/cm^2 constant current density driving.

Figure 7.3b shows the J-V-L characteristics of inverted G-QLEDs fabricated using pristine and previously aged (pre-aged) ZnMgO layer in hole-rich devices. The results show that the current density of the devices with the aged ZnMgO layer is to some extent lower than the pristine control device at any driving voltage, specifically at lower voltages, and that the threshold voltage (V_{th}) is somewhat high. Since the only difference between the two cases is the ZnMgO layer being subjected to hole-rich current flow before the QLED fabrication, we can attribute the changes to the effect of holes on the ZnMgO layer. The relatively higher voltage and lower current density, especially at lower voltages,

suggest the differences may be due to electron injection properties between the two ETLs. Thus, the results suggest that holes can degrade the ZnMgO layer and negatively affect its ability for electron injection. **Figure 7.3c** shows the external quantum efficiency (EQE) versus current density (EQE-J) characteristics of these devices. The results show a 20% reduction in the maximum EQE of the QLEDs using the aged ZnMgO layer compared to the pristine one (from 7.4 % to 6.0 %). Given the J-V-L characteristics, the inferior electron injection property in the aged ZnMgO layer can, at least in part, contribute to the lower EQE of the G-QLEDs. The EL spectra of the devices are presented in **Figure 7.3d**. The spectra show a single emission band at 530 nm, indicating that the majority of electron-hole recombination occurs in the QD layer for both cases.

To further verify whether the type of carriers indeed matters in ZnMgO degradation, we also age the ZnMgO layer under electron-rich current flow and subsequently use it in an inverted G-QLED. **Figure 7.4a** depicts the procedure starting with aging the ZnMgO layer in an electron-rich device and the subsequent peel-off of the top layers until the final step of G-QLED fabrication. As before, an identical set of devices was fabricated using ZnMgO that was left unaged. As before, an identical set of devices was fabricated using ZnMgO that was left unaged. **Figure 7.4b** shows the J-V-L characteristics of G-QLEDs with pristine and aged ZnMgO layer. As can be seen, there are very negligible variations between the devices in this case, showing that electrons have negligible effect on ZnMgO. The EQE-J characteristics of the QLEDs in **Figure 7.4c** show a maximum EQE of almost 7% for both devices. **Figure 7.4d** depicts the EL spectra of the devices with a single peak emission at 530 nm.

a)

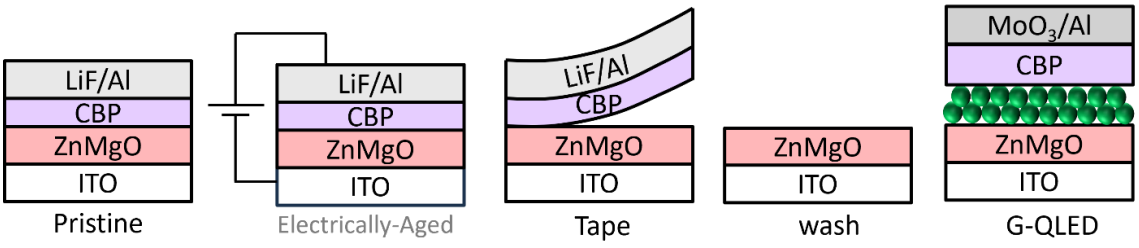

b) c) d)

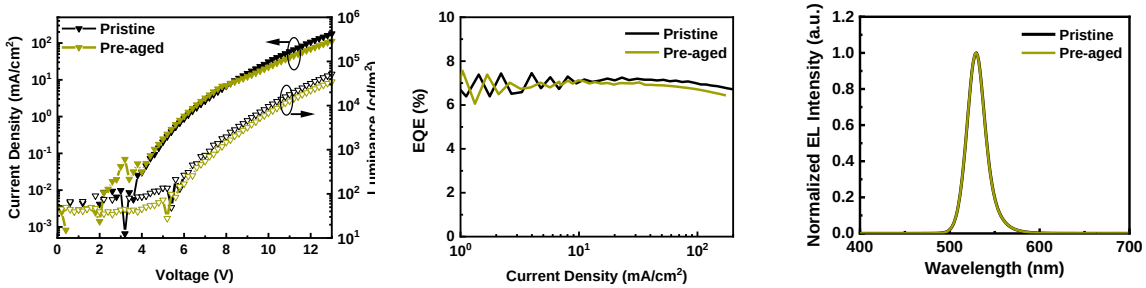

Figure 7.4 a) Schematic of aging ZnMgO in an electron-rich device and peel-off experiments and the subsequently fabricated inverted G-QLED structure b) The J-V-L characteristics of the G-QLED c) The EQE-J characteristics of the G-QLEDs d) The EL spectra of the G-QLEDs using pristine and pre-aged ZnMgO layer under electron-rich current flow. The EL spectra are collected under 20 mA/cm^2 constant current density driving.

7.1.3 The PL Properties of the Inverted QLEDs

To obtain a deeper insight into the damage induced by holes in the ZnMgO layer and its consequential impact on QLEDs efficiency, we also test the PL properties of the fabricated G-QLEDs. **Figure 7.5a** and **b** show the PL spectra of the G-QLEDs discussed above in **Figures 7.3a** and **4a**, compared to their control cases, respectively. All the spectra are collected under 330 nm excitation.

As can be seen, in **Figures 7.5a** and **b**, the PL spectra of the G-QLEDs exhibit a broadband emission ranging from 350-500 nm that corresponds to CBP, along with a narrow emission peak at 526 nm for the G-QDs, respectively. Remarkably, while the normalized spectra show essentially identical spectra for the devices with the pre-aged versus pristine in the case of electron-rich current flow. A significant decrease (~25%) in PL relative intensity is observed in the case of the devices containing ZnMgO exposed to hole-rich current flow. The lower PL intensity points to increased quenching which indicates that the ZnMgO aged under hole-rich current shows a strong quenching effect on the adjacent QD layer.

To investigate if the hole stress of ZnMgO would lead to a similar quenching effect on B-QDs, similar experiments using B-QD are conducted. Since the efficiency of the inverted B-QLEDs is very low, measuring EL properties is not beneficial. Therefore, PL measurements are conducted on the final devices. The results are shown in **Figures S7.1a** and **b**. As can be seen, here again, the intensity of PL for the QDs is much lower in devices with ZnMgO aged under hole-rich current, but not in those aged

under electron-rich current; confirming that the leakage of holes to ZnMgO will degrade the ZnMgO and subsequently negatively affect the output performance of B-QLEDs.

Considering the previously observed sub-bandgap defect states in the degraded ZnMgO layer in hole-rich devices, one can attribute the reduced PLQY of QDs to the defective adjacent ZnMgO layer that leads to exciton quenching in the EML. This phenomenon can also contribute to the lower EQE of the G-QLEDs, as illustrated in **Figure 7.3c**. Hence, the hole-induced degradation in the ZnMgO layer not only reduces the electron injection efficiency in QLEDs but also partially reduces the PLQY of QDs, culminating in a decrease in the device efficiency.

In addition to the steady-state PL spectra, we also study the TRPL characteristics of the G-QLEDs to investigate the exciton decay behavior in QDs adjacent to different ETLs. **Figures 7.5c** and **d** show the TRPL characteristics of the G-QLEDs, discussed above, with the ZnMgO layer already aged under electron-rich or hole-rich current flow, respectively compared to their controls. Again, an identical set of similar samples using B-QDs are fabricated, and their TRPL spectra are presented in **Figures S7.1c** and **d**, providing additional confirmation of optical changes in the case of B-QLEDs. The corresponding TRPL characteristics of similar devices with B-QDs are also presented in the insets. The TRPL characteristics are collected at 526 nm for G-QLEDs and at 467 nm for B-QLEDs, i.e. the QDs PL emission, under a 380 nm excitation peak using a pulsed laser.

The TRPL decay characteristics of the G-QLEDs are fitted using a biexponential function ($y = y_0 + A_1 e^{-t/\tau_1} + A_2 e^{-t/\tau_2}$), and the extracted parameters are presented in **Table 7.1**. In general, the exciton lifetime depends on the rate constants of the radiative and nonradiative recombination, K_r and K_{nr}, respectively; following the relationship: $\tau = \frac{1}{K_r + K_{nr}}$. Since the QDs and the device structure are the same between the pristine and aged scenarios in each case, the K_r is expected to be the same and the differences appear in K_{nr}. In general, fast nonradiative processes such as Auger recombination through the intermediate trap states or defect states in the ETLs can affect the τ_1 component. Comparing the τ_1 component between the G-QLEDs including the pristine or pre-aged ZnMgO layer under electron current in **Figure 7.5c** shows minimal changes. Whereas in **Figure 7.5d**, the G-QLED with aged ETL under hole current shows a shorter exciton lifetime relative to its control. The TRPL decay curves of the B-QLEDs in the inset also show similar behavior.

Therefore, the PL spectra and TRPL characteristics of both G- and B-QLEDs using both electron-rich or hole-rich current aging scenarios used for the ZnMgO layer, confirm that the presence of holes

in the ZnMgO layer causes changes in it that affect its electrical properties as well as increases quenching of the adjacent QD layer. This degradation results in the QDs lower PLQY and subsequently reduces the device efficiency. The electrons, in contrast, make no significant change to the ZnMgO layer.

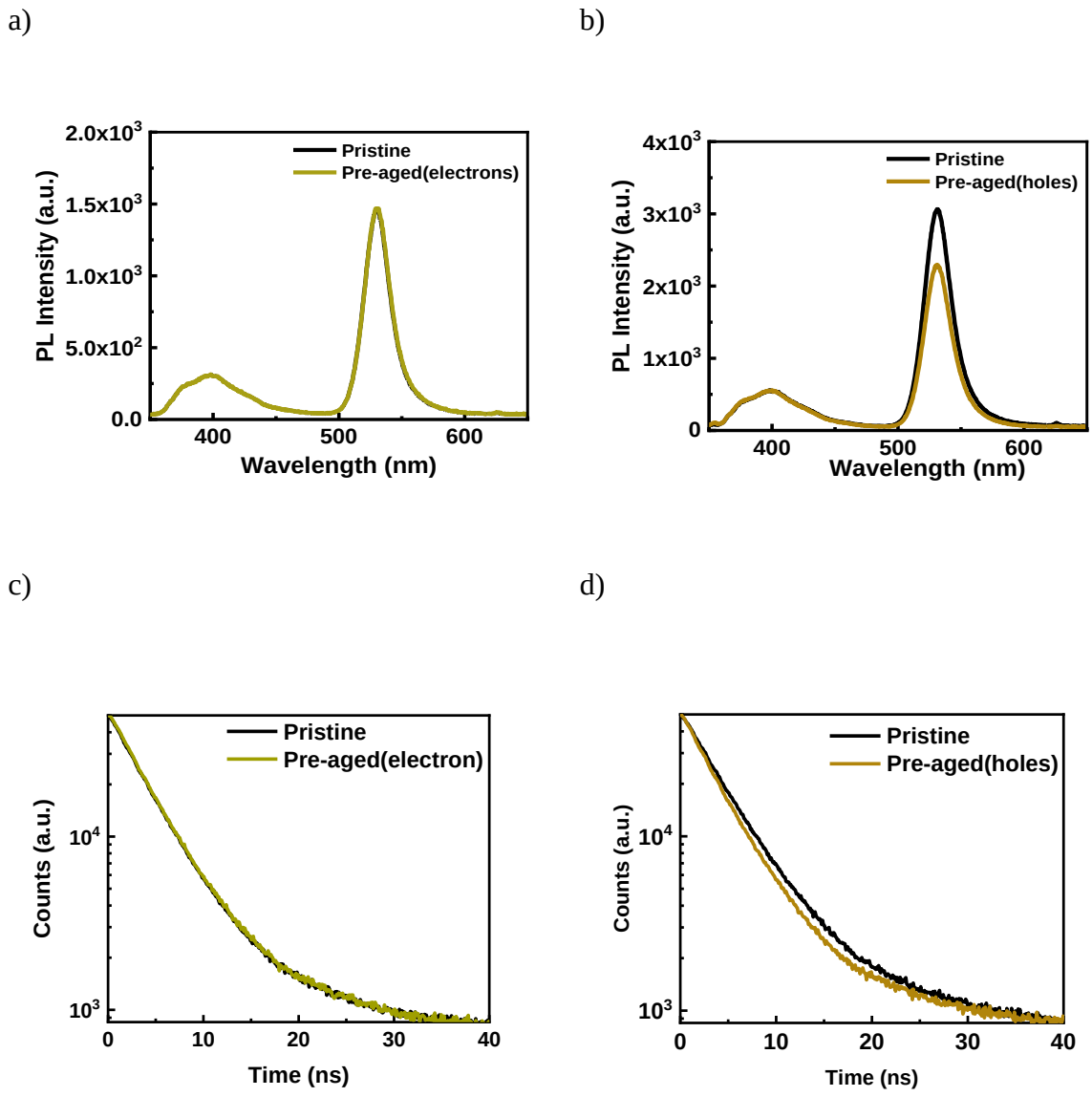

Figure 7.5 The PL spectra of inverted G-QLED using pristine and pre-aged ZnMgO layer a) under electron-rich current flow, b) under hole-rich current flow. The TRPL characteristics of inverted G-QLED using pristine and pre-aged ZnMgO layer c) under electron-rich current flow, d) under hole-rich current flow.

Table 7.1 Exciton lifetimes were found from the bi-exponential fitting of the TRPL curves.

Device	τ_1	τ_2	A_1	A_2
Figure 5c-Electrons effect				
Pristine	4.15	35.1	1.01	0.019
Aged	4.16	38	1.03	0.02
Figure 5d-Holes effect				
Pristine	4.5	34.3	1.01	0.02
Aged	3.99	22.7	1.01	0.02

7.1.4 B-QLEDs Aging with Different h/e Ratios

To further examine the impact of holes on the electron injection property of ZnMgO and its subsequent effect on the stability of upright B-QLEDs, we conduct a comparative measurement of two B-QLEDs with different hole-to-electron (h/e) ratios before and after 24 hours of electrical aging. **Figure 7.6a** depicts a schematic diagram illustrating the structure of the hole-rich B-QLED comprising ITO (100 nm)/PEDOT:PSS(40 nm)/TFB(20 nm)/B-QD(20 nm)/ZnMgO(60 nm)/MoO_3(5 nm)/Al(100 nm). The structure is identical to a regular B-QLED except for the incorporation of the MoO_3 electron-blocking layer. This layer serves the purpose of partially impeding electron injection thereby increasing the h/e ratio within the device. For a device with a lower h/e ratio, a regular B-QLED with the structure of ITO (100 nm)/PEDOT:PSS(40 nm)/TFB(20 nm)/B-QD(20 nm)/ZnMgO(60 nm)/ Al(100 nm) is used.

Figure 7.6b shows the J-V-L characteristics of pristine B-QLED and hole-rich B-QLED versus their aged cases. As can be seen, the current density in both cases decreases at any voltage after aging. In our previous work, we established that hole injection is facilitated during the B-QLEDs aging[136]. Since the device current density is composed of both electrons and holes injections into the device, and in the

aged B-QLEDs, hole injection is increased although the total current of the device decreases, one can conclude that the observed decrease in current density can be associated with a decrease in electron injection upon aging.

Moreover, the turn-on voltage, defined as the voltage for the onset of electroluminescence, taken here as reaching an electroluminescence of 20 cd/m^2[125], increases from 2.65 V to 3 V and from 2.8 V to 3.6 V in B-QLED and hole-rich B-QLED, respectively. Since in both devices holes are the majority carriers and are injected first [78-79, 136], the turn-on voltage for efficient radiative exciton recombination is constrained by the onset of electron injection into the B-QDs EML. The increase in turn-on voltage implies that electron injection becomes less efficient, requiring a higher voltage. As the h/e ratio increases, e.g., in hole-rich B-QLED, a larger increase in the turn-on voltage is observed. Therefore, the decreased electron injection efficiency can be ascribed to the role of holes inducing the ZnMgO degradation, where more holes cause greater damage to the electron injection capacity of the ETL, and hence a larger increase in turn-on voltage due to aging.

Turning our attention now to the EL spectra of these devices in **Figure 7.6c**, both the pristine B-QLED and hole-rich B-QLEDs devices emit a single peak at 471 nm corresponding to the emission peak of the B-QDs. The EL spectra of the aged devices however additionally show a prominent blue peak at 476 nm with a broad emission band ranging from 400-700 nm that corresponds to the emission from the ZnMgO layer sub-bandgap defect states. The emission band originating from the ZnMgO layer is more significant in hole-rich B-QLED where the h/e ratio is larger. The recombination zone shift toward the ETL after aging is consistent with electron injection becoming less efficient after aging. This substantiates the critical role of holes in the ZnMgO degradation, ultimately leading to a lower electron injection efficiency.

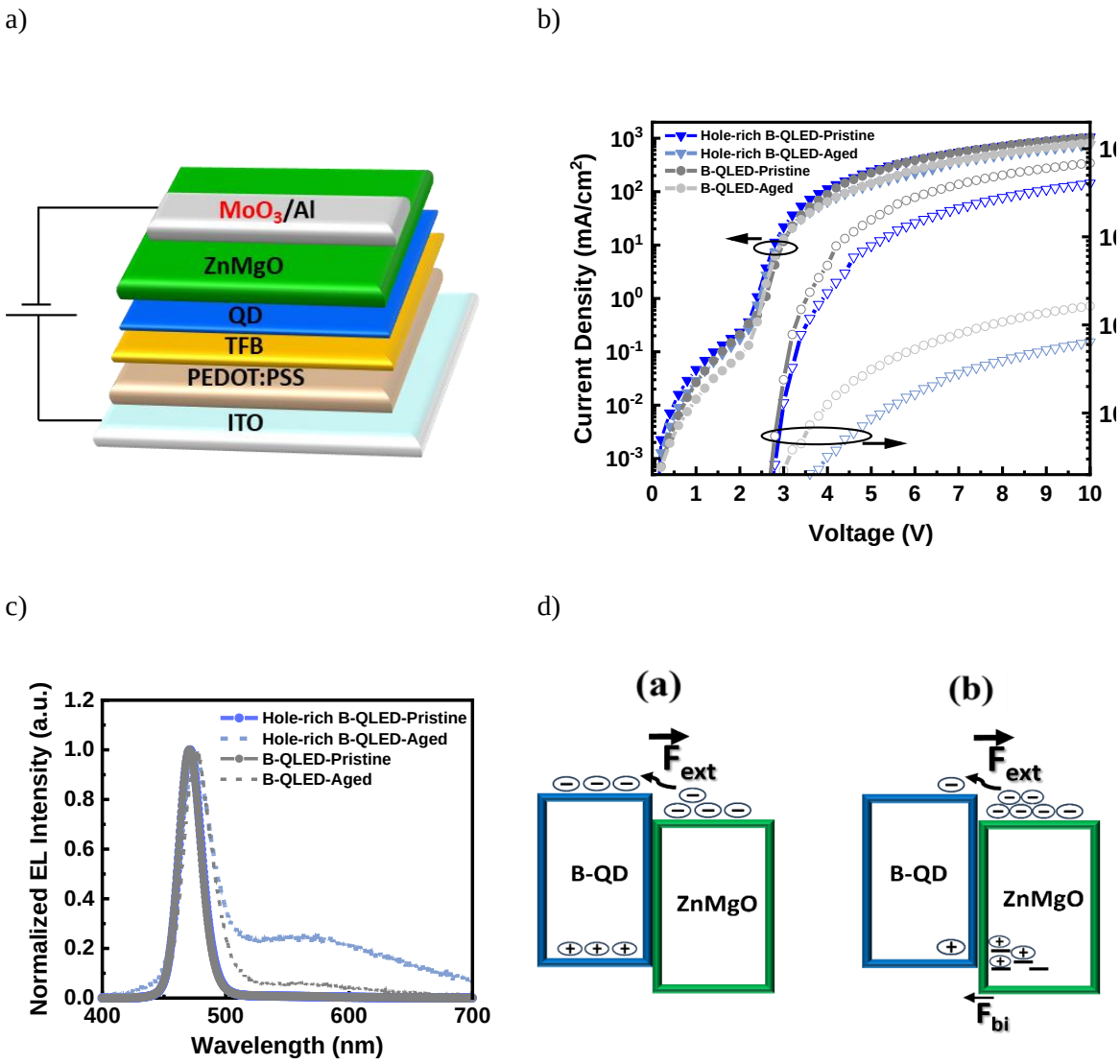

Figure 7.6 a) A schematic diagram of a hole-rich B-QLED. b) The J-V-L characteristics of regular and hole-rich B-QLEDs before and after aging. c) The EL characteristics of regular and hole-rich B-QLEDs before and after aging. The aging is conducted under 20 mA/cm^2 constant current density driving for 24 hours. d) A schematic explaining the electron injection deterioration induced by holes in the ZnMgO layer.

To elucidate the mechanism behind the hole-induced ZnMgO aging, resulting in an inferior charge balance in B-QLEDs, **Figure 7.6d** presents a schematic that speculates the potential processes leading to decreased electron injection**.** The figure shows B-QDs EML adjacent to the ZnMgO ETL,

representing the initial pristine case and after aging in (a) and (b), respectively. In the pristine case, the external electric field drives the electrons to overcome the injection energy barrier to get injected into the B-QDs layer. According to the PL results of electron-rich and hole-rich devices discussed earlier, the leaked holes from the B-QDs into the ZnMgO lead to sub-bandgap defect states, a similar phenomenon reported for ZnO in inverted red QLEDs[97]. As the holes, i.e. positive charges, penetrate into the ZnMgO layer, they can get trapped in some of these defect states, thereby establishing a built-in electric field against the external field. Consequently, the net force for injecting electrons is reduced. In addition, the generated defects in the ETL can scatter the electrons affecting the electron mobility[137]. Also, the positively charged trapes can neutralize the intrinsic electrons leading to a reduced number of carriers in the ETL. Besides that, these traps can further influence the efficiency and stability of B-QLEDs by inducing exciton quenching in the neighboring B-QDs layer. Therefore, the hole-induced damage in the ZnMgO layer can reduce electron injection efficiency into the B-QDs layer.

7.2 Conclusions

In summary, the findings of this chapter shed light on a key contributing factor to the limited EL stability of upright B-QLEDs. The study reveals hole leakage into the ZnMgO layer in B-QLEDs is a critical issue, leading to subsequent degradation of ETL. Optical and electrical studies are carried out on the ZnMgO layer subjected to electrical aging under both electron-rich and hole-rich current flow scenarios. The steady-state PL results coupled with TRPL characteristics of the inverted G-QLED fabricated using the pre-aged ZnMgO layer show that holes are detrimental to the ZnMgO layer by inducing defects. Conversely, electrons are found to have a limited impact on the ZnMgO layer. In addition, the J-V-L characteristics of B-QLEDs with different h/e ratios emphasize that increased penetration of holes into the ZnMgO layer exacerbates the degradation of the ETL's electron injection property, disrupting the charge balance in B-QLEDs. Our findings uncover the critical role of leaked holes in upright B-QLEDs on the ZnMgO degradation and highlight the significance of achieving optimal charge balance and carrier confinement in B-QLEDs for the development of highly stable devices toward QLEDs commercialization.

Chapter 8

Summary and Future Work

8.1 Summary of Main Conclusions

This section summarizes the main findings of this work. The fundamental objective of this research was to identify the underlying causes for poor EL stability of B-QLEDs that were categorized into three main routes: (i) studying the B-QDs' PLQY shelf life in different scenarios (ii) studying the B-QDs' PLQY under electrical stress (iii) exploring different potential factors contributing to the B-QLEDs' EL stability such as charge imbalance or CTLs degradation.

Chapter 4: studying the B-QDs PLQY stability without bias:

- The results indicated that B-QDs PLQY were intrinsically stable over time in storage provided that the film is protected from ambient species.
- B-QDs showed stable PLQY in contact with the HTL.
- ZnMgO showed a significant quenching effect on B-QDs PLQY due to the morphological changes leading to higher roughness and the diffusion of some spices like Li or Mg.

Chapter 5: Studying the B-QDs PLQY stability under electrical stress:

- The results of EODs showed that B-QDs' PLQY is stable over time and after being subjected to electron current flow.
- The HODs using TFB exhibited degradation when subjected to hole current flow.
- Replacing the TFB with VB-FNPD showed stable PL spectra in HODs but no change in the electrical stability of B-QLEDs.
- Replacing the TFB with VB-FNPD in upright G-QLEDs enhanced their electrical stability by two times.

Chapter 6: Studying the electrical characteristics of single-carrier devices:

- The charge balance deteriorated over time in B-QLEDs under electrical stress. Hole injection into B-QDs was shown to increase and electron injection to decrease over time.
- The charge injection change was observed to be partially reversible and resulted in improved EL stability of B-QLEDs if aged under pulsed current bias instead of constant continuous current.

Chapter 7: Studying the ZnMgO layer degradation in B-QLEDs:

- B-QLEDs suffer from holes leaking into the ZnMgO layer that induces ETL degradation under bias.
- The ZnMgO layer contains more sub-bandgap defect states after being subjected to hole-rich current flow.
- The ZnMgO layer showed minimal change when subjected to electron-rich current flow.
- The hole-induced degradation in the ZnMgO layer results in reduced electron injection capacity of the ZnMgO layer, resulting in charge imbalance in B-QLEDs.

8.2 Future Work

This section outlines suggestions for future research based on the conclusions and major findings of this work.

First, this work has revealed that the inorganic metal oxide ZnMgO ETL leads to PLQY loss for B-QDs due to morphology changes over time or the diffusion of some species from the ETL into the QD layer. Therefore, the commonly used ZnMgO ETL can negatively affect the shelf life of the B-QLEDs. It is essential for QLEDs commercialization to find alternative solutions to achieve reliable B-QLEDs with high EL stability. Therefore, there is a space for future studies to design new ETLs with high morphological stability and well-matched energy levels with B-QDs. For example, SnO_2 is found to work well as the ETL in perovskite devices exhibiting high stability[138].

Moreover, a comprehensive study needs to be done on the influence of encapsulation and the exact mechanism of its effects on B-QLEDs.

In addition, the findings indicated that the EL degradation in B-QLEDs is partially reversible, and using pulsed current instead of continuous constant current enhanced the devices' EL stability. Therefore, using alternating current (AC) instead of direct current (DC) can be promising to achieve higher EL stabilities for QLEDs. Using an AC drive is an interesting potential alternative for a DC drive in QLEDs due to the great advantage of easy integration with AC power system without complicated back-end electronics. The AC driving can be advantageous to retard the degradation mechanism in QLEDs possibly by neutralizing the accumulated charges in the device or making charge relaxations and detrapping in the negative half-cycles.

Furthermore, the results show that CdSe-based B-QLEDs EL loss causes are more complex than other color counterparts despite their similarities in the chemical compounds. In addition, it is found that charge injection efficiency into B-QDs changes over time under bias. Considering that B-QDs possess different organic ligands compared to R- and G-QDs, the role of ligands in charge injection into the QDs and their electrochemical stability is important and might be playing a role in B-QLEDs EL stability. Therefore, future studies can be dedicated to the role of different ligands with various functional groups, and different carbon chain lengths and see how each of these factors can affect the shelf life or the electrical stability of the QLEDs. These studies can give deeper insights to engineer the QDs design for obtaining higher EL stability of QLEDs toward the QLEDs commercialization.

References

1. Heilmeier, G. H.; Zanoni, L. A.; Barton, L. A., Dynamic scattering: A new electrooptic effect in certain classes of nematic liquid crystals. *Proceedings of the IEEE* **1968,** *56* (7), 1162-1171.
2. Huang, Y.; Hsiang, E.-L.; Deng, M.-Y.; Wu, S.-T., Mini-LED, Micro-LED and OLED displays: present status and future perspectives. *Light: Science & Applications* **2020,** *9* (1), 105.
3. Tang, C. W.; VanSlyke, S. A., Organic electroluminescent diodes. *Applied physics letters* **1987,** *51* (12), 913-915.
4. Jang, E.; Jang, H., Quantum Dot Light-Emitting Diodes. *Chemical Reviews* **2023,** *123* (8), 4663-4692.
5. Rossetti, R.; Nakahara, S.; Brus, L. E., Quantum size effects in the redox potentials, resonance Raman spectra, and electronic spectra of CdS crystallites in aqueous solution. *The Journal of Chemical Physics* **1983,** *79* (2), 1086-1088.
6. Ekimov, A. I.; Efros, A. L.; Onushchenko, A. A., Quantum size effect in semiconductor microcrystals. *Solid State Communications* **1985,** *56* (11), 921-924.
7. Shirasaki, Y.; Supran, G. J.; Bawendi, M. G.; Bulović, V., Emergence of colloidal quantum-dot light-emitting technologies. *Nature photonics* **2013,** *7* (1), 13-23.
8. Tian, D.; Ma, H.; Huang, G.; Gao, M.; Cai, F.; Fang, Y.; Li, C.; Jiang, X.; Wang, A.; Wang, S., A Review on Quantum Dot Light-Emitting Diodes: From Materials to Applications. *Advanced Optical Materials* **2023,** *11* (2), 2201965.
9. Wood, V.; Bulović, V., Colloidal quantum dot light-emitting devices. *Nano reviews* **2010,** *1* (1), 5202.
10. Colvin, V. L.; Schlamp, M. C.; Alivisatos, A. P., Light-emitting diodes made from cadmium selenide nanocrystals and a semiconducting polymer. *Nature* **1994,** *370* (6488), 354-357.
11. Dabbousi, B.; Bawendi, M.; Onitsuka, O.; Rubner, M., Electroluminescence from CdSe quantum-dot/polymer composites. *Applied Physics Letters* **1995,** *66* (11), 1316-1318.
12. Deng, Y.; Peng, F.; Lu, Y.; Zhu, X.; Jin, W.; Qiu, J.; Dong, J.; Hao, Y.; Di, D.; Gao, Y., Solution-processed green and blue quantum-dot light-emitting diodes with eliminated charge leakage. *Nature Photonics* **2022,** *16* (7), 505-511.
13. Fang, Y.; Bai, P.; Li, J.; Xiao, B.; Wang, Y.; Wang, Y., Highly efficient red quantum dot light-emitting diodes by balancing charge injection and transport. *ACS Applied Materials & Interfaces* **2022,** *14* (18), 21263-21269.
14. Hanson, G. W., *Fundamentals of nanoelectronics*. Pearson Education: 2008; p 280-314.
15. Pietryga, J. M.; Park, Y.-S.; Lim, J.; Fidler, A. F.; Bae, W. K.; Brovelli, S.; Klimov, V. I., Spectroscopic and device aspects of nanocrystal quantum dots. *Chemical reviews* **2016,** *116* (18), 10513-10622.
16. Marnocha, J., Effect of Wannier-Mott Exciton on Semiconductor Quantum Dot Photo-Absorption Spectra. **2017**.
17. Li, S.-N.; Pan, J.-L.; Yu, Y.-J.; Zhao, F.; Wang, Y.-K.; Liao, L.-S., Advances in Solution-Processed Blue Quantum Dot Light-Emitting Diodes. *Nanomaterials* **2023,** *13* (10), 1695.
18. Kim, J.; Roh, J.; Park, M.; Lee, C., Recent Advances and Challenges of Colloidal Quantum Dot Light-Emitting Diodes for Display Applications. *Advanced Materials* **2023**, 2212220.
19. García de Arquer, F. P.; Talapin, D. V.; Klimov, V. I.; Arakawa, Y.; Bayer, M.; Sargent, E. H., Semiconductor quantum dots: Technological progress and future challenges. *Science* **2021,** *373* (6555), eaaz8541.

20. Osypiw, A. R.; Lee, S.; Jung, S.-M.; Leoni, S.; Smowton, P. M.; Hou, B.; Kim, J. M.; Amaratunga, G. A., Solution-processed colloidal quantum dots for light emission. *Materials Advances* **2022,** *3* (17), 6773-6790.
21. Rodrigues, S. S. M.; Ribeiro, D. S.; Soares, J. X.; Passos, M. L.; Saraiva, M. L. M.; Santos, J. L., Application of nanocrystalline CdTe quantum dots in chemical analysis: Implementation of chemo-sensing schemes based on analyte-triggered photoluminescence modulation. *Coordination Chemistry Reviews* **2017,** *330*, 127-143.
22. Blachowicz, T.; Ehrmann, A., Recent developments of solar cells from PbS colloidal quantum dots. *Applied Sciences* **2020,** *10* (5), 1743.
23. Chinnathambi, S.; Chen, S.; Ganesan, S.; Hanagata, N., Silicon quantum dots for biological applications. *Advanced healthcare materials* **2014,** *3* (1), 10-29.
24. Riehle, F. S.; Bienert, R.; Thomann, R.; Urban, G. A.; Krüger, M., Blue luminescence and superstructures from magic size clusters of CdSe. *Nano letters* **2009,** *9* (2), 514-518.
25. Díaz-González, M.; de la Escosura-Muñiz, A.; Fernandez-Argüelles, M. T.; Alonso, F. J. G.; Costa-Fernandez, J. M., Quantum dot bioconjugates for diagnostic applications. *Surface-modified nanobiomaterials for electrochemical and biomedicine applications* **2020**, 133-176.
26. Moon, H.; Lee, C.; Lee, W.; Kim, J.; Chae, H., Stability of quantum dots, quantum dot films, and quantum dot light-emitting diodes for display applications. *Advanced Materials* **2019,** *31* (34), 1804294.
27. Qi, H.; Wang, S.; Jiang, X.; Fang, Y.; Wang, A.; Shen, H.; Du, Z., Research progress and challenges of blue light-emitting diodes based on II–VI semiconductor quantum dots. *Journal of Materials Chemistry C* **2020,** *8* (30), 10160-10173.
28. Jia, H.; Wang, F.; Tan, Z. a., Material and device engineering for high-performance blue quantum dot light-emitting diodes. *Nanoscale* **2020,** *12* (25), 13186-13224.
29. Chen, Z.; Li, H.; Yuan, C.; Gao, P.; Su, Q.; Chen, S., Color Revolution: Prospects and Challenges of Quantum-Dot Light-Emitting Diode Display Technologies. *Small Methods* **2023**, 2300359.
30. Yuan, Q.; Wang, T.; Yu, P.; Zhang, H.; Zhang, H.; Ji, W., A review on the electroluminescence properties of quantum-dot light-emitting diodes. *Organic Electronics* **2021,** *90*, 106086.
31. Yang, Z.; Gao, M.; Wu, W.; Yang, X.; Sun, X. W.; Zhang, J.; Wang, H.-C.; Liu, R.-S.; Han, C.-Y.; Yang, H., Recent advances in quantum dot-based light-emitting devices: Challenges and possible solutions. *Materials Today* **2019,** *24*, 69-93.
32. Dai, X.; Deng, Y.; Peng, X.; Jin, Y., Quantum-dot light-emitting diodes for large-area displays: towards the dawn of commercialization. *Advanced materials* **2017,** *29* (14), 1607022.
33. Coe, S.; Woo, W.-K.; Bawendi, M.; Bulović, V., Electroluminescence from single monolayers of nanocrystals in molecular organic devices. *Nature* **2002,** *420* (6917), 800-803.
34. Caruge, J.; Halpert, J. E.; Wood, V.; Bulović, V.; Bawendi, M., Colloidal quantum-dot light-emitting diodes with metal-oxide charge transport layers. *Nature photonics* **2008,** *2* (4), 247-250.
35. Qian, L.; Zheng, Y.; Xue, J.; Holloway, P. H., Stable and efficient quantum-dot light-emitting diodes based on solution-processed multilayer structures. *Nature photonics* **2011,** *5* (9), 543-548.
36. Chen, F.; Lin, Q.; Shen, H.; Tang, A., Blue quantum dot-based electroluminescent light-emitting diodes. *Materials Chemistry Frontiers* **2020,** *4* (5), 1340-1365.
37. Bae, W. K.; Park, Y.-S.; Lim, J.; Lee, D.; Padilha, L. A.; McDaniel, H.; Robel, I.; Lee, C.; Pietryga, J. M.; Klimov, V. I., Controlling the influence of Auger recombination on the performance of quantum-dot light-emitting diodes. *Nature communications* **2013,** *4* (1), 2661.

38. Brown, P. R.; Kim, D.; Lunt, R. R.; Zhao, N.; Bawendi, M. G.; Grossman, J. C.; Bulovic, V., Energy level modification in lead sulfide quantum dot thin films through ligand exchange. *ACS nano* **2014,** *8* (6), 5863-5872.
39. Li, X.; Zhao, Y.-B.; Fan, F.; Levina, L.; Liu, M.; Quintero-Bermudez, R.; Gong, X.; Quan, L. N.; Fan, J.; Yang, Z., Bright colloidal quantum dot light-emitting diodes enabled by efficient chlorination. *Nature Photonics* **2018,** *12* (3), 159-164.
40. Davidson-Hall, T.; Aziz, H., Significant enhancement in quantum dot light-emitting device stability via a cascading hole transport layer. *ACS applied materials & interfaces* **2020,** *12* (14), 16782-16791.
41. Chao, W.-C.; Chiang, T.-H.; Liu, Y.-C.; Huang, Z.-X.; Liao, C.-C.; Chu, C.-H.; Wang, C.-H.; Tseng, H.-W.; Hung, W.-Y.; Chou, P.-T., High efficiency green InP quantum dot light-emitting diodes by balancing electron and hole mobility. *Communications Materials* **2021,** *2* (1), 96.
42. Cao, F.; Zhao, D.; Shen, P.; Wu, J.; Wang, H.; Wu, Q.; Wang, F.; Yang, X., High-efficiency, solution-processed white quantum dot light-emitting diodes with serially stacked red/green/blue units. *Advanced Optical Materials* **2018,** *6* (20), 1800652.
43. Sun, Y.; Jiang, Y.; Sun, X. W.; Zhang, S.; Chen, S., Beyond OLED: efficient quantum dot light-emitting diodes for display and lighting application. *The Chemical Record* **2019,** *19* (8), 1729-1752.
44. Song, J.; Wang, O.; Shen, H.; Lin, Q.; Li, Z.; Wang, L.; Zhang, X.; Li, L. S., Over 30% external quantum efficiency light-emitting diodes by engineering quantum dot-assisted energy level match for hole transport layer. *Advanced Functional Materials* **2019,** *29* (33), 1808377.
45. Wang, L.; Lin, J.; Hu, Y.; Guo, X.; Lv, Y.; Tang, Z.; Zhao, J.; Fan, Y.; Zhang, N.; Wang, Y., Blue quantum dot light-emitting diodes with high electroluminescent efficiency. *ACS applied materials & interfaces* **2017,** *9* (44), 38755-38760.
46. Li, X.; Lin, Q.; Song, J.; Shen, H.; Zhang, H.; Li, L. S.; Li, X.; Du, Z., Quantum-Dot Light-Emitting Diodes for Outdoor Displays with High Stability at High Brightness. *Advanced Optical Materials* **2020,** *8* (2), 1901145.
47. Kim, T.; Kim, K.-H.; Kim, S.; Choi, S.-M.; Jang, H.; Seo, H.-K.; Lee, H.; Chung, D.-Y.; Jang, E., Efficient and stable blue quantum dot light-emitting diode. *Nature* **2020,** *586* (7829), 385-389.
48. Lee, K.-H.; Lee, J.-H.; Song, W.-S.; Ko, H.; Lee, C.; Lee, J.-H.; Yang, H., Highly efficient, color-pure, color-stable blue quantum dot light-emitting devices. *ACS nano* **2013,** *7* (8), 7295-7302.
49. Lee, T.; Kim, B. J.; Lee, H.; Hahm, D.; Bae, W. K.; Lim, J.; Kwak, J., Bright and Stable Quantum Dot Light-Emitting Diodes. *Advanced Materials* **2022,** *34* (4), 2106276.
50. Chung, D. S.; Davidson-Hall, T.; Cotella, G.; Lyu, Q.; Chun, P.; Aziz, H., Significant Lifetime Enhancement in QLEDs by Reducing Interfacial Charge Accumulation via Fluorine Incorporation in the ZnO Electron Transport Layer. *Nano-Micro Letters* **2022,** *14* (1), 212.
51. Pu, C.; Dai, X.; Shu, Y.; Zhu, M.; Deng, Y.; Jin, Y.; Peng, X., Electrochemically-stable ligands bridge the photoluminescence-electroluminescence gap of quantum dots. *Nature Communications* **2020,** *11* (1), 937.
52. Chen, X.; Lin, X.; Zhou, L.; Sun, X.; Li, R.; Chen, M.; Yang, Y.; Hou, W.; Wu, L.; Cao, W., Blue light-emitting diodes based on colloidal quantum dots with reduced surface-bulk coupling. *Nature Communications* **2023,** *14* (1), 284.
53. Zhang, Z.; Zhang, X.; Liu, H.; Bao, H.; Zhang, F.; Wang, S.; Li, X., Building one-dimensional hole transport channels in cross-linked polymers to enable efficient deep blue QLED. *Chemical Engineering Journal* **2023,** *451*, 138516.

54. Shen, Q.; Hao, Y.; Ma, L.; Wang, X., Comparative study of red/green/blue quantum-dot light-emitting diodes by time-resolved transient electroluminescence. *The Journal of Physical Chemistry Letters* **2021,** *12* (29), 7019-7025.
55. Davidson-Hall, T.; Aziz, H., The role of excitons within the hole transporting layer in quantum dot light emitting device degradation. *Nanoscale* **2019,** *11* (17), 8310-8318.
56. Chang, J. H.; Park, P.; Jung, H.; Jeong, B. G.; Hahm, D.; Nagamine, G.; Ko, J.; Cho, J.; Padilha, L. A.; Lee, D. C., Unraveling the origin of operational instability of quantum dot based light-emitting diodes. *ACS nano* **2018,** *12* (10), 10231-10239.
57. Cordero, S.; Carson, P.; Estabrook, R.; Strouse, G.; Buratto, S., Photo-activated luminescence of CdSe quantum dot monolayers. *The Journal of Physical Chemistry B* **2000,** *104* (51), 12137-12142.
58. Pechstedt, K.; Whittle, T.; Baumberg, J.; Melvin, T., Photoluminescence of colloidal CdSe/ZnS quantum dots: the critical effect of water molecules. *The Journal of Physical Chemistry C* **2010,** *114* (28), 12069-12077.
59. Carrillo-Carrión, C.; Cárdenas, S.; Simonet, B. M.; Valcárcel, M., Quantum dots luminescence enhancement due to illumination with UV/Vis light. *Chemical Communications* **2009,** (35), 5214-5226.
60. Kondakov, D. Y.; Pawlik, T. D.; Nichols, W. F.; Lenhart, W. C., Free-radical pathways in operational degradation of OLEDs. *Journal of the Society for Information Display* **2008,** *16* (1), 37-46.
61. Xue, X.; Dong, J.; Wang, S.; Zhang, H.; Zhang, H.; Zhao, J.; Ji, W., Degradation of quantum dot light emitting diodes, the case under a low driving level. *Journal of Materials Chemistry C* **2020,** *8* (6), 2014-2018.
62. Chen, S.; Cao, W.; Liu, T.; Tsang, S.-W.; Yang, Y.; Yan, X.; Qian, L., On the degradation mechanisms of quantum-dot light-emitting diodes. *Nature Communications* **2019,** *10* (1), 765.
63. Han, M. G.; Lee, Y.; Kwon, H.-i.; Lee, H.; Kim, T.; Won, Y.-H.; Jang, E., InP-based quantum dot light-emitting diode with a blended emissive layer. *ACS Energy Letters* **2021,** *6* (4), 1577-1585.
64. Ye, Y.; Zheng, X.; Chen, D.; Deng, Y.; Chen, D.; Hao, Y.; Dai, X.; Jin, Y., Design of the hole-injection/hole-transport interfaces for stable quantum-dot light-emitting diodes. *The Journal of Physical Chemistry Letters* **2020,** *11* (12), 4649-4654.
65. Liu, Y.; Jiang, C.; Song, C.; Wang, J.; Mu, L.; He, Z.; Zhong, Z.; Cun, Y.; Mai, C.; Wang, J., Highly efficient all-solution processed inverted quantum dots based light emitting diodes. *ACS nano* **2018,** *12* (2), 1564-1570.
66. Davidson-Hall, T.; Aziz, H., The role of polyethylenimine in enhancing the efficiency of quantum dot light-emitting devices. *Nanoscale* **2018,** *10* (5), 2623-2631.
67. Tang, P.; Xie, L.; Xiong, X.; Wei, C.; Zhao, W.; Chen, M.; Zhuang, J.; Su, W.; Cui, Z., Realizing 22.3% EQE and 7-fold lifetime enhancement in QLEDs via blending polymer TFB and cross-linkable small molecules for a solvent-resistant hole transport layer. *ACS applied materials & interfaces* **2020,** *12* (11), 13087-13095.
68. Zou, Y.; Liu, Y.; Ban, M.; Huang, Q.; Sun, T.; Zhang, Q.; Song, T.; Sun, B., Crosslinked conjugated polymers as hole transport layers in high-performance quantum dot light-emitting diodes. *Nanoscale Horizons* **2017,** *2* (3), 156-162.
69. Sun, W.; Deng, Y.; Jin, Y.; Guo, X.; Zhang, Q., Solvent Resistant Hole-Transporting Thin Films via Diacetylene Cross-Linking and Their Applications in Solution-Processed QLEDs. *ACS Applied Polymer Materials* **2020,** *2* (8), 3274-3281.
70. Lin, B.-Y.; Ding, W.-C.; Chen, C.-H.; Kuo, Y.-P.; Lee, J.-H.; Lee, C.-Y.; Chiu, T.-L., Lifetime elongation of quantum-dot light-emitting diodes by inhibiting the degradation of hole transport layer. *RSC advances* **2021,** *11* (34), 20884-20891.

71. Pan, J.; Chen, J.; Huang, Q.; Khan, Q.; Liu, X.; Tao, Z.; Zhang, Z.; Lei, W.; Nathan, A., Size tunable ZnO nanoparticles to enhance electron injection in solution processed QLEDs. *ACS photonics* **2016,** *3* (2), 215-222.
72. Mashford, B. S.; Stevenson, M.; Popovic, Z.; Hamilton, C.; Zhou, Z.; Breen, C.; Steckel, J.; Bulovic, V.; Bawendi, M.; Coe-Sullivan, S., High-efficiency quantum-dot light-emitting devices with enhanced charge injection. *Nature photonics* **2013,** *7* (5), 407-412.
73. Moon, H.; Lee, W.; Kim, J.; Lee, D.; Cha, S.; Shin, S.; Chae, H., Composition-tailored ZnMgO nanoparticles for electron transport layers of highly efficient and bright InP-based quantum dot light emitting diodes. *Chemical Communications* **2019,** *55* (88), 13299-13302.
74. Kim, J.-H.; Han, C.-Y.; Lee, K.-H.; An, K.-S.; Song, W.; Kim, J.; Oh, M. S.; Do, Y. R.; Yang, H., Performance improvement of quantum dot-light-emitting diodes enabled by an alloyed ZnMgO nanoparticle electron transport layer. *Chemistry of Materials* **2015,** *27* (1), 197-204.
75. Sun, Y.; Jiang, Y.; Peng, H.; Wei, J.; Zhang, S.; Chen, S., Efficient quantum dot light-emitting diodes with a Zn 0.85 Mg 0.15 O interfacial modification layer. *Nanoscale* **2017,** *9* (26), 8962-8969.
76. Vokhmintcev, K. V.; Samokhvalov, P. S.; Nabiev, I., Charge transfer and separation in photoexcited quantum dot-based systems. *Nano Today* **2016,** *11* (2), 189-211.
77. Keating, L. P.; Lee, H.; Rogers, S. P.; Huang, C.; Shim, M., Charging and Charged Species in Quantum Dot Light-Emitting Diodes. *Nano letters* **2022,** *22* (23), 9500-9506.
78. Azadinia, M.; Chun, P.; Lyu, Q.; Cotella, G.; Aziz, H., Differences in Electron and Hole Injection and Auger Recombination between Red, Green, and Blue CdSe-Based Quantum Dot Light Emitting Devices. *ACS nano* **2024,** *18* (2), 1485-1495.
79. Azadinia, M.; Davidson-Hall, T.; Chung, D. S.; Ghorbani, A.; Samaeifar, F.; Chen, J.; Chun, P.; Lyu, Q.; Cotella, G.; Aziz, H., Inverted Solution-Processed Quantum Dot Light-Emitting Devices with Wide Band Gap Quantum Dot Interlayers. *ACS Applied Materials & Interfaces* **2023,** *15* (19), 23631-23641.
80. Wang, S.; Guo, Y.; Feng, D.; Chen, L.; Fang, Y.; Shen, H.; Du, Z., Bandgap tunable Zn 1− x Mg x O thin films as electron transport layers for high performance quantum dot light-emitting diodes. *Journal of Materials Chemistry C* **2017,** *5* (19), 4724-4730.
81. Alsharafi, R.; Zhu, Y.; Li, F.; Xu, Z.; Hu, H.; Guo, T., Boosting the performance of quantum dot light-emitting diodes with Mg and PVP Co-doped ZnO as electron transport layer. *Organic Electronics* **2019,** *75*, 105411.
82. Chung, D. S.; Davidson-Hall, T.; Yu, H.; Samaeifar, F.; Chun, P.; Lyu, Q.; Cotella, G.; Aziz, H., Significant enhancement in quantum-dot light emitting device stability via a ZnO: polyethylenimine mixture in the electron transport layer. *Nanoscale Advances* **2021,** *3* (20), 5900-5907.
83. Song, J.; Kulinich, S. A.; Li, J.; Liu, Y.; Zeng, H., A General One-Pot Strategy for the Synthesis of High-Performance Transparent-Conducting-Oxide Nanocrystal Inks for All-Solution-Processed Devices. *Angewandte Chemie International Edition* **2015,** *54* (2), 462-466.
84. Sun, Y.; Wang, W.; Zhang, H.; Su, Q.; Wei, J.; Liu, P.; Chen, S.; Zhang, S., High-performance quantum dot light-emitting diodes based on Al-doped ZnO nanoparticles electron transport layer. *ACS applied materials & interfaces* **2018,** *10* (22), 18902-18909.
85. Kim, H. H.; Kumi, D. O.; Kim, K.; Park, D.; Yi, Y.; Cho, S. H.; Park, C.; Ntwaeaborwa, O.; Choi, W. K., Optimization of the electron transport in quantum dot light-emitting diodes by codoping ZnO with gallium (Ga) and magnesium (Mg). *RSC advances* **2019,** *9* (55), 32066-32071.
86. Wang, F.; Sun, W.; Liu, P.; Wang, Z.; Zhang, J.; Wei, J.; Li, Y.; Hayat, T.; Alsaedi, A.; Tan, Z. a., Achieving balanced charge injection of blue quantum dot light-emitting diodes through transport layer doping strategies. *The Journal of Physical Chemistry Letters* **2019,** *10* (5), 960-965.

87. Kim, H.-M.; Cho, S.; Kim, J.; Shin, H.; Jang, J., Li and Mg Co-doped zinc oxide electron transporting layer for highly efficient quantum dot light-emitting diodes. *ACS applied materials & interfaces* **2018,** *10* (28), 24028-24036.
88. Cao, S.; Zheng, J.; Zhao, J.; Yang, Z.; Li, C.; Guan, X.; Yang, W.; Shang, M.; Wu, T., Enhancing the performance of quantum dot light-emitting diodes using room-temperature-processed Ga-doped ZnO nanoparticles as the electron transport layer. *ACS Applied Materials & Interfaces* **2017,** *9* (18), 15605-15614.
89. Mokarian Zanjani, S.; Tintori, F.; Sadeghi, S.; Linkov, P.; Dayneko, S.; Shahalizad, A.; Pahlevaninezhad, H.; Pahlevani, M., Tailored ZnO Functional Nanomaterials for Solution-Processed Quantum-Dot Light-Emitting Diodes. *Advanced Photonics Research* **2022,** *3* (12), 2200159.
90. Zhang, Z.; Ye, Y.; Pu, C.; Deng, Y.; Dai, X.; Chen, X.; Chen, D.; Zheng, X.; Gao, Y.; Fang, W., High-performance, solution-processed, and insulating-layer-free light-emitting diodes based on colloidal quantum dots. *Advanced Materials* **2018,** *30* (28), 1801387.
91. Yang, Y.; Su, L.; Feng, N.; Liu, A.; Xing, X.; Lu, M.; William, W. Y., Balanced charge transport and enhanced performance of blue quantum dot light-emitting diodes via electron transport layer doping. *Nanotechnology* **2021,** *32* (33), 335203.
92. Heo, S. B.; Shin, J. S.; Kim, T. Y.; Park, S.; Jung, W. H.; Kim, H.; Hong, J.-A.; Kim, B.-S.; Park, Y.; Chin, B. D., Highly efficient and low turn-on voltage quantum-dot light-emitting diodes using a ZnMgO/ZnO double electron transport layer. *Current Applied Physics* **2021,** *29*, 107-113.
93. Zhang, Q.; Gu, X.; Zhang, Q.; Jiang, J.; Jin, X.; Li, F.; Chen, Z.; Zhao, F.; Li, Q., ZnMgO: ZnO composite films for fast electron transport and high charge balance in quantum dot light emitting diodes. *Optical Materials Express* **2018,** *8* (4), 909-918.
94. Zhang, B.; Luo, Y.; Mai, C.; Mu, L.; Li, M.; Wang, J.; Xu, W.; Peng, J., Effects of ZnMgO electron transport layer on the performance of InP-based inverted quantum dot light-emitting diodes. *Nanomaterials* **2021,** *11* (5), 1246.
95. Qu, X.; Liu, W.; Li, D.; Ma, J.; Gu, M.; Jia, S.; Xiang, G.; Sun, X. W., Does interfacial exciton quenching exist in high-performance quantum dot light-emitting diodes? *Nanoscale* **2023,** *15* (7), 3430-3437.
96. Chen, D.; Ma, L.; Chen, Y.; Zhou, X.; Xing, S.; Deng, Y.; Hao, Y.; Pu, C.; Kong, X.; Jin, Y., Electrochemically Stable Ligands of ZnO Electron-Transporting Layers for Quantum-Dot Light-Emitting Diodes. *Nano Letters* **2023,** *23* (3), 1061-1067.
97. Chung, D. S.; Lyu, Q.; Cotella, G. F.; Chun, P.; Aziz, H., Suppressing Degradation in QLEDs via Doping ZnO Electron Transport Layer by Halides. *Advanced Optical Materials* **2023**, 2300686.
98. Guo, Y.; Liu, B.; Chen, Z.; Song, W.; Tian, N.; Wu, W.; Fan, X.; Zhan, Y.; Meng, F.; Zeng, Q., Water-passivated ZnMgO nanoparticles for blue quantum dot light-emitting diodes. *Journal of Materials Chemistry C* **2021,** *9* (32), 10381-10387.
99. Acharya, K. P.; Titov, A.; Hyvonen, J.; Wang, C.; Tokarz, J.; Holloway, P. H., High efficiency quantum dot light emitting diodes from positive aging. *Nanoscale* **2017,** *9* (38), 14451-14457.
100. Su, Q.; Sun, Y.; Zhang, H.; Chen, S., Origin of Positive Aging in Quantum-Dot Light-Emitting Diodes. *Advanced Science* **2018,** *5* (10), 1800549.
101. Zhang, W.; Chen, X.; Ma, Y.; Xu, Z.; Wu, L.; Yang, Y.; Tsang, S.-W.; Chen, S., Positive aging effect of ZnO nanoparticles induced by surface stabilization. *The Journal of Physical Chemistry Letters* **2020,** *11* (15), 5863-5870.
102. Chen, D.; Chen, D.; Dai, X.; Zhang, Z.; Lin, J.; Deng, Y.; Hao, Y.; Zhang, C.; Zhu, H.; Gao, F., Shelf-stable quantum-dot light-emitting diodes with high operational performance. *Advanced Materials* **2020,** *32* (52), 2006178.

103. Chen, J.; Ghorbani, A.; Chung, D. S.; Azadinia, M.; Davidson-Hall, T.; Chun, P.; Lyu, Q.; Cotella, G.; Song, D.; Xu, Z., Influence of Encapsulation on the Efficiency and Positive Aging Behavior in Blue Quantum Dot Light-Emitting Devices. *ACS Applied Materials & Interfaces* **2023,** *15* (28), 34240-34248.
104. Chen, J.; Ghorbani, A.; Samaeifar, F.; Chun, P.; Lyu, Q.; Cotella, G.; Song, D.; Xu, Z.; Aziz, H., Long-term spontaneous negative aging behavior of encapsulated blue quantum dot light emitting devices: the influence of the hole transport material. *Journal of Materials Chemistry C* **2023,** *11* (40), 13788-13793.
105. Okamoto, S.; Tanaka, K.; Izumi, Y.; Adachi, H.; Yamaji, T.; Suzuki, T., Simple measurement of quantum efficiency in organic electroluminescent devices. *Japanese journal of applied physics* **2001,** *40* (7B), L783.
106. Lee, C.; Moon, H.; Kim, J.; Kim, H.; Chae, H., Ethanedithiol treatment on zinc oxide films for highly efficient quantum dot light-emitting diodes by reducing exciton quenching. *JOSA B* **2020,** *37* (2), 304-310.
107. Jing, J.; Lin, L.; Yang, K.; Hu, H.; Guo, T.; Li, F., Highly efficient inverted quantum dot light-emitting diodes employing sol-gel derived Li-doped ZnO as electron transport layer. *Organic Electronics* **2022,** *103*, 106466.
108. Pan, J.; Wei, C.; Wang, L.; Zhuang, J.; Huang, Q.; Su, W.; Cui, Z.; Nathan, A.; Lei, W.; Chen, J., Boosting the efficiency of inverted quantum dot light-emitting diodes by balancing charge densities and suppressing exciton quenching through band alignment. *Nanoscale* **2018,** *10* (2), 592-602.
109. Cohn, A. W.; Kittilstved, K. R.; Gamelin, D. R., Tuning the potentials of "extra" electrons in colloidal n-type ZnO nanocrystals via Mg2+ substitution. *Journal of the American Chemical Society* **2012,** *134* (18), 7937-7943.
110. Hofmann, D.; Pfisterer, D.; Sann, J.; Meyer, B.; Tena-Zaera, R.; Munoz-Sanjose, V.; Frank, T.; Pensl, G., Properties of the oxygen vacancy in ZnO. *Applied Physics A* **2007,** *88*, 147-151.
111. Mondal, P., Effect of Oxygen vacancy induced defect on the optical emission and excitonic lifetime of intrinsic ZnO. *Optical Materials* **2019,** *98*, 109476.
112. Purbayanto, M. A. K.; Nurfani, E.; Chichvarina, O.; Ding, J.; Rusydi, A.; Darma, Y., Oxygen vacancy enhancement promoting strong green emission through surface modification in ZnO thin film. *Applied Surface Science* **2018,** *462*, 466-470.
113. Ghorbani, A.; Chen, J.; Chun, P.; Lyu, Q.; Cotella, G.; Aziz, H., Changes in Hole and Electron Injection under Electrical Stress and the Rapid Electroluminescence Loss in Blue Quantum-Dot Light-Emitting Devices. *Small* **2023**, 2304580.
114. Davidson-Hall, T.; Aziz, H., Perspective: Toward highly stable electroluminescent quantum dot light-emitting devices in the visible range. *Applied Physics Letters* **2020,** *116* (1).
115. Nebatti, A.; Zekri, A.; Zakaria, Y.; Singh, R.; Mukherjee, S.; Kadari, A.; Guezzoul, M.; Khodja, K.; Amrani, B.; Aïssa, B., Compositional mapping of Mo-doped ZnO thin films: Mechanical, nano-surface and ToF-SIMS analyses. *Journal of Molecular Structure* **2023,** *1286*, 135566.
116. Cho, H.; Park, S.; Shin, H.; Kim, M.; Jang, H.; Park, J.; Yang, J. H.; Han, C. W.; Baek, J. H.; Jung, Y. S., Highly Efficient Deep Blue Cd-Free Quantum Dot Light-Emitting Diodes by ap-Type Doped Emissive Layer. *Small* **2020,** *16* (40), 2002109.
117. Alexandrov, A.; Zvaigzne, M.; Lypenko, D.; Nabiev, I.; Samokhvalov, P., Al-, Ga-, Mg-, or Li-doped zinc oxide nanoparticles as electron transport layers for quantum dot light-emitting diodes. *Scientific Reports* **2020,** *10* (1), 7496.
118. Kajiyama, Y.; Kajiyama, K.; Aziz, H., Diffusion barriers for achieving controlled concentrations of luminescent dopants via diffusion for mask-less RGB color patterning of organic light emitting devices. *Optics Express* **2015,** *23* (24), 30783-30792.

119. Lin, C.-Y.; Lin, Y.-C.; Hung, W.-Y.; Wong, K.-T.; Kwong, R. C.; Xia, S. C.; Chen, Y.-H.; Wu, C.-I., A thermally cured 9, 9-diarylfluorene-based triaryldiamine polymer displaying high hole mobility and remarkable ambient stability. *Journal of Materials Chemistry* **2009,** *19* (22), 3618-3623.
120. Chen, S.; Cao, W.; Liu, T.; Tsang, S.-W.; Yang, Y.; Yan, X.; Qian, L., On the degradation mechanisms of quantum-dot light-emitting diodes. *Nature communications* **2019,** *10* (1), 1-9.
121. Lee, H.; Song, S.-W.; Hwang, K. M.; Kim, K. J.; Yang, H.; Kim, Y. K.; Kim, T., Hybrid white quantum dot–organic light-emitting diodes with highly stable CIE x, y coordinates by the introduction of n-type modulation and multi-stacked hole transporting layer. *Journal of Materials Chemistry C* **2021,** *9* (36), 12248-12254.
122. Shendre, S.; Sharma, V. K.; Dang, C.; Demir, H. V., Exciton dynamics in colloidal quantum-dot LEDs under active device operations. *ACS Photonics* **2018,** *5* (2), 480-486.
123. Cheng, Y.; Gui, Z.; Qiao, R.; Fang, S.; Ba, G.; Liang, T.; Wan, H.; Zhang, Z.; Liu, C.; Ma, C., Electronic structural insight into high-performance quantum dot light-emitting diodes. *Advanced Functional Materials* **2022**, 2207974.
124. Liu, D.; Cao, S.; Wang, S.; Wang, H.; Dai, W.; Zou, B.; Zhao, J.; Wang, Y., Highly stable red quantum dot light-emitting diodes with long T 95 operation lifetimes. *The Journal of Physical Chemistry Letters* **2020,** *11* (8), 3111-3115.
125. Ghorbani, A.; Chen, J.; Samaeifar, F.; Azadinia, M.; Chun, P.; Lyu, Q.; Cotella, G.; Aziz, H., Stability Improvement in Quantum-Dot Light-Emitting Devices via a New Robust Hole Transport Layer. *The Journal of Physical Chemistry C* **2022,** *126* (42), 18144-18151.
126. Azadinia, M.; Davidson-Hall, T.; Chung, D. S.; Ghorbani, A.; Samaeifar, F.; Chen, J.; Chun, P.; Lyu, Q.; Cotella, G.; Aziz, H., Inverted Solution-Processed Quantum Dot Light-Emitting Devices with Wide Band Gap Quantum Dot Interlayers. *ACS Applied Materials & Interfaces* **2023**.
127. Kim, S.-K.; Yang, H.; Kim, Y.-S., Control of carrier injection and transport in quantum dot light emitting diodes (QLEDs) via modulating Schottky injection barrier and carrier mobility. *Journal of Applied Physics* **2019,** *126* (18), 185702.
128. Kim, S.-K.; Kim, Y.-S., Charge carrier injection and transport in QLED layer with dynamic equilibrium of trapping/de-trapping carriers. *Journal of Applied Physics* **2019,** *126* (3), 035704.
129. Ye, Y.; Wang, J.; Qiu, Y.; Liu, J.; Ye, B.; Yang, Z.; Gong, Z.; Xu, L.; Zhou, Y.; Huang, Q., Ultra-low EQE roll-off and marvelous efficiency perovskite quantum-dots light-emitting-diodes achieved by ligand passivation. *Nano Energy* **2021,** *90*, 106583.
130. Haneef, H. F.; Zeidell, A. M.; Jurchescu, O. D., Charge carrier traps in organic semiconductors: a review on the underlying physics and impact on electronic devices. *Journal of Materials Chemistry C* **2020,** *8* (3), 759-787.
131. Park, Y.-S.; Bae, W. K.; Pietryga, J. M.; Klimov, V. I., Auger recombination of biexcitons and negative and positive trions in individual quantum dots. *ACS nano* **2014,** *8* (7), 7288-7296.
132. Du, W.; Cheng, C.; Tian, J., Efficient solution-processed InP quantum-dots light-emitting diodes enabled by suppressing hole injection loss. *Nano Research* **2022**, 1-7.
133. Ashkenov, N.; Mbenkum, B.; Bundesmann, C.; Riede, V.; Lorenz, M.; Spemann, D.; Kaidashev, E.; Kasic, A.; Schubert, M.; Grundmann, M., Infrared dielectric functions and phonon modes of high-quality ZnO films. *Journal of Applied Physics* **2003,** *93* (1), 126-133.
134. Bin, Z.; Liu, Z.; Duan, L., Organic radicals outperform LiF as efficient electron-injection materials for organic light-emitting diodes. *The Journal of Physical Chemistry Letters* **2017,** *8* (19), 4769-4773.
135. Yamada, T.; Suzuki, F.; Goto, A.; Sato, T.; Tanaka, K.; Kaji, H., Revealing bipolar charge-transport property of 4, 4′-N, N′-dicarbazolylbiphenyl (CBP) by quantum chemical calculations. *Organic Electronics* **2011,** *12* (1), 169-178.

136. Ghorbani, A.; Chen, J.; Chun, P.; Lyu, Q.; Cotella, G.; Aziz, H., Changes in Hole and Electron Injection under Electrical Stress and the Rapid Electroluminescence Loss in Blue Quantum-Dot Light-Emitting Devices. *Small* **2024,** *20* (1), 2304580.
137. Makino, T.; Segawa, Y.; Tsukazaki, A.; Ohtomo, A.; Kawasaki, M., Electron transport in ZnO thin films. *Applied Physics Letters* **2005,** *87* (2).
138. Jiang, Q.; Zhang, X.; You, J., SnO2: a wonderful electron transport layer for perovskite solar cells. *Small* **2018,** *14* (31), 1801154.

Appendices

Appendix A

Supplementary Information for Chapter 4

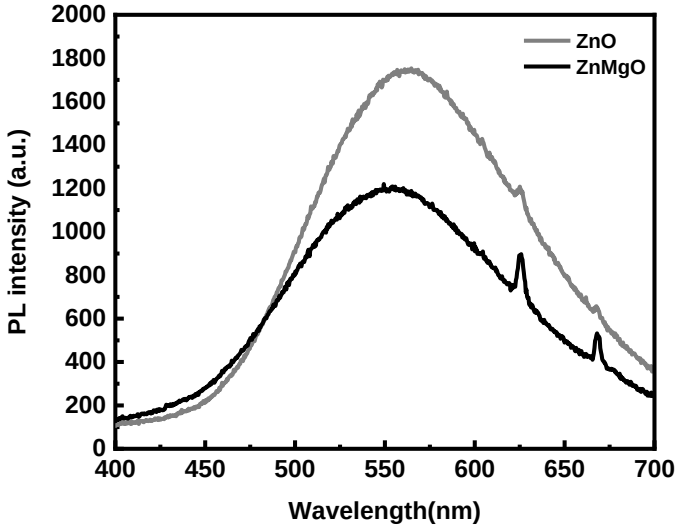

Figure S 4.1 The PL spectra of ZnO and ZnMgO fresh films, collected under 330 nm excitation.

a)

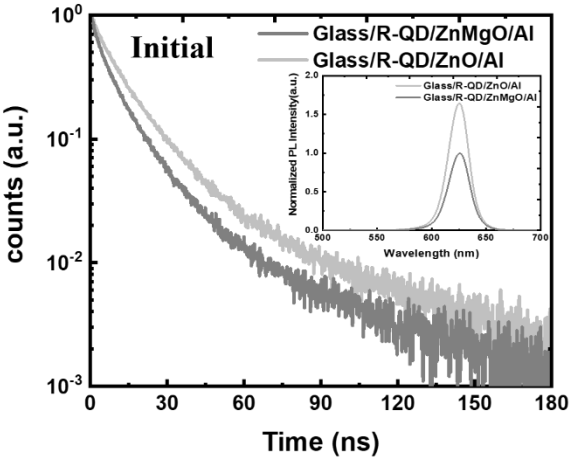

b)

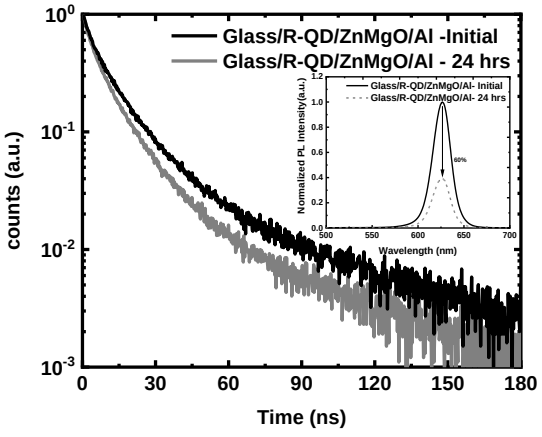

c)

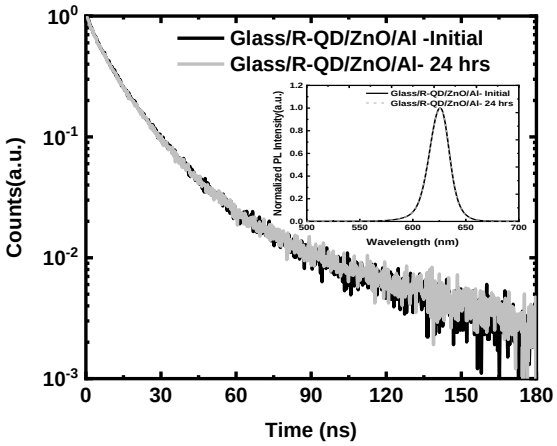

Figure S 4.2 a) TRPL decay characteristics of the R-QDs in contact with ZnO and ZnMgO in fresh samples. b) TRPL decay characteristics of the R-QDs in contact with b) the ZnMgO layer c) the ZnO layer, initially and after 24 hours. All the insets show the corresponding PL spectra with normalized intensities.

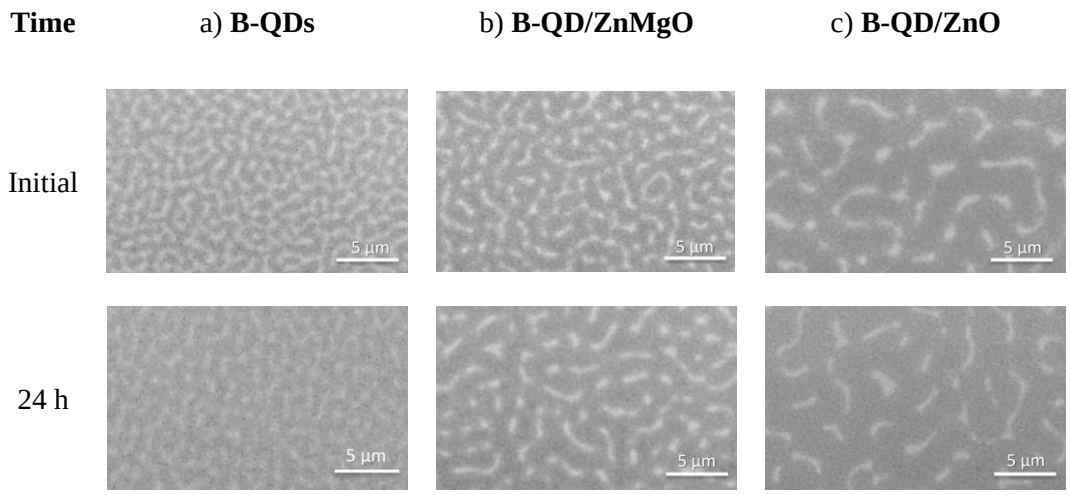

Figure S 4.3 The microscope images of a) B-QDs b) B-QD/ZnMgO c) B-QD/ZnO films initially and after 24 hours of storage with ×100 magnification.

a)

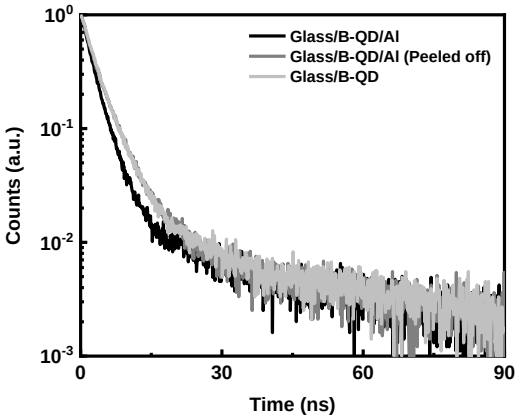

b)

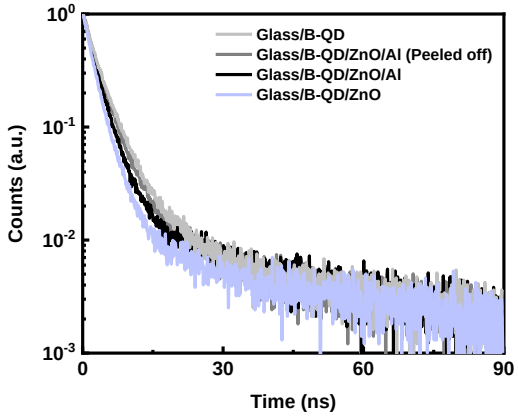

c)

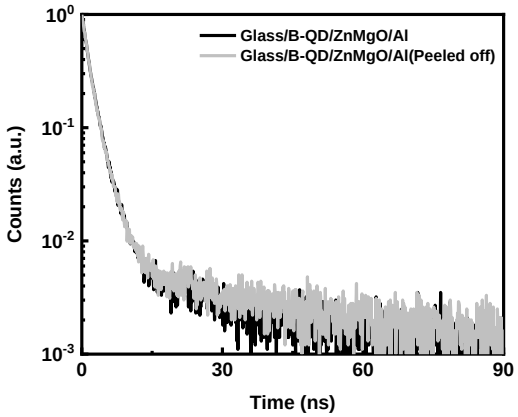

Figure S 4.4 TRPL decay characteristics of a) Glass/B-QDs/ZnMgO/Al b) Glass/B-QDs/ZnO/Al c) Glass/B-QDs/Al 24hrs old samples immediately before and after Al peel off collected under 380 nm excitation.

a)

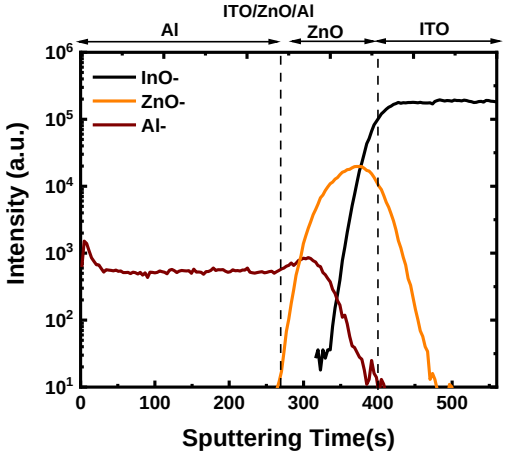

b)

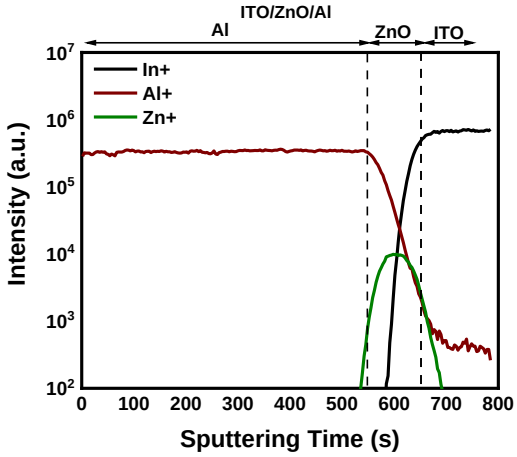

c)

d)

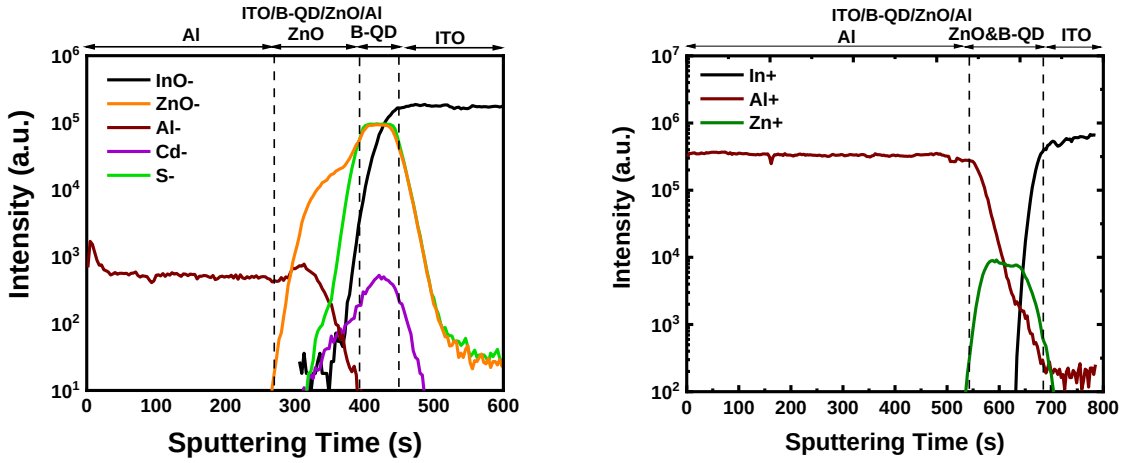

Figure S 4.5 The TOF-SIMS depth profiles of a) ITO/ZnO/Al (Negative polarity) b) ITO/ZnO/Al (Positive polarity) c) ITO/B-QD/ZnO/Al (Negative polarity) d) ITO/B-QD/ZnO/Al (Positive polarity)

Appendix B

Supplementary Information for Chapter 6

a)

b)

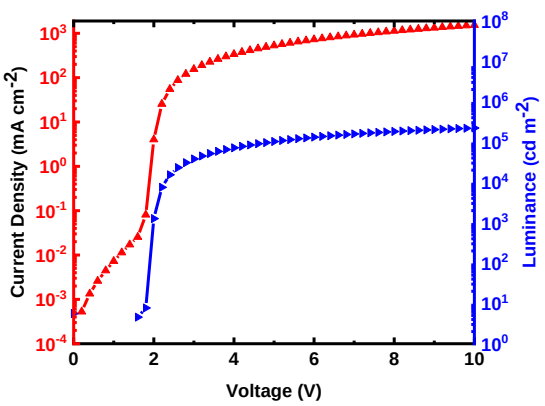

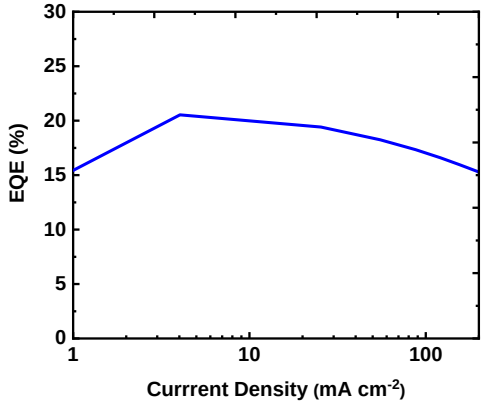

c)

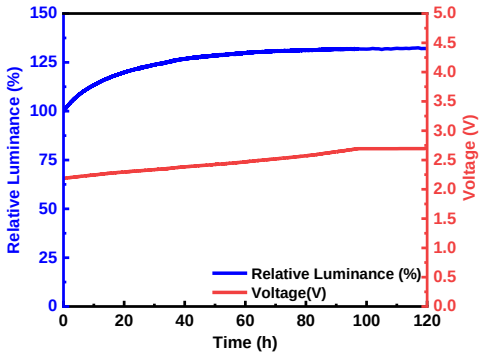

Figure S 6.1 a) J-V-L characteristics of R-QLED b) EQE versus current density of the R-QLED c) EL of R-QLEDs normalized to its initial value and driving voltage of the R-QLED as a function of time under a constant driving current density of 20 mA/cm^2.

a) b) c)

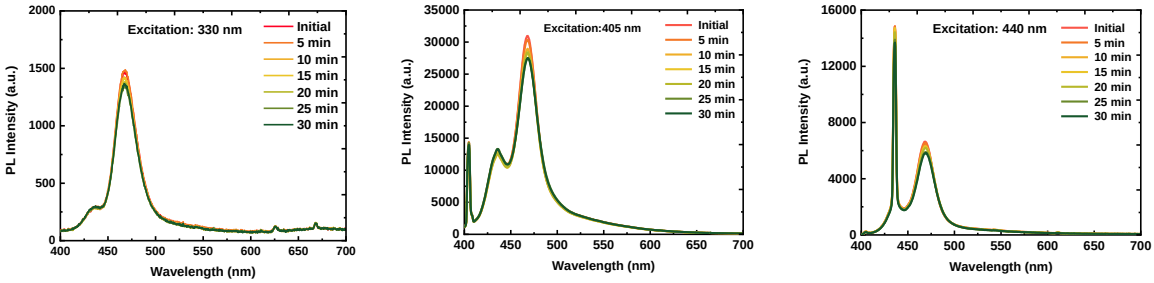

Figure S 6.2 PL spectra of the B-QLEDs, measured after the shown aging time under a constant driving current density of 20 mA/cm^2 driving. The PL spectra are collected under a) 330 nm b) 405 nm c) 440 nm excitation wavelength.

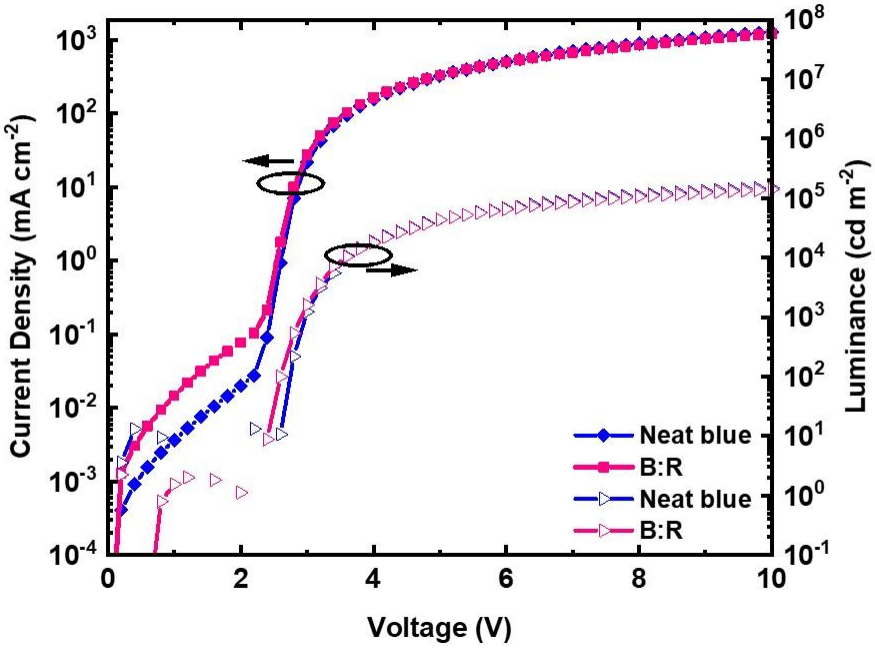

Figure S 6.3 J-V-L characteristics of the neat B- and B:R-QLEDs

a) b)

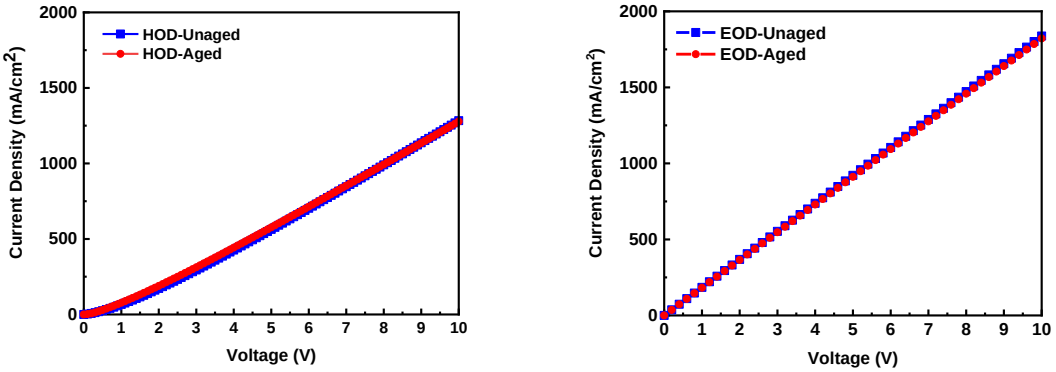

Figure S 6.4 J-V characteristics of unaged and aged a) HODs (ITO/PEDOT:PSS/TFB/MoO3/Al) b) EODs (ITO/ZnO(sol-gel)/ZnMgO/Al). The devices are driven at a constant current density of 20 mA/cm^2 for 24 h.

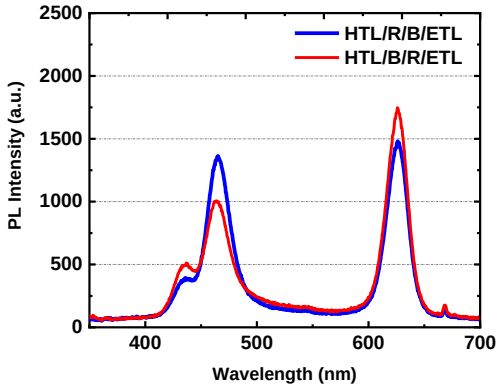

Figure S 6.5 PL spectra of HTL/R/B/ETL and HTL/B/R/ETL devices under 330 nm excitation wavelength.

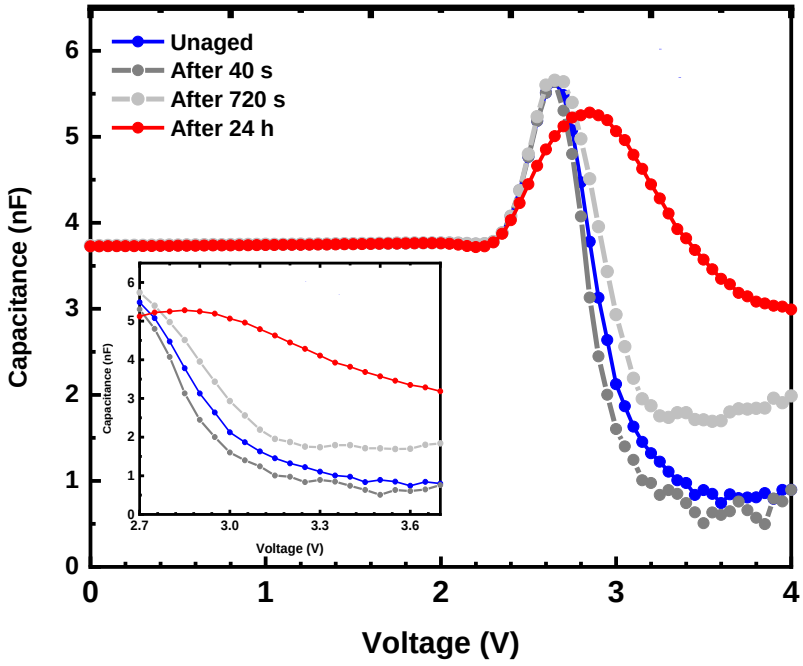

Figure S 6.6 C-V characteristics of B-QLED under electrical stress for different periods of time.

a) b)

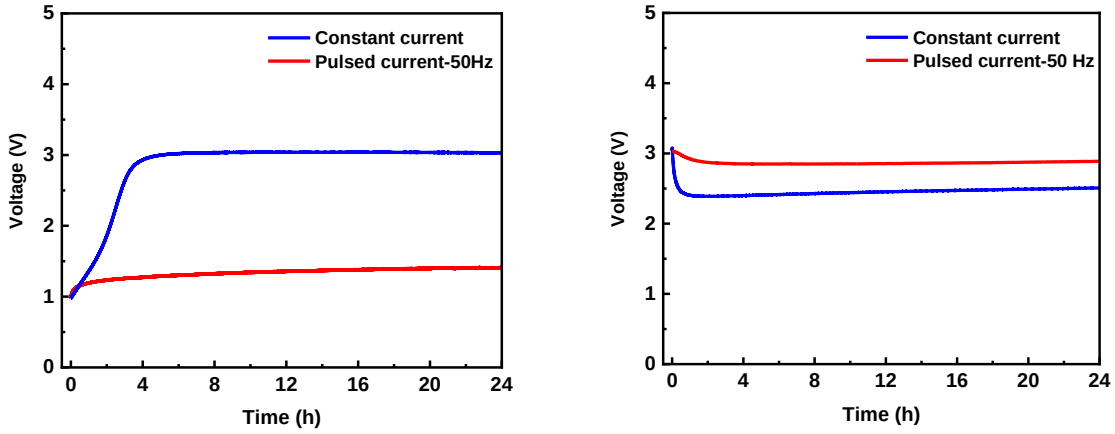

Figure S 0.7 Driving voltage versus time trends of a) EODs (ITO/ZnO(sol-gel)/B-QD/ZnMgO/Al) b) HODs (ITO/PEDOT:PSS/TFB/B-QD/MoO_3/Al). The devices are aged under a constant current density of 10 mA/cm^2 and pulsed current with an amplitude of 20 mA/cm^2 and frequency of 50 Hz.

Appendix C

Supplementary Information for Chapter 7

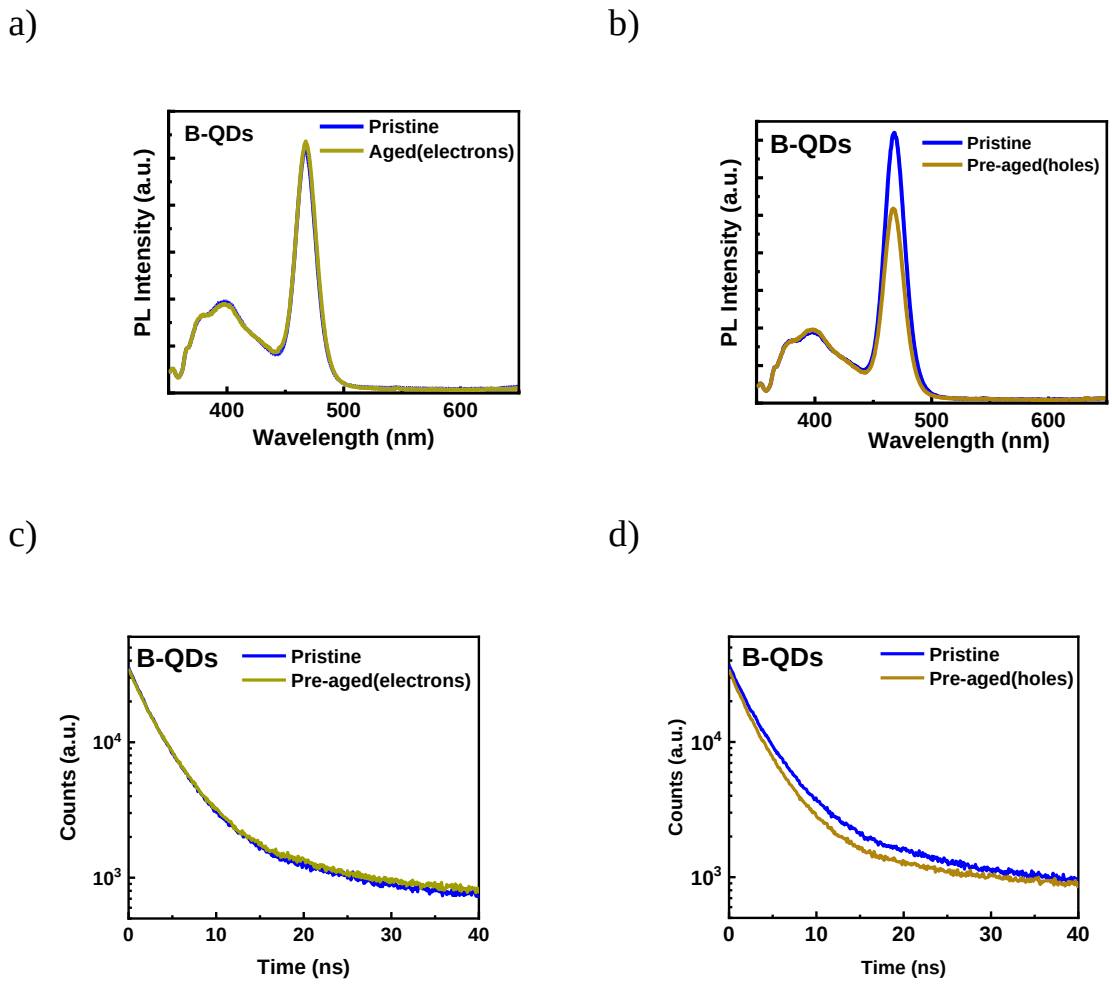

Figure S 7.6 The PL spectra of inverted B-QLED using pristine and pre-aged ZnMgO layer a) under electron-rich current flow, b) under hole-rich current flow. The TRPL characteristics of inverted B-QLED using pristine and pre-aged ZnMgO layer c) under electron-rich current flow, d) under hole-rich current flow.